THOR's Martian War:

Testing a new GCM's ability to model Mars's atmosphere

by

Corine Brown

A thesis submitted to Macquarie University
for the degree of Master of Research
Department of Earth and Environmental Sciences
19 December 2019

Contents

Statement

I, Corine Yvette Brown, hereby confirm that the thesis submitted herein has not previously or presently been submitted for a higher degree to any other university or institution. No Ethics Committee approval was required to complete this work.

Corine Yvette Brown

Student Name

Student Signature

Acknowledgements

First and foremost, I'd like to give a great, big, extra-special thank you to my family – Mum, Nan, Craig, Clinton, Rosslyn – for being the greatest cheer squad and strongest support network I could imagine, especially after all we've gone through these last few years. In your own unique ways, you've each been an immense help to me throughout this whole experience. I'd be lost without you. Thanks also to my "pseudo-family" – Sheryl, Aidan, Darlene, Delphine – for somehow still being there for me even when you were hundreds of kilometres away.

Secondly, but by no means less importantly, I'd like to extend my deepest, heartfelt gratitude to my truly indefatigable supervisors, Dr Kevin Cheung and A/Prof. Craig O'Neill, for their invaluable guidance, infinite patience, and unwavering support – especially when literally everything that could possibly go wrong actually *did* go wrong. Thanks for not letting me give up. There's no way I could have made it through this without you both.

Special thanks go to Dr Greg Bodeker for his early assistance in formulating ideas for this project and for welcoming me into his organisation, however briefly. Thanks also to: Dr Katie Dafforn and Dr Stefan Loehr from the environmental sciences department for helping me to navigate the maze of bureaucracy; Prof. Mark Wardle, Prof. Orsola De Marco, and A/Prof. Richard McDermid from the astronomy department for the little snippets of insight and advice; and Richard Miller from faculty I.T. for helping to sort out all of my many, many I.T. issues along the way.

To my fellow MRes cohort, thank you for keeping me sane throughout this whole thing. Especially Sam Brown, who endured my many anxiety-ridden ramblings with an almost preternatural serenity, remaining totally confident that I could pull this off even when I had no confidence at all. Bless your heart, Sam, you have the patience of a saint. I wish you all the luck in the world.

Lastly, I'd like to acknowledge the late Dr. Grant Edwards, my initial principal supervisor on this project. You saw something in me from the first undergraduate class of yours that I ever took and believed in me enough to say – even then – that if I ever wanted to do postgraduate study, you'd be happy to take me on as a student. You mentored me, provided me with incredible opportunities, supported me even when my personal life was repeatedly turned upside down, and I am deeply, immensely grateful to you for everything. I'm sorry I never managed to get that job at NASA that you were going to ride my coattails on before you passed away, but I promise I'll still try to get a job there one day. You were a big man with a big heart, and you'll be profoundly missed. But in the words of Thor's father, Odin:

"Cattle die, and kinsman die,
You yourself must also die;
One thing that will never die,
The fame of a dead man's deeds."
- Hávamál, verse 76

May your memory live long and prosper.

Abstract

Observations of planets within and beyond our solar system have highlighted a diverse range of planetary climates that Earth-centric and Earth-derived General Circulation Models (GCMs) are unlikely to be suited to. A self-consistent GCM, capable of adapting to a wide range of planetary conditions without compromising accuracy, is therefore needed. A new GCM called THOR may fill this void. THOR, an atmospheric fluid dynamics solver optimized for GPU computation, was developed from first principles and lacks the assumptions of Earth-derived GCMs. Its performance has been tested with the Martian atmosphere using fundamental planetary and orbital properties with a basic radiative transfer scheme, although topography has not been included. Through this, the influence of optical depth and obliquity on zonally-averaged temperature, zonal winds, and vertical velocity has been investigated. A key finding is that dust has a first-order effect and is particularly important at higher obliquities. Results were compared extensively against previous studies of Mars which had made use of existing GCMs for simulations. These results indicate that THOR's dynamics perform reasonably well but confirm its high sensitivity to dust loading. Future improvements to THOR's treatment of dust and aerosols could make THOR quite suitable for simulation with dusty planets.

CHAPTER 1 – INTRODUCTION AND BACKGROUND

1.1. INTRODUCTION

Identifying habitable planets outside the Solar System could be critical to humanity's future. Atmospheric modelling will be a crucial research tool for assessing "exoplanetary" habitability. In recent years, the rate of exoplanet detections has increased. At the time of writing, the NASA Exoplanet Archive lists 4141 confirmed exoplanet detections and observational surveys indicate that almost every star within 50 parsecs of our solar system is home to at least one planet (Howard et al., 2012, Madhusudhan et al., 2016). Presumably, all of these planets have atmospheres but so far, basic atmospheric characterisation has been limited to larger planets – most commonly hot Jupiters (Jupiter-like gas giants orbiting their parent stars at extremely small distances of <0.05 astronomical units (AU) (Knutson et al., 2007)). These planets can be more than 10 times the size of Jupiter, with temperatures between 800-3000 K, making them more conducive to observations (Madhusudhan et al., 2016). This makes studying "Earth-like" planets challenging. Loosely defined, these are planets with roughly 0.1-10 times the mass and/or 0.4-2.5 times the radius of Earth (PHL, 2012). They account for approximately 45-62% of confirmed and candidate exoplanet detections (PHL, 2018); however, most of these, like hot Jupiters, are detected at distances too close to their parent stars to potentially be considered habitable. Earth-like planets detected within the "habitable" zone comprise only ~1.5% of all detections; of those, only ~22% have been detected orbiting stars like our Sun (Petigura et al., 2013, PHL, 2018). New generation space telescopes and giant ground-based telescopes scheduled for launch in the next few years may increase detection rates for all planet types, including those orbiting Sun-like stars. As such, a flexible general circulation model (GCM) will be required to study their atmospheres. To provide a baseline comparison, the atmospheres of planets in our own solar system will need to be studied in greater detail and used as "test subjects" for new GCM candidates. For Earth-like planet comparisons, more than one Earth analogue can be found in our solar system. Venus is one – similar in size but located at the hot, inner edge of the habitable zone (Kane et al., 2019). Mars is another – smaller than Earth but with a similar climate in some respects (Read et al., 2015). In this paper, Mars will be used as a test subject for THOR – a new GCM designed from first principles to study exoplanetary atmospheres.

1.2. PLANETARY CLIMATE FACTORS

Many factors impact on the *thermal emission* of an Earth-like planet. According to Gómez-Leal et al. (2016), an uneven distribution of continents and/or large-scale topography leads to uneven

distribution of surface temperature and convection, the presence of clouds can dramatically decrease thermal emission, planets with a uniform surface covering of liquid water (so-called "aquaplanets") have a higher mean surface temperature due to a lower overall albedo, and ice-covered worlds experience an ice-albedo feedback that keeps temperatures cold and the atmosphere dry. Retention of volatile and non-condensable gases, whether they have a greenhouse effect or not, is also important for warming the planet's coldest surface regions (Turbet et al., 2016). More importantly, orbital forcings (changes in the planet's eccentricity, precession, and obliquity) have a strong impact on the amount of incoming solar radiation and thus *radiative equilibrium*. The most significant of these is obliquity. A wide range of obliquities have been identified in detected exoplanets, but even in our own solar system, the range of obliquities is great. Mercury, Venus, and Jupiter all have very small obliquities (~0°, ~2.5°, and ~3° respectively), meaning that the distribution of insolation incident on their surfaces is nearly symmetric with respect to the equator, and absorbed stellar radiation is lowest at the poles (Gómez-Leal et al., 2016, Levine et al., 1977). Planets with obliquity values of 23.5-54° – for example Earth (~23.5°), Saturn (~26.5°), and Neptune (~29°) – exhibit a heat gain at the tropics and a greater amount of absorbed radiation at lower latitudes, leading to sustained *Hadley cells*. If there is any east-west heating asymmetry, zonal cells may develop as well (Gómez-Leal et al., 2016, Levine et al., 1977).

Mars currently has an obliquity similar to Earth's – ~25° – but due to gravitational perturbations from other planets, this can oscillate between 0-60° over the course of 2.5-10 Myr (Laskar and Robutel, 1993, Read et al., 2015). This has major implications for the study of its long-term climate and atmospheric composition, particularly with regard to the capture and release of CO_2 from the polar caps. A major uncertainty, though, is just how much the Martian surface pressure might increase at higher obliquities, as it is unknown how much of a residual subsurface CO_2 ice reservoir is left from the last period of very low obliquity (Read et al., 2015).

1.3. MARS'S CLIMATE

Mars is perhaps Earth's closest relation in terms of meteorology and climate. It has seasons and complex nonlinear feedbacks that affect external forcing responses. There are, however, significant differences. The most obvious are its smaller size and its larger (and longer) orbit. Others include larger scale topography, no liquid oceans or vegetation, and a thinner, mostly CO_2 atmosphere. Its atmospheric structure and near-surface environment are influenced by similar processes to those

found on Earth but on Mars, they operate under much harsher and more extreme conditions (Read et al., 2015). Viking Lander data has shown evidence of an annual surface pressure cycle, suggesting that the atmospheric CO_2 cycle has minimal interannual variability. H_2O and global atmospheric dust loading data also exhibit annual cycles; however, the actual dust cycle is highly variable (Hollingsworth, 2010). The thermal structure of the atmosphere cannot be accounted for by a mostly CO_2 atmosphere unless atmospheric dust is also considered, and the variability of the dust cycle also has significant impacts on heating rates and temperatures (Madeleine et al., 2011).

1.3.1. Eccentricity, topography, and thermal structure

Mars's orbit is roughly 5.5 times more eccentric ($e \approx 0.0934$) than Earth's orbit ($e \approx 0.0167$) (Williams, 2018b, Williams, 2020). Its perihelion occurs just before the southern summer solstice, resulting in a much stronger meridional circulation during southern summer than in northern summer (Read et al., 2015). But despite this, it is Mars's hemispherically asymmetric topography, not its orbital eccentricity, that is most responsible for this north-south difference in seasonal circulation. Mars's surface is characterised by polar ice caps and a global divide of 2.5 to 6 km in elevation between the northern and southern hemispheres, giving rise to the southern "highlands" – featuring the Tharsis Rise volcanic province (which extends into the northern hemisphere), the Valles Marineris rift, and the Hellas and Argyre impact basins – and the northern "lowlands" of the Vastitas Borealis Formation (Watters et al., 2007). For reference, a full-page map of Mars's main topographical features is provided in Appendix 1. This hemispheric dichotomy results in a more significant atmospheric perturbation in the southern hemisphere than in the northern hemisphere, as well as a net mass transfer of dust and water vapour from south to north. In fact, continental-scale orography is a major player in determining the zonal and meridional scales of individual atmospheric disturbances such as fronts and sub-synoptic circulation patterns, as well as helping to steer baroclinic waves into focused storm zones (Hollingsworth and Kahre, 2010, Read et al., 2015).

Mars's externally irradiated atmosphere is relatively transparent in the infrared. Thus, compared to Earth the exchange between incoming solar radiation and outgoing surface radiation has an even greater impact on Mars's overall energy balance. Furthermore, even though atmospheric convection and transport are active, they are comparatively weak. Hence, surface conditions such as temperature, humidity, and wind are generally determined by latitude and time of day. Mars has no oceans, so its thermal inertia – i.e. the ability to store and re-radiate heat on diurnal and seasonal

timescales – is much lower than that of Earth, making its atmospheric response time much shorter and its diurnal temperature variations much larger (Justus et al., 2002, Read et al., 2015).

Taken together, according to Read et al. (2015), this means that Mars's large-scale topography has multiple impacts: (1) high elevation slopes act as heat sources, generating thermal perturbations; (2) these slopes act as mechanical obstacles to the horizontal circulation; and (3) the varying topography activates and/or regulates several thermal tide modes and planetary-scale stationary waves. The combined effect of Mars's orbital eccentricity and asymmetric topography is that the largest of Mars's frequent dust storms are almost always generated in the southern hemisphere. On small scales, the combination of solar irradiance and adiabatic cooling with height generates *anabatic* and *katabatic* winds. These are common on Earth but, due to Mars's low thermal inertia, Martian slope winds are much stronger and an important source of dust lifting (see section 1.3.2).

Due to the above factors, Mars has a very distinct thermal structure. At most latitudes, particularly in the tropics, temperature usually only decreases with height. Thermal inversions do occur, however, in the middle and upper atmosphere at high latitudes and, due to rapid surface cooling, nocturnal shallow thermal inversions also occur at mid-latitudes. 1D microphysical models and GCMs have shown that most of these inversions are caused by the presence of clouds (Steele et al., 2014b). There is no stratosphere and thus no tropopause. As such, cells can extend to far greater altitudes than on Earth and have no clearly defined tops. Near the surface, super-adiabatic layers frequently occur due to a lower atmospheric density restricting the air's heat-carrying capacity. During the day, incoming solar radiation triggers buoyancy of the air, which is then convected by intense upwelling plumes and weaker downwelling regions. Thus, the thermal structure is generally characterised by a deep, convective boundary layer of anywhere from 2 km to 9 km in depth, topped by a near-neutral entrainment layer and a stable capping inversion (Read et al., 2015).

Seasonal cycles are also evident in the thermal structure, most strongly exhibited by a symmetrical "equinoctial mode" centred around the equator at each equinox and an asymmetric "solstitial mode" in which surface temperatures at each solstice increase monotonically from the winter pole to the summer pole at almost all heights (McCleese et al., 2010, Read et al., 2015). The reason for such asymmetry at the solstices is a combination of two things: (1) Mars's obliquity ensures that the poles receive continuous daylight for months, compensating for the large solar zenith angle and any

increased dust loading, and (2) Mars's low thermal inertia shifts the warmest parts of the surface to higher latitudes in the summer hemisphere (Levine et al., 1977, Read et al., 2015).

The solstitial mode is far more intense in southern summer due to the nature of Mars's orbital eccentricity. Since southern summer occurs at perihelion and northern summer occurs at aphelion, the southern pole receives far more incident solar radiation than the northern pole does during their respective summers (see Appendix 2, Figure 1), and southern winters are far longer and colder than northern winters. Consequently, the southern polar cap is quite extensive in winter, but it rapidly, almost completely melts in summer. By comparison, the northern polar cap is a permanent feature of the Martian surface, though its extent grows and shrinks with the seasons (Levine et al., 1977). The strong horizontal thermal gradient found in the winter hemisphere is a condition known as "baroclinicity". (More precisely, this condition is one in which density relies on both pressure *and* temperature, so the surfaces of constant pressure and constant density intersect rather than run parallel (Haltiner, 1957, Hollingsworth and Kahre, 2010) – see Appendix 2, Figure 2). Together with the almost neutral vertical stability in the winter hemisphere, *baroclinic instability* is likely to develop. This is a wave-like instability with the capacity to release potential energy from statically stable, sloping isotherms in the vertical direction. Images of vertically-spiralling, westerly dust clouds and dust fronts in the extra-tropics and subtropics taken by the Viking and Mars Global Surveyor orbiters are perfect examples of this, bearing a remarkable resemblance to Earth's extratropical cyclones (Hollingsworth and Kahre, 2010). Baroclinic waves appear to be weaker in southern winter than in northern winter and do not develop at some longitudes, which may be due to the hemispherically asymmetric topography and weaker irradiance in southern winter, although this is still not well understood.

1.3.2. Dust

Airborne dust permeates the entire Martian atmosphere. Since almost the entire planet is covered in sand, dust, and boulders, dust can be lifted into the atmosphere by near-surface meteorological phenomena almost everywhere and then be easily deposited elsewhere. This means that the dust loading at any one location is highly variable (Read et al., 2015). Thermal emission spectrometry of Martian albedo has shown that the northern hemisphere is covered by far more dust than the southern hemisphere and that redistribution of dust caused by major dust storms may lead to significant regional depletion of liftable materials. Additionally, Mars Climate Sounder (MCS) observations show that some regions are sometimes virtually dust-free (Read et al., 2015).

The effect of atmospheric dust on Mars's surface insolation cannot be overstated. A perfect example is the planet-encircling dust storm in the southern summer of 1971. Observations of this storm showed that atmospheric optical depth exhibited a 20-fold increase, while mean annual daily surface insolation plummeted 100-fold due to the increased dust loading. The peak of solar insolation, which would normally be at the south pole during this time, was shifted equatorward (Levine et al., 1977). Most dust storms are generated regionally by either baroclinic or *barotropic instability* or some combination of the two. However, there are additional factors which contribute to the growth of larger storms. In southern summer, the meridional overturning (Hadley) cell is latitudinally more extensive than in northern summer, leading to hemispheric transport of dust and other tracers that can cause a localised dust storm to rapidly expand. This triggers further growth in intensity and latitudinal extent of the Hadley cell and an additional increase in surface pressure, turning a localised storm into a global one (Kahre and Haberle, 2010, Read et al., 2015)

1.3.3. CO_2

Over the course of a Martian year, up to 30% of Mars's atmospheric CO_2 is condensed in the polar caps, while sublimation and precipitation of polar CO_2 ice affects the global atmospheric pressure by ~20% (Forget et al., 1998, Mangan et al., 2017, Tillman et al., 1993). Temperatures at the winter pole can sometimes reach <145 K, colder than the frost point of CO_2. As a result, dry ice condensation develops throughout the polar atmosphere, leading to spontaneous formation of a "polar hood" cloud at altitudes ≤25 km (Mangan et al., 2017, Read et al., 2015). Polar hood clouds increase greenhouse warming due to their scattering capabilities at almost all visible and infrared wavelengths. While they are also reflective at almost all wavelengths, there are some exceptions, most notably the 15 µm band and, to a lesser extent, the bands located around 2.7 µm and 4.3 µm, resulting from CO_2's strong vibration-rotation absorption at these wavelengths. It should be noted, however, that at lower temperatures and pressures the 15 µm band becomes saturated, making it a less efficient IR absorber. Regardless, these bands together absorb ~20% of surface thermal emission – a lesser greenhouse effect than that seen on Earth but still significant nonetheless. Another band of note is the 1.4 µm CO_2 band, which provides substantial thermal absorption at altitudes >30 km and results in dayside heating rates of >20 $K \cdot d^{-1}$. At altitudes >60 km, this can also involve non-local thermodynamic equilibrium effects because of direct radiative perturbations to CO_2 molecule energy level populations. This can have major impacts on computations of Mars's upper-middle atmospheric thermal structure (Read et al., 2015).

Beyond the polar regions, CO_2 clouds can also be found (i) during the day above the equator at altitudes of 65-85 km, (ii) at night above the subtropics at altitudes of 80-100 km, and (iii) above the mid-latitudes at altitudes of 53-62 km. These clouds are typically formed when the mesospheric temperatures drop below 100 K as a result of gravity wave propagation (Mangan et al., 2017).

1.3.4. H_2O

On a global scale, clouds concentrate water vapour in two regions: (1) close to the surface as fog and (2) at altitudes of 10-30 km near the equator and mountain regions. This has the potential to amplify vapour exchange with the surface and affect large scale atmospheric transport. These clouds also cause the magnitude of the Martian hydrological cycle to double, yet water vapour is only a small part of the Martian atmosphere, amounting to no more than 100 precipitable microns (pr µm, a unit of column number density equal to 3.34×10^{18} cm^{-2}) (Iraci et al., 2010, Read et al., 2015). Most of this (99%) is found below an altitude of 40 km, and 90% of that is found below an altitude of 20 km. Yet despite the fact that it is almost exclusively concentrated at the near-surface level, it is also the most variable trace gas observed because of its interactions with atmospheric circulation, cloud formation, regolith, and surface ice deposits (Read et al., 2015, Steele et al., 2014a). In addition to water vapour, water ice clouds have a direct influence on Mars's radiative balance, and interactions with dust provide a further indirect influence. Whether water ice clouds are discernible in observations or not, even the most tenuous of these clouds affect diurnal temperature variations and, in turn, upper atmosphere thermal tides. They are also responsible for atmospheric cooling at altitudes <15 km and atmospheric warming at altitudes of 15-40 km (Read et al., 2015).

Mars's annual global water cycle is primarily controlled by the sublimation and transport of H_2O from the polar caps, particularly the north pole where a permanent residual water ice cap is found (Steele et al., 2014a). This cap becomes exposed in northern spring once the CO_2 ice cap above it has sublimed. In addition to the polar regions, water ice clouds are, like CO_2, found to have an increased abundance over large topographical features such as the Tharsis Rise plateau (home to the giant Tharsis Montes shield volcanoes) and Arabia Terra. In addition to condensation processes related to elevation, it is thought that this may be at least partially due to regolith-atmosphere interactions (Steele et al., 2014a). Tropical water ice clouds tend to be found at higher altitudes and have greater density-scaled opacity in southern summer compared to northern summer. During southern summer, the cloud base and top create a substantial haze in the vertical since they are

separated by about an order of magnitude in pressure. At the solstices, these clouds can extend into the lower mid-latitudes (McCleese et al., 2010).

1.3.5. Modelling

As with GCMs which model Earth's atmosphere, Mars models must be constrained and validated by observations. This poses some problems for Mars models, particularly with regard to the impacts of dust on the atmosphere. Dust observations for Mars are spatially and temporally limited in scope, making retrieval of basic scattering parameters – *attenuation coefficient* Q_{ext}, *single-scatter albedo* ω, and *asymmetry factor* g – and key physical parameters such as column dust optical depth (CDOD – which is related to Q_{ext}) a troublesome, poorly constrained inverse problem, especially for predictive climate models (Madeleine et al., 2011, Montabone et al., 2015). There have been significant discrepancies in the past between the derived parameters and observational data, which heavily impacts on the implied solar heating rates. One such discrepancy was the underestimation of ω, which rendered GCMs unable to make realistic temperature predictions when both observed dust radiative properties and column opacity were used simultaneously *unless* the model was driven by a tuned opacity, at which point the model was no longer self-consistent (Madeleine et al., 2011).

CDOD datasets can still be used to reconstruct recent climatology and seasonal variability, though one must be cautious when interpreting the results. Montabone et al. (2015) used CDOD datasets to generate an eight-year 2D dust climatology and a set of dust scenarios for use in GCM experiments. Their results indicated an annual cycle of background CDOD. The second half of the Martian year appeared to be the most active, exhibiting a repeatable pattern with the following three phases:

1. Increasing aerosol dust in equatorial/southern tropical latitudes prior to southern spring equinox. Peak increase in aerosol dust between southern spring and summer, when northern high-latitude baroclinic activity favours cross-equatorial flushing dust storms,
2. Sublimation of southern polar CO_2 followed by significant dust lifting in the region during southern summer. Atmospheric dust markedly decreases at all other latitudes just prior to southern summer solstice, coinciding with a brief decrease in northern low-altitude baroclinic wave amplitudes (known as the "solstitial pause"), and
3. Late peak in dust optical depth between southern summer and autumn.

Despite this repeatable pattern, the occurrence of global dust storms is highly unpredictable.

During the eight-year period examined by Montabone et al. (2015), global dust storms developed only in Martian Year (MY) 25 and MY 28 (corresponding to Earth years (EY) 2001 and 2007 respectively). They also compared two storms which developed at the same location: the MY 25 global dust storm and a regional storm in MY 32 (EY 2014), both of which developed just after southern spring equinox. They found that CDOD values in spring and summer for both years were consistent with the first half of the aforementioned phase (1) but shortly into the second half, the MY 32 storm increased in size with an easterly trajectory, whereas the MY 25 storm increased in size with a westerly trajectory. They could find no apparent explanation for these contradictory trajectories, nor could they explain why the MY 25 storm became global while the MY 32 storm remained regional. Recent research has shown that water vapour reaches the middle atmosphere during global dust storms but not during regional ones (Heavens et al., 2018). In comparing the MY 28 and MY 32 storms, Heavens et al. (2018) found that the tropical hygropause (the altitude at which water content rapidly drops to zero) was situated at ~50-55 km during the MY 32 storm season but was raised to 75-80 km during the MY 28 storm season. This could be attributed to higher potential moistening rates above 50 km during MY 28, though latitudes north of 55°N showed no appreciable water transport within vertical dust advection that year. It's possible that water observed in the higher northern latitudes was advected in the descending branch of the Hadley cell such that the dust was removed from the atmosphere, but the water was not. However, water vapour content in the middle atmosphere increased at ~65°N before significant amounts of dust could reach that latitude, suggesting that dust advection was not the direct cause of the increased vapour content (Heavens et al., 2018). There may be interactions between the solstice cross-equatorial cell, the north-south topographical asymmetry, the east-west dust content asymmetry, the two transient baroclinic wave modes, and atmospheric circulations at different scales that have not yet been identified.

Several Mars GCMs capable of appropriately integrating dust have already been developed. Examples include the NASA Ames and Laboratoire de Météorologie Dynamique GCMs, which will be discussed in Chapter 2. THOR, which was ostensibly developed to investigate a wide range of planetary regimes, is used in this work to generate new results and compare them with those from existing models to explore the interaction between Mars's orbital evolution, dust, and climate.

CHAPTER 2 – MODELS AND METHODS

2.1. ABOUT GCMs

To investigate the atmospheric circulation of any planet, a General Circulation Model (GCM) should be employed. GCMs are three-dimensional models capable of solving elaborate physical and dynamical equations that represent *radiative transfer*, *convection*, *momentum*, *heat flux*, and fluid flow In so doing, a 3D model of atmospheric circulation and thermal structure is created (Madhusudhan et al., 2016, Mendonça et al., 2016). They can also be used to produce observables and examine their connection to planetary properties (Gómez-Leal et al., 2016). These models were originally designed to study Earth's atmospheric circulation and climate but have more recently been adapted to study solar system bodies and exoplanets (Gómez-Leal et al., 2016, Madhusudhan et al., 2016, Mendonça et al., 2016).

In general, we can divide GCMs into two types: spectral and grid-point. Spectral models are numerically more accurate and less noisy than grid-point models but are far less efficient at high resolutions and struggle with large gradients and discontinuities (Mendonça et al., 2016, Zalucha et al., 2013). As such, many GCMs are run on a grid-point basis. These grid-point models can be further subdivided into "primitive" models (those which assume hydrostatic equilibrium and synoptic scale hydrostatic dynamics, ideal gas laws, and a shallow atmosphere) and "comprehensive" models (those which can account for mesoscale non-hydrostatic dynamics and a "deep" – i.e. comprehensive – atmosphere) (Adcroft et al., 2004b, Selsis et al., 2011, White et al., 2005).

Two widely used primitive models are the NASA ARIES/GEOS model and the Laboratoire de Météorologie Dynamique (LMD) GCM, both of which were originally designed to study Earth's atmosphere but have since been adapted to study solar and extrasolar planets. ARIES/GEOS was adapted for Mars to become the NASA Ames Mars GCM (MGCM), which incorporates a two-stream radiative transfer solution for plane-parallel atmospheres that accounts for scattering and absorption by CO_2, H_2O, and dust (Haberle et al., 2003a). The LMD GCM combines physical schemes (radiative transfer, atmospheric chemistry, etc) with a spectral dynamical core, a semi-Lagrangian advection scheme, vertical energy and angular momentum conservation, and parameterisation of clouds, convection, and small-scale turbulence (Gómez-Leal et al., 2016, Steele et al., 2014a, Turbet et al., 2016). Model versions exist for Venus, Mars, Titan, Triton, and three planets (c, d, and g) in the Gliese 581 system (Selsis et al., 2011, Steele et al., 2014b, Turbet et al., 2016). Work is currently

being done to consolidate all of these model versions into a single, unified dynamical core model (Millour et al., 2013).

One drawback of the Ames MGCM is that it predicts lower IR and higher UV optical depths than are seen in observations. Moreover, neither the observed timing of the annual peak IR and UV optical depths nor the observed seasonal variations in apparent particle size are captured by the model (Kahre et al., 2017). The LMD MGCM, on the other hand, exhibits temperature biases in thermal structure at the poles. Cold biases are evident in the upper atmosphere above cloud-forming height over the summer pole in each hemisphere, which appear to be related to the model's dust distribution. An additional warm bias over all other latitudes is due to modelled thermal tides. Cloud radiative heating appears to strengthen the meridional circulation in the LMD model but this strengthening also seems to exacerbate its temperature biases – ∼6-8 K for polar warmings and ∼2 K in the tropics. Positions and wind speeds of high latitude jets are also affected by this due to changes in meridional temperature gradients. These biases have been improved by including ice and temperature assimilation schemes but the problem has not yet been fully resolved (Steele et al., 2014b).

The underlying assumptions of the primitive equations improve GCM performance without compromising accuracy in the Earth case but these assumptions may not be valid for some planetary atmospheres (Mendonça et al., 2016) and a comprehensive model is then required. A notable example is the MITgcm, which was designed originally for Earth use but has since been adapted for Mars, Pluto, and hot Jupiters HD209458b and HD189733b (Zalucha et al., 2013). While it can be used to solve the primitive equations, it is fully capable of operating non-hydrostatically and includes a thermodynamic equation with a user-specified external heating term (Adcroft et al., 2018). Like the Ames MGCM, it incorporates a two-stream radiative transfer scheme.

Earth-centric and Earth-derived GCMs have become incredibly robust, but in addition to the abovementioned primitive assumptions, certain approximations used in solving radiative transfer and chemical processes do impose limitations on accuracy (Gómez-Leal et al., 2016, Madhusudhan et al., 2016, Mendonça et al., 2016). They also tend to lack self-consistency – i.e. focusing on some aspects while ignoring or approximating others (Madhusudhan et al., 2016). Furthermore, observations of solar and extrasolar planets have highlighted a very diverse range of planetary

climates for which Earth-centric and Earth-derived GCMs are unlikely to be suited to (Mendonça et al., 2016). This and the sheer number of bespoke models which have been created for individual exoplanets [see Zalucha et al., 2013 for an extensive – though by no means exhaustive – list of such models] highlights the need for a new generation of self-consistent, flexible GCMs capable of adapting to a wide range of planetary conditions and climates without compromising accuracy (Mendonça et al., 2016, Zalucha et al., 2013). One such model is THOR, developed from first principles by Mendonça et al. (2016), which solves the 3D nonhydrostatic compressible Euler equations on a rotating sphere (Mendonça et al., 2016, Mendonça et al., 2018a). The primitive equations and underlying assumptions have still been included in THOR, but the model allows the user to switch these on and off, depending on the user's needs.

In addition to the primitive and comprehensive difference outlined above, two other key differences exist between the main models presented. The first relates to grid type. Both the Ames MGCM and the LMD GCM use a simple latitude-longitude cylindrical projection grid. This grid is well-known for its "pole problem" where the lines of longitude converge at the poles, resulting in smaller and smaller zonal grid spacing and an ever-decreasing time step. In order to maintain model stability, time steps at high latitudes have to be constrained with Fourier filtering (Adcroft et al., 2004a, Mendonça et al., 2016, Zalucha et al., 2013). The MITgcm solves this problem by using a cubed-sphere grid, but THOR uses a modified icosahedral grid instead. The icosahedral grid has a higher uniformity and isotropy than a cubed-sphere grid and can be divided over and over into triangular sections to improve resolution. This is achieved using a recursive method whereby the original spherical equilateral triangles are sub-divided into one equilateral triangle and three isosceles triangles (Figure 1). The equilateral triangle is then subdivided the same way again while the isosceles triangles are sub-divided into two isosceles triangles and two general spherical triangles (Mendonça et al., 2016). Since this results in not one but three different triangle types, all with different areas, a "spring dynamics" smoothing method is applied. Here, springs are attached to each grid point and the whole system is integrated with a magnitude 0.01 timestep until the net force applied to each grid point is no more than 10^{-5} in magnitude. Each triangle's control volume is then re-centred to its new centroid to complete the smoothing process (Mendonça et al., 2016).

The second difference between the main models presented here is their use of Arakawa gridding. MITgcm, Ames MGCM, and LMD GCM all use the Arakawa-C grid (Adcroft et al., 2018, Haberle et

al., 2003a, Millour et al., 2013). This is a staggered grid which separates the evaluation of vector quantities. For example, in a square grid one might evaluate the north-south velocity components at the centres of the upper and lower square faces and the east-west velocity components at the left and right square faces, rather than evaluating all components at the centre of the square itself. THOR uses an Arakawa-A grid – an unstaggered grid type where all physical variables are defined at the centre of each triangles' control volume. This makes it easier to construct higher order accuracy schemes, but it also uncouples neighbouring points from each other. Arakawa-C grids have double the resolution of Arakawa-A grids, but they also make inertia gravity waves less accurate. Arakawa-A grids are, however, more computationally efficient and have been successfully tested on icosahedral grids (Mendonça et al., 2016). The grid noise and instability associated with the unstaggered grid is reduced through the use of the abovementioned spring dynamics scheme (Mendonça et al., 2016, Tomita et al., 2001).

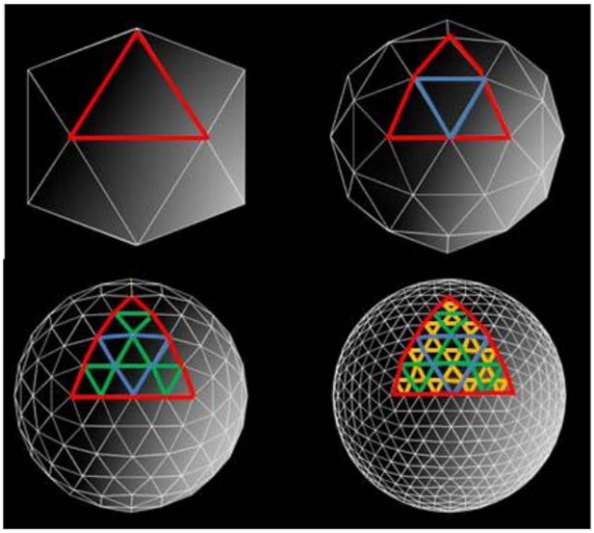

Figure 1: Grid refinement using a recursive method, which consists of bisecting each edge and projecting the new points on the sphere (taken from Mendonça et al. (2016))

In comparing the two main comprehensive models listed here (THOR and MITgcm), there is one more difference to note. Real atmospheres transfer kinetic energy from larger to smaller scales but in model atmospheres, some of this transfer occurs at unresolved scales, leading to drifts in mean circulation (Adcroft et al., 2018, Mendonça et al., 2016). The MITgcms, like many others, deal with this by using the flux form of the total energy equation, although this can lead to false local conversions between available and unavailable potential energy (Adcroft et al., 2018, Mendonça et al., 2016). At present, THOR instead uses the entropy equation, which helps to globally and uniformly adjust the internal energy at all grid points.

In all, THOR's main advantages over other models are its icosahedral grid, which circumvents the pole problem with a higher degree of isotropy, and the complete representation of resolved fluid flow without compromising the approximations that are common to adapted Earth models (Mendonça et al., 2016).

2.2. ABOUT THOR

THOR is part of the Exoclimes Simulation Platform (ESP) – a family of codes designed to simulate various aspects of exoplanetary climates. THOR runs in a GPU environment, which is more power and cost efficient than a CPU and facilitates parallel computing, but it is not without its limitations. First, the model currently assumes that the simulated atmosphere is not ionised (this is not the case for any planet that has a very hot or highly irradiated atmosphere) and that the effective gravity of the planet is constant and radial (which is not always valid in deep atmospheres), although modules to improve these cases are in development. Second, an explicit numerical dissipation scheme is used to keep the model numerically stable; however, in this scheme, diffusion strength is tunable and is invariant with latitude or longitude. Nonlinear diffusion strength formulations are currently being investigated to see whether they handle this problem any better. Lastly, though this is common to all non-Earth GCM adaptations as well, source and sink balances for quantities such as angular momentum and total energy are still largely unknown. This affects the assessment of the model's accuracy and robustness (Mendonça et al., 2016).

THOR has, to date, passed two benchmark tests: one for Earth and one for a generic hot Jupiter (Mendonça et al., 2016), yet it has only been used to fully simulate WASP-43b, a tidally locked hot Jupiter orbiting a K7 dwarf star with an orbital period of 19.2 hours (Mendonça et al., 2018a, Mendonça et al., 2018b). A previous GCM study of WASP-43b's near-infrared phase curves compared the effects of 1x and 5x solar composition on the planet's atmospheric circulation, longitudinal temperature distribution, and thermal structure, then simulated multi-wavelength phase curves and emission spectra for different orbital phases (Kataria et al., 2015). That study, however, solved the primitive equations while performing multi-wavelength radiative transfer. Another study had used the same phase curves with another primitive model to generate brightness temperature maps for 15 spectrophotometric channels, allowing the researchers to make inferences about the presence and circulation of atmospheric water vapour (Stevenson et al., 2014). Many other previous studies had shown that GCM results for hot Jupiters could generate large uncertainties on the order of tens of percent due to trade-offs between computational feasibility

and sensitivity to grid choices, computational methods, and numerical dissipation schemes. Hence, simulating any exoplanets with multiple GCMs would help to identify the main sources and drivers of uncertainty (Mendonça et al., 2018a). As such, Mendonça et al. (2018a) used THOR to provide a second opinion of the results found in Kataria et al. (2015). They used a "double-grey" radiative transfer scheme while solving the non-hydrostatic Euler equations. They also included enhanced CO and CO_2 (as constrained by the data), as well as a simple cloud parameterisation scheme, called into the model as an external module. Results showed that cloudfree runs were poor matches to the data. The different treatment of opacity meant that the resulting thermal structure was different to that found in previous studies and thus yielded different predictions for cloudfree phase curves. However, cloudy THOR runs were well-matched with observations, especially when CO_2 was enhanced with the 4.5 μm phase curve. Both the cloudy and cloudfree THOR runs and the previous study showed the presence of an equatorial jet – a trait exhibited by all hot Jupiters. However, Mendonça et al. (2018a) noted that simulations would benefit from upgrading THOR's radiative transfer scheme to one that handles multiple wavelengths simultaneously without needing any post-processing. In a subsequent paper, Mendonça et al. (2018b) ran further cloudy simulations on WASP-43b. The model was coupled to FastChem (another ESP code) and results were post-processed with a more sophisticated radiative transfer model to assess the planet's chemical diseqilibrium and its effect on observed emission spectra. They found that zonal transport was the dominant process affecting chemical distribution. One limitation of the study was the lack of included photochemical effects, which the authors hope to address in later work. In addition, the cloud parameterisation used in both studies is highly crude – it assumes that opacity is constant over the planet's night side. The acquisition of a visible, reflected light curve at higher resolution could constrain longitudinal cloud distribution, as in the case of Kepler-7b. While this is not yet possible for WASP-43b with current instruments, it may be obtainable once the James Webb Space Telescope (JWST) and Extremely Large Telescope (ELT) launch in 2021 and 2024 respectively (ESO, 2018, NASA, 2018).

While THOR has passed a benchmark test for Earth, it has not yet been used to study an Earth-like planet. This work will test THOR's performance on Mars. In particular, the role of atmospheric dust is investigated by changing longwave optical depth to reflect low, moderate, and high atmospheric dust loading. Additionally, the role of obliquity on climate is examined by comparing extreme obliquity regimes for Mars with the atmospheric state associated with Mars's current obliquity. Changes to these parameters are outlined in detail in Section 2.3.4.

2.3. MODEL SETUP

In THOR, there are three main equations which characterise the dry atmospheric flow, as described by (Mendonça et al., 2016). The first and most fundamental of these describes conservation of dry mass:

$$\frac{\partial \rho}{\partial t} + \nabla \cdot (\rho \boldsymbol{v}) = 0 \quad (1)$$

where ρ is the atmospheric density and $\boldsymbol{v}$ is the velocity.

The second is representative of Newton's second law of fluid motion, described by:

$$\frac{\partial \rho \boldsymbol{v}}{\partial t} + \nabla \cdot (\rho \boldsymbol{v} \otimes \boldsymbol{v}) = -\nabla p - \rho g \hat{\boldsymbol{r}} - 2\rho \boldsymbol{\Omega} \times \boldsymbol{v} \quad (2)$$

where $\otimes$ is the tensor product, p is pressure, g is gravity, $\hat{\boldsymbol{r}}$ is the radial unit vector, and $\boldsymbol{\Omega}$ is the planetary rotation rate. The pressure is recovered using the following equation:

$$p = p_{\mathrm{ref}} \left(\frac{R_d (\rho \theta)}{p_{\mathrm{ref}}} \right)^{\frac{C_p}{C_v}} \quad (3)$$

where p_{ref} is a reference pressure level, R_d is the gas constant for dry air, C_p is the specific heat capacity at constant pressure, and C_v is the specific heat capacity at constant volume. The potential temperature, θ, is also used in the final equation, which represents the thermodynamic equation in the flux form for entropy:

$$\frac{\partial \rho \theta}{\partial t} + \nabla \cdot (\rho \theta \boldsymbol{v}) = 0 \quad (4)$$

Entropy and potential temperature are tightly linked, thus the specific entropy S is defined as

$$dS = C_p d(\ln \theta) \quad (5)$$

A list of basic input parameters for the simulations can be found in Table 1. As per Mendonça et al. (2018a), the horizontal resolution was set to 4° with 40 vertical layers up to an altitude of 100 km. A number of earlier Mars models set the tops of their model domains to altitudes between 30 km and 80 km (Barnes and Haberle, 1996, Lewis et al., 1999, Urata and Toon, 2013). However, a model domain top above 80 km facilitates full development of Martian Hadley circulation and enables adequate simulation of polar mesospheric warming. Such warming is a non-negligible component of the polar radiation budget, particularly during dust storms (Forget et al., 1998, Forget et al., 1999). Hence, an altitude of 100 km was chosen for THOR's Martian simulations. The tuning parameter β, required for spring dynamics calculations, was set to 1.15. As per Tomita et al. (2002), if $\beta < 1.1$, the ratio of maximum grid interval to minimum grid interval (l_{max}/l_{min}) exceeds the convergence level of the standard grid system and the magnitude of Rossby wave discretisation errors increase. The ratio l_{max}/l_{min} also increases as horizontal resolution increases. If $\beta > 1.2$, the grid doesn't approach anything close to an equilibrium state. If $\beta = 1.2$, the values of l_{max}/l_{min} are the same regardless of

horizontal resolution, the Rossby wave errors are most reduced, and the grid is in its most homogeneous state. However, Heikes et al. (2013) found that their simulations were only stable up to a value of $\beta = 1.1$. For the above reasons, a value of $\beta = 1.15$ was adopted for this work, a value which was also adopted by Mendonça et al. (2016). The model was initialised from a rest atmosphere with an isothermal temperature profile and integrated for 1220 days, starting from a solar longitude (i.e. position in orbit) of 0°. This corresponds to the Martian southern autumnal equinox, which marks the beginning of a Martian year. The 1220 days modelling time includes almost 1.5 Martian years (where one Martian year is 687.5 Earth days) and a spin-up time of precisely 203.125 Earth days, with a timestep of 300 seconds duration and output files generated every 1500 seconds.

Table 1: Input parameters used in THOR's Mars simulations. See Appendix 3 for a full list of input parameters and enabled schemes.

VARIABLE	VALUE	SOURCE
Stellar temperature, $T_\odot$	5772 K	(Williams, 2018a)
Stellar radius, $R_\odot$	1 $R_\odot$ (solar radius)	–
Orbital distance, d	1.52366231 AU	(Williams, 2018b)
Planet radius, r	3396.2 km	(Williams, 2018b)
Rotation rate, ω	7.078 x 10^{-5} rad s^{-1}	Converted from Williams (2018b)
Gravitational acceleration, g	3.71 m s^{-2}	(Williams, 2018b)
Gas constant, R_d	191.84 J kg^{-1} K^{-1}	(Urata and Toon, 2013)
Specific heat capacity [of dry air], C_p	750 J kg^{-1} K^{-1}	(Urata and Toon, 2013)
Mean atmospheric temperature, T	210 K	(Williams, 2018b)
Reference surface pressure, p	636 Pa	(Williams, 2018b)
Bond albedo, A	0.25	(Williams, 2018b)
Mean orbital velocity, Ω	1.05 x 10^{-7} rad s^{-1}	Converted from Williams (2018b)
Orbital eccentricity, e	0.09341233	(Williams, 2018b)
Longitude of periastron, ϖ	336.04084°	(Williams, 2018b)
Current obliquity, ε	25.19°	(Williams, 2018b)

2.3.1. Enabled schemes

Previous research has indicated that Mars's large-scale topography – particularly the Tharsis Montes region – induces mesoscale circulations which vertically transport large amounts of water vapour, dust, and other aerosols above 40 km in altitude where they can then enter the global circulation (Michaels et al., 2006). This important interplay between mesoscale (non-hydrostatic) and synoptic (hydrostatic) processes should not be discounted in Martian simulations. The hydrostatic approximation used in many GCMs neglects the acoustic terms required to simulate the propagation of vertical acoustic waves, which becomes problematic for resolving some mesoscale processes (Mendonça et al., 2016). As such, non-hydrostatic dynamics have been enabled in THOR for this work. The deep atmosphere scheme has also been enabled. While a shallow atmosphere

approximation is perfectly valid for planets with thin atmospheres (like Mars or Earth), it neglects the Coriolis terms in the horizontal components of planetary angular velocity in order to conserve axial angular momentum. Deep models have been shown to provide similar results to shallow models without compromising angular momentum conservation, regardless of the type of planet under consideration (Mendonça et al., 2016, White et al., 2005).

A dry convective adjustment scheme has been included in recent updates of THOR which vertically mixes atmospheric entropy while conserving total column enthalpy when the lapse rate becomes super-adiabatic (Mendonça et al., 2018a). This scheme has been enabled for Mars simulations in this work, as a daytime super-adiabatic near-surface layer has been observed by the Miniature Thermal Emission Spectrometer aboard the Mars rovers "Spirit" and "Opportunity" (Smith et al., 2004).

2.3.2. Diffusion and damping

2.3.2.1. Hyper-diffusion and divergence-damping

Including explicit linear horizontal diffusion – particularly 4th-order hyper-diffusion – is common in GCMs. Hyper-diffusion is often included to maximise the enstrophy-to-energy dissipation ratio (where enstrophy is a quantity representing the kinetic energy of a fluid generated by turbulence, corresponding to dissipation effects) and is preferred over 2nd-order diffusion schemes which have poor scale selectivity and thus negatively impact well-resolved scales. Implementation of any kind of explicit horizontal diffusion, though, tends to be physically inconsistent. Dissipation irrevocably converts mechanical energy to thermal energy, and this process should be represented as a positive frictional heating term in the thermodynamic equation. Such friction is almost always ignored in GCMs because its contribution to the heat budget is so small, yet over time, neglect of this term violates the conservation of total energy and (if hyper-diffusion is applied) axial angular momentum (Jablonowski and Williamson, 2011, Mendonça et al., 2016). THOR is no exception; as seen in Eq. 4, it, too, neglects frictional heating, although a conservation scheme has been included (and enabled in this work) which uniformly adjusts the internal energy at all grid points in order to conserve mass, total energy, and angular momentum (Mendonça et al., 2016).

When using grid point models, it is necessary that they obey the Courant-Friedrichs-Lewy (CFL) convergence condition in order to maintain model stability. This is particularly problematic for latitude-longitude grids, although THOR's modified icosahedral grid is able to relax this condition to

some extent. To fully satisfy the CFL condition horizontally, however, a split-explicit time-stepping scheme is required. Such a scheme uses short, explicit timesteps to correctly resolve fast acoustic wave modes and large timesteps to resolve everything else. This scheme improves time-integration performance but can produce spurious high-wavenumber modes. To combat this, 3D divergence-damping – itself a form of hyper-diffusion- is used to damp this noise (Jablonowski and Williamson, 2011, Mendonça et al., 2016, Ullrich et al., 2018).

In THOR, hyper-diffusion is represented by the following equations (Mendonça et al., 2016):

Diffuse flux for density (ρ)

$$F_\rho = -\nabla_h^2 K_d \cdot \nabla_h^2 \rho \tag{6}$$

Dissipative fluxes for momentum (ν) projections

$$F_{\nu_{hx}} = -\nabla_h^2 K_d \nabla_h^2 \nu_{hx} - K_d \nabla_h^2 \nabla_h (\nabla_h \cdot (\rho \boldsymbol{\nu}_h) + \frac{1}{r^2}\frac{\partial}{\partial r}(\rho \nu_r r^2)) \tag{7}$$

$$F_{\nu_{hy}} = -\nabla_h^2 K_d \nabla_h^2 \nu_{hy} - K_d \nabla_h^2 \nabla_h (\nabla_h \cdot (\rho \boldsymbol{\nu}_h) + \frac{1}{r^2}\frac{\partial}{\partial r}(\rho \nu_r r^2)) \tag{8}$$

$$F_{\nu_{hz}} = -\nabla_h^2 K_d \nabla_h^2 \nu_{hz} - K_d \nabla_h^2 \nabla_h (\nabla_h \cdot (\rho \boldsymbol{\nu}_h) + \frac{1}{r^2}\frac{\partial}{\partial r}(\rho \nu_r r^2)) \tag{9}$$

$$F_{\nu_r} = -\nabla_h^2 \rho K_d \nabla_h^2 \nu_r \tag{10}$$

*Diffuse flux for pressure field (*p*)*

$$F_{\mathrm{p}} = -R_d \nabla_h^2 \rho K_d \nabla_h^2 T \tag{11}$$

where K_d is the diffusion strength, $\boldsymbol{\nu}_h$ is the horizontal momentum vector, ν_r is the radial momentum, r is planet radius, R_d is the gas constant for dry air, and T is prognostic temperature. ∇_h is the spherical horizontal operator. When applied to any vector Φ_0 (for example $\boldsymbol{\nu}_h$), ∇_h denotes a divergence operator, given by:

$$\nabla_h \cdot \boldsymbol{\Phi_0} \simeq \frac{1}{A_c} \sum_{k=1}^{6(5)} F_k \tag{12}$$

where A_c is the area of the control volume, F_k is the flux at the edges of the control volume, C_k, and k is an index which can take any number between 1 and 5 or 6, corresponding to the edges of the hexagon or pentagon created by the triangles of the icosahedral grid.

When applied to any scalar s_0 (for example ν_{hx}), ∇_h denotes a gradient operator, given by:

$$\nabla_h \mathrm{s}_0 \simeq \frac{1}{A_c} \sum_{k=1}^{6(5)} l_k \frac{s_k^* + s_{k+1}^*}{2} \widehat{\boldsymbol{n}}_{\boldsymbol{k}} - \frac{s_0}{A_c} \sum_{k=1}^{6(5)} l_k \widehat{\boldsymbol{n}}_{\boldsymbol{k}} \tag{13}$$

where l_k is the geodesic arc length between control volume vertices and $\widehat{\boldsymbol{n}}_{\boldsymbol{k}}$ is the unit outward vector normal to the geodesic arc. Asterisks in the scalar terms denote that they are defined at the vertices of the control volume.

The second term ($K_d \nabla^2 \nabla_h (\nabla_h \cdot (\rho \nu_h) + \frac{1}{r^2}\frac{\partial}{\partial r}(\rho \nu_r r^2))$) in Eqs. 7-10 represents the 3D divergence-damping. In previous work by THOR developers (Mendonça et al., 2016, Mendonça et al., 2018a, Mendonça et al., 2018b) the strength of hyper-diffusion and the strength of divergence-damping

are taken to be the same value, both represented by K_d = 0.015. The choice of this value – in particular, the choice of the "nondimensional diffusion parameter" used to calculate the coefficient – is not elucidated in the literature or the model code. Such a lack of diffusion coefficient documentation is a pervasive problem in the climate modelling community (Jablonowski and Williamson, 2011). Tomita and Satoh (2004) refer to their diffusion coefficients as "empirical factors", implying that their values are chosen via experiment/observation, but this is not explained further. For simplicity, this work adopts the values chosen by THOR developers (K_d = 0.015) for now, although this may be revised at a later date.

2.3.2.2. Boundary conditions

Upper boundary conditions such as a rigid lid (in which the vertical velocity at the top of the model domain is hard set to zero) are used to conserve mass in GCMS but often result in spurious wave reflections at the top. One common mitigation strategy is to adopt a sponge layer in the upper layers of the model domain to ease the eddy component of the wind field to zero and absorb spurious reflections (Jablonowski and Williamson, 2011, Klemp et al., 2008, Mendonça et al., 2018b). Use of a sponge layer can compromise axial angular momentum (Mendonça et al., 2016) but for THOR this is addressed in the conservation scheme mentioned in the previous subsection.

As per Mendonça et al. (2018b), THOR's sponge layer scheme applies Rayleigh friction to the upper layers using a zonal/meridional projection rather than a 3D Cartesian projection, and is represented by the following equation:

$$\frac{d\Psi}{dt} = -\frac{1}{\tau}(\Psi - \bar{\Psi}) \qquad (14)$$

where Ψ represents the wind velocity components, $\bar{\Psi}$ represents the zonally averaged wind velocity, and $\frac{1}{\tau}$ is the damping strength (where τ is the relaxation timescale). To calculate the zonally averaged quantities, THOR decomposes its icosahedral grid into latitudinal rings and in this work, the number of rings is set to 20. A variable average is then calculated inside each ring. Finally, the zonal average is computed by linear interpolation in latitude of the average value of the rings. The damping strength is represented by the following equation:

$$\frac{1}{\tau} = \begin{cases} 0 & \text{if } \eta < \eta_s \\ k_s \sin^2\left(\frac{\pi}{2}\frac{\eta-\eta_s}{1-\eta_s}\right) & \text{otherwise} \end{cases} \qquad (15)$$

where k_s represents the greatest damping at the top of the model domain, which has been set to a value of 1 x 10^{-4} s^{-1}, equivalent to a relaxation time of ~8.5 days. The hybrid vertical coordinate

denoted by η represents normalised hydrostatic pressure, as per Skamarock and Klemp (2008), and decreases monotonically from η = 1 at the surface to η = 0 at the model top. This coordinate is determined by:

$$\eta = \frac{p_{\mathrm{h}} - p_{\mathrm{ht}}}{p_{\mathrm{hs}} - p_{\mathrm{ht}}} \tag{16}$$

where p_{h} is the hydrostatic component of pressure, p_{hs} is the surface pressure for dry atmosphere, and p_{ht} is the upper boundary pressure for dry atmosphere, set as a constant. As opposed to a standard pressure coordinate ($\sigma = p/p_s$, where p_s is the surface pressure), η varies smoothly from topography-dependent pressure at low levels to an isobaric pressure at higher levels and thus "naturally incorporates" a lower boundary condition rather than needing to specify one separately (Laprise, 1992, Sangster, 1960). Therefore, the fractional height denoted by η_s simply represents the percentage of the model atmosphere at which the sponge layer is first activated, with the damping function slowly increasing with altitude to avoid unintended creation of spurious waves (Mendonça et al., 2018b). In this work, as in previous work by THOR developers, η_s = 0.75.

2.3.3. Radiative transfer and radiative properties

2.3.3.1. Internal heat flux

The radiative transfer scheme used in this work is the same as the two-stream "double grey" scheme outlined in Appendix A of Mendonça et al. (2018a). The equivalent blackbody temperature of the planet's internal heat flux is required for calculation of the thermal emission equation and is a specifiable parameter in THOR's configuration file terms. This temperature is derived using the relation $\Phi = \sigma_{SB} T^4$, where Φ is a flux, T is a temperature in units of Kelvin, and σ_{SB} is the Stefan-Boltzmann constant 5.67 x 10^{-8} W·m^{-2}·K^{-4}. According to Hoffman (2001), Mars's internal heat flux is 28% of Earth's internal heat flux. Using a dataset consisting of more than 38,000 data points, Davies and Davies (2010) estimate Earth's total surface heat flow to be 47 $\pm$ 2 TW, which is equivalent to an average internal heat flux of ~91.6 mW·m^{-2}. This gives an average internal heat flux of ~26.4 mW·m^{-2} for Mars, and its equivalent blackbody temperature is thus T_{low} ~26.1 K. For simplicity, this has been rounded to T_{low} = 25 K in this work.

2.3.3.2. Diffusivity factor

Radiative heat flux and atmospheric cooling/heating rates require several integrations, including over the solar zenith angle; however, this angle is difficult to calculate exactly and so an approximation in the form of a diffusivity factor is made (Zhang and Shi, 2001). Traditionally, this

diffusivity factor is assumed to be r = 1.66 (Gierasch and Goody, 1967); however, the optimum value of this factor depends on the method used to calculate radiative heating. THOR uses the flux method, rather than the intensity method and, according to Apruzese (1980), the optimum diffusivity factor value for this method is 1.81, which is used in this work.

2.3.3.3. Optical depth of incoming stellar flux

The grey optical depth of incoming stellar flux, τ_{sw}, is derived from the equation for downward stellar flux in Appendix A of Mendonça et al. (2018a). With the solar path-length correction outlined in Eq. A2 of that paper, τ_{sw} is thus given by

$$\tau_{sw} = \ln\left[\frac{(1-A)F_\star}{F_{sw}^{\downarrow}}\right]\sqrt{1-\left(\frac{r}{r+z}\right)^2(1-\mu_0^2)} \qquad (17)$$

where A is the planet bond albedo, $F_\star$ is the stellar constant, $F_{sw}^{\downarrow}$ is the incoming downward flux, r is the planet radius, z is the altitude at the top of the model domain, and μ_0 is the cosine of the zenith angle. According to Appelbaum and Flood (1990), $F_\star$ = 1371 W·m^{-2} and $F_{sw}^{\downarrow}$ = 590 W·m^{-2} for Mars. Cronin (2014) suggests that an insolation-weighted cosine zenith angle of μ_0 = 2/3 should be used in place of the commonly used daytime-averaged cosine zenith angle of μ_0 = 0.5, as the latter value can lead to deficits in shortwave absorption. Thus, the insolation-weighted average has been adopted here. Taking all of this into account, a value of τ_{sw} = 0.45 was calculated for Mars.

2.3.4. Model variations

2.3.4.1. Surface heat capacity

Areal surface heat capacity, C_{surf}, was estimated using two techniques, and both of these estimates were used in THOR simulations of Mars. The first estimate was obtained using Eq. 2 from Cook et al. (2017), which calculates the heat capacity of Earth's ocean mixed layer. This equation has been slightly modified to be applicable to the Martian surface: instead of having terms be related to Earth's ocean mixed layer, the terms now represent Martian soil. The equation is thus:

$$C_{surf} = c_s \rho_s h_s \qquad (18)$$

where c_s is the average soil heat capacity, ρ_s is the average soil density, and h_s is the estimated total depth of the subsurface layers, given by 627.9 J·kg^{-1}·K^{-1}, 1500.0 kg·m^{-3}, and 2.8 m respectively (Urata and Toon, 2013). This results in an average C_{surf} of 2.6 x 10^6 J·K^{-1}·m^{-2} (hereafter referred to as C_2). The second estimate was obtained using Eq. 30 from Heng et al. (2011) for cases where the bottom of the model domain does not mimic a mixed layer ocean. This equation is written as:

$$C_{surf} = \frac{c_p P}{T^2}\left(\frac{k_{con}}{4 g_p \sigma_{SB} R_d}\right)^{1/2} \qquad (19)$$

where c_p is the specific heat capacity of the atmosphere at constant pressure, P is vertical pressure, T is the equivalent blackbody temperature of the internal heat flux, T_{low}, k_{con} is thermal conductivity, g_p is surface gravity, σ_{SB} is the Stefan-Boltzmann constant, and R_d is the ideal gas constant. Since Mars's crust is primarily composed of basalt, which likely has the strongest influence on the thermal properties of Mars regolith (Clifford, 1993), this work assumes a high-end basaltic value of k_{con} = 5.0 W·m^{-1}·K^{-1}, giving an areal heat capacity of C_{surf} = 1.8 x 10^5 J·K^{-1}·m^{-2} (hereafter referred to as C_1). It should be noted that, according to Clifford (1993), the column-averaged thermal conductivity could be closer to (2.0 $\pm$ 1.0) W·m^{-1}·K^{-1}, which would give an approximate C_{surf} value of (1.1 $\pm$ 0.3) x 10^5 J·K^{-1}·m^{-2}, and this may be explored with THOR at a later date.

2.3.4.2. Longwave optical depth

For the sake of simplicity, the grey optical depth of thermal wavelengths at the equator, τ_{lw}, takes into account the infrared absorption of both dust and CO_2, as there is currently no way to separate the radiative effects of each in THOR without coupling to or post-processing with another ESP module. Such combined treatment of dust and CO_2 is not uncommon – for example, Moudden and McConnell (2005) did exactly this for their radiative transfer code in the Global Mars Multiscale Model (GM3) to preserve the consistency of calculations. At any rate, dust is the predominant source of radiative heating, particularly in the lowest 50 km of the atmosphere, and so τ_{lw} should be seen as indicative of dust optical depth (Haberle et al., 2003b, Moudden and McConnell, 2005). Following the work of Barnes and Haberle (1996), Lewis et al. (1999), Moudden and McConnell (2005), and Urata and Toon (2013), three global dust regimes have been investigated under Mars's current obliquity: (1) "low-dust" with τ_{lw} = 0.3, denoting a mostly clear atmosphere; (2) "moderate-dust" with τ_{lw} = 2, representative of dusty average conditions; and (3) "high-dust" with τ_{lw} = 5, denoting strong global dust storm conditions. While much of the planet can be represented by these dust conditions, low emission zones at the polar regions are more likely to be created by the radiative properties of CO_2 polar hood clouds and snowfalls and tend to vary with time and dust content. The distribution of these polar low emission zones are well reproduced by values of $\tau_{lw,pole}$ = 0.1-0.3 during clear periods free of dust storms and $\tau_{lw,pole}$ = 1.5 during and after such dust storms (Forget et al., 1998). In this work, a $\sin^2\phi$ latitude dependence (where ϕ denotes latitude) has been enabled in the model so that values between τ_{lw} and $\tau_{lw,pole}$ vary as a function of latitude, rather than using a single value for τ_{lw} to represent the whole planet. A smaller value of $\tau_{lw,pole}$ = 0.1 was chosen for low-dust simulations but for moderate and high dust simulations, the value of $\tau_{lw,pole}$ =

1.5 is adopted, as per Forget et al. (1998). Power law indices are set to n_s = 2 and n_l = 4 for shortwave and longwave absorbers respectively, while the strength of the well-mixed longwave absorbers is set to f_l = 0.1 as per Heng et al. (2011).

2.3.4.3. Obliquity (ε) variations

To investigate the impacts of Mars's highly variable obliquity on the climate, simulations were carried out with the current obliquity value of ε = 25.19° and two extreme obliquity values identified in past Mars climate: ε = 0° and ε = 60°. These simulations were conducted under the low-dust scenario described above to separate obliquity impacts from dust impacts, although Haberle et al. (2003b) note that a low-dust scenario could be unrealistic for high obliquity regimes, since dust lifting seems to dramatically increase with increasing obliquity.

2.3.5. Comparison with previous works

Results from THOR's simulations will be compared with results from several models used in previous studies – specifically LMD and AOPP (Forget et al., 1999, Lewis et al., 1999), NASA Ames (Haberle et al., 2003b), Martian COMMA-IAP (Hartogh et al., 2005), GM3 (Moudden and McConnell, 2005), and Mars-GRAM 2000 (Justus et al., 2002). These models encompass six dust regimes, with longwave optical depths of τ_{lw} = 0.1, τ_{lw} = 0.18, τ_{lw} = 0.3, τ_{lw} = 0.4, τ_{lw} = 1, and τ_{lw} = 3. Ideally, THOR would have been used to simulate all of these but due to time constraints on this project, simulations were limited to the three dust regimes described in Section 2.3.4.2 of this chapter. To aid comparison, THOR's low-dust regime results are matched with the first four regimes (τ_{lw} = 0.1, τ_{lw} = 0.18, τ_{lw} = 0.3, and τ_{lw} = 0.4) from previous works, depending on the season or time of year for which those regimes were used. THOR's moderate- and high-dust regimes are matched with the τ_{lw} = 1 and τ_{lw} = 3 regimes from previous works, with THOR's high-dust regime representing a kind of "extreme" case compared to the other, more moderate regimes. These dustier regimes are examined only for southern summer (Mars's "dusty season"). All results are presented in Chapter 3 and discussed further in Chapter 4.

CHAPTER 3 – RESULTS

In this chapter, I present the results of the model variations described in Chapter 2, Section 2.3.4. Briefly summarised, the impacts of different surface heat capacity values are first assessed in Section 3.1 to determine which of these values is more appropriate for Mars simulations. Following this, results for a small region of the troposphere are compared against Mariner 9 and Viking Lander data with promising results in Section 3.2.1. In Sections 3.2.2-3, a significant problem is consistently observed in THOR's simulated troposphere for the low dust loading case. However, highly favourable results for moderate and high dust loading cases in Section 3.2.4 indicate that the problem may arise from the specification of shortwave radiation. In light of this, Section 3.3 not only compares results between low and high obliquity cases for low dust loading but also how these cases respond to a minimal (τ_{lw} = 0.1) dust loading. These results appear to confirm that the higher value for shortwave radiation (τ_{sw} = 0.45) is causing the effects observed in the low dust loading cases for low, high, and present-day obliquity. These results are discussed as a whole in Chapter 4, with potential solutions and avenues of future investigation put forward.

3.1. Assessment of areal (surface) heat capacity values

A key free parameter in THOR is the areal heat capacity, C_{surf}. This represents the capacity of the surface to absorb radiant energy. To develop a baseline model for THOR, the value of this parameter needed to be constrained, and simulations were performed with the two C_{surf} values calculated in Chapter 2, Section 2.3.4.1: $C_1 = 1.8 \times 10^5$ J·K^{-1}·m^{-2} and $C_2 = 2.6 \times 10^6$ J·K^{-1}·m^{-2}.

For space, graphic comparisons of C_{surf} results from low-dust model runs at current obliquity (ε = 25.19°), low obliquity (ε = 0°) and high obliquity (ε = 60°) are provided in Appendix 4A-F but the basic outcomes are as follows. Model runs using an areal heat capacity C_2, generally produced similar results to those using an areal heat capacity C_1. However, with the exception of low obliquity cases, which exhibited no change regardless of areal heat capacity value or time of year, C_2 also tended to produce greater extremes in temperature, an easterly wind bias with less accurate wind field structure, and an underestimation of vertical velocities when compared to C_1. Furthermore, simulations using C_2 with moderate dust loading failed, while simulations using C_1 did not. These results would seem to indicate that a higher areal heat capacity (calculated using Eq. 18) is too high to produce reliable simulations for Mars. As such, the focus of this work now turns to results obtained using C_1.

3.2. THE MARTIAN YEAR

Before progressing further, it is worth noting that Mars has twelve seasons, not four, which have been identified and tabulated in Lewis et al. (1999). Those seasons have been reproduced and elaborated upon in Table 2 of this work and graphically represented in Appendix 2, Figure 1 for ease of reference. Previous studies have focused on the equinoxes, solstices, or their corresponding seasons. To provide easier comparisons, this work focuses on these periods as well.

Table 2: Martian seasons according to Lewis et al. (1999). Solar longitude refers to Mars's position in orbit around the Sun at any given time throughout the year. A Martian solar day (sol) is the approximate equivalent of 1.03 Earth days.

Season	Solar longitude (L_s)	Martian sols	Earth days		Events
1	*0° - 30°*	*0 – 61*	*0 – 63*	*Southern autumn*	*Autumnal equinox at L_s = 0°*
2	30° - 60°	61 – 127	63 – 130		
3	60° - 90°	127 – 193	130 – 198		
4	*90° - 120°*	*193 – 258*	*198 – 266*	*Southern winter*	*Winter solstice at L_s = 90°*
5	120° - 150°	258 – 318	265 – 327		
6	150° - 180°	318 – 372	327 – 382		
7	*180° - 210°*	*372 – 422*	*382 – 434*	*Southern spring*	*Vernal equinox at L_s = 180°*
8	210° - 240°	422 – 468	434 – 481		
9	240° - 270°	468 – 515	481 – 529		
10	*270° - 300°*	*515 – 562*	*529 – 577*	*Southern summer*	*Summer solstice at L_s = 270°*
11	300° - 330°	562 – 613	577 – 630		
12	330° - 360°	613 – 669	630 – 687		

3.2.1. Season 2 – Comparing with Mariner 9 data (L_s = 43° – 54°)

In constructing their Mars Climate Database, Lewis et al. (1999) validated their results for low dust loading by comparing them to data obtained by the Infrared Interferometer Spectrometer (IRIS) aboard Mariner 9 during L_s = 43°-54° of Martian Season 2 in 1972 and to Viking observations modelled using a time-dependent dust-scenario developed specifically with those observations in mind. These comparisons were, in their words, "intended to reflect the current uncertainty in the appropriate background dust loading of the Martian atmosphere." Here, THOR's low dust loading results are compared with all three sets of results from Lewis et al. (1999) for this time period. Both the Mars Climate Database τ = 0.1 scenario and the time-dependent Viking dust scenario exhibit a temperature trough in the upper 25-30 km with a peak decrease at ~10°S (Figure 2.b and Figure 2.c). This same trough is observed in THOR's simulation for τ_{lw} = 0.3 (Figure 2.a), though the peak decrease occurs roughly at the equator and temperatures are overestimated by ~110 K. This trough is not observed in data acquired by Mariner 9 (Figure 2.d). THOR exhibits an astonishingly warm anomaly (> 360 K) above the northern polar latitudes and a cooler one (~280 K) above the southern mid-latitudes, which are not observed in any of the comparative figures. These anomalies continue

to recur throughout all of THOR's results for τ_{lw} = 0.3, as shown later in Sections 3.2 and 3.3 of this chapter and discussed in more detail in Chapter 4. However, temperatures in the lowest 5 km of THOR's results between 20°S and 55°S do match both Mariner 9 observations and the dust scenarios employed by (Lewis et al., 1999). Despite the unexpected warm anomalies, these results are encouraging.

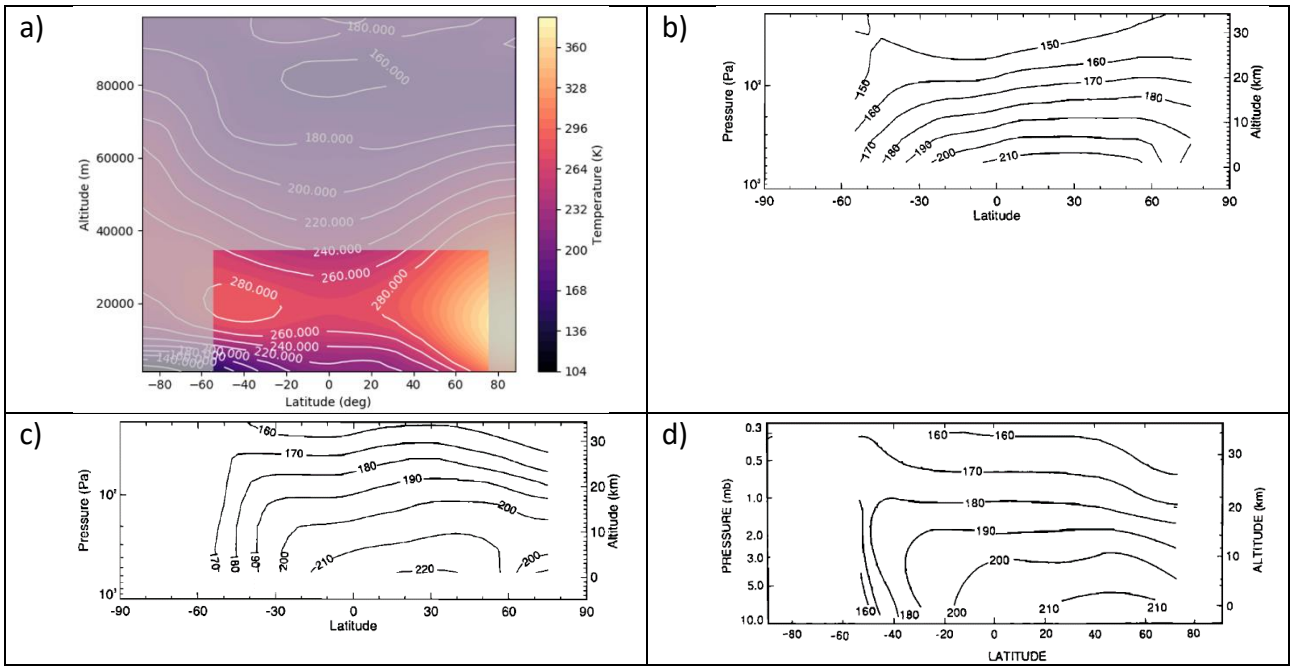

Figure 2: Comparison of a) zonal mean temperature for τ_{lw} = 0.3 as simulated by THOR, b) zonal mean temperature for τ_{lw} = 0.1 as simulated by the Mars Climate Database, c) zonal mean temperature using a time-dependent optical depth function for modelling Viking Lander observations, and d) temperature observations acquired by Mariner 9 IRIS. Figures (b) – (d) are taken from Lewis et al. (1999)

3.2.2. Southern autumn (L_s = 0° – 30°) and southern spring (L_s = 180° – 210°)

As demonstrated in Figure 3 for southern autumn and Figure 4 for southern spring, THOR performs reasonably well in the mesosphere (> 50 km altitude) and is comparable with the results obtained by Forget et al. (1999) using the LMD grid-point model and AOPP spectral model with a longwave optical depth value of τ = 0.4. THOR does seem to push the top of the mesosphere down from 100 km to 90 km, which is evident in both figures.

Areas of mid-level polar warming are evident in THOR between 60 km and 80 km altitude, stronger over the southern polar latitudes than the northern polar latitudes in southern autumn (Figure 3.a) but showing the reverse pattern in southern spring (Figure 4.a). The mid-level southern polar warming is larger and remains warm directly over the pole, in line with the AOPP model (Figure 3.a.ii, right, and Figure 4.a.ii, right), but less so with the LMD model (Figure 3.a.ii, left, and Figure

4.a.ii, left). Conversely, despite the warm anomalies centred above the polar to midlatitudes at an altitude of ~20 km and the general overestimation of low-level temperatures, THOR does reflect the skewed distribution of lower level warm temperatures toward northern polar latitudes, in line with the LMD model but slightly less so with the AOPP model. Cooling in the lowest 2-3 km above the polar to midlatitudes in both hemispheres is also evident and in line with both models.

The zonal wind results displayed in Figure 3.b.i and Figure 4.b.i are much less symmetric than those generated by both the AOPP and LMD models. The northern westerly jet has been shunted to a small area above the midlatitudes with a considerable loss of wind strength. While THOR correctly shows that the southern westerly jet is much stronger than its northern counterpart, the wind strength of both westerlies has been underestimated – in the case of the southerly jet, wind strength is underestimated by roughly half an order of magnitude. Conversely, the equatorial easterlies have been considerably overestimated by 70 $m \cdot s^{-1}$ (compared to the AOPP model) to 110 $m \cdot s^{-1}$ (compared to the LMD model).

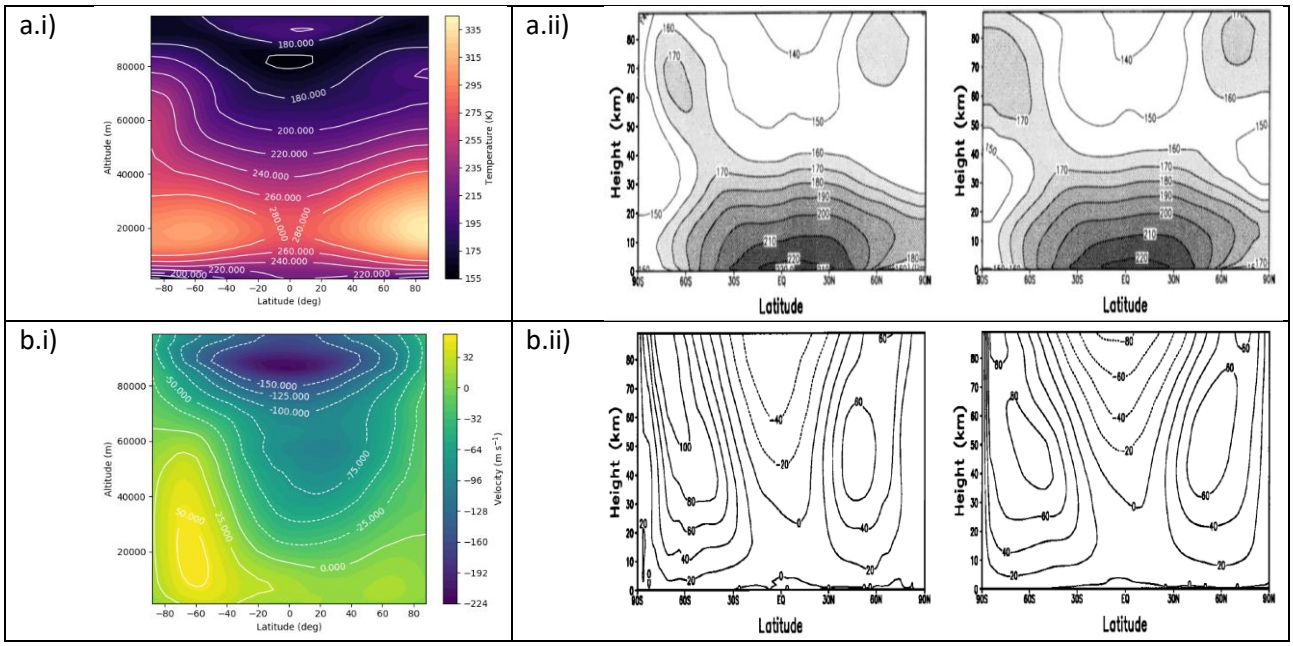

Figure 3: L_s = 0°-30°, seasonally averaged outputs for a) zonal mean temperature simulated by (i) THOR and (ii) LMD (left) and AOPP (right); b) zonal wind simulated by (i) THOR and (ii) LMD (left) and AOPP (right). All LMD and AOPP figures are taken from Forget et al. (1999) and are using a longwave optical depth of τ_{lw} = 0.4.

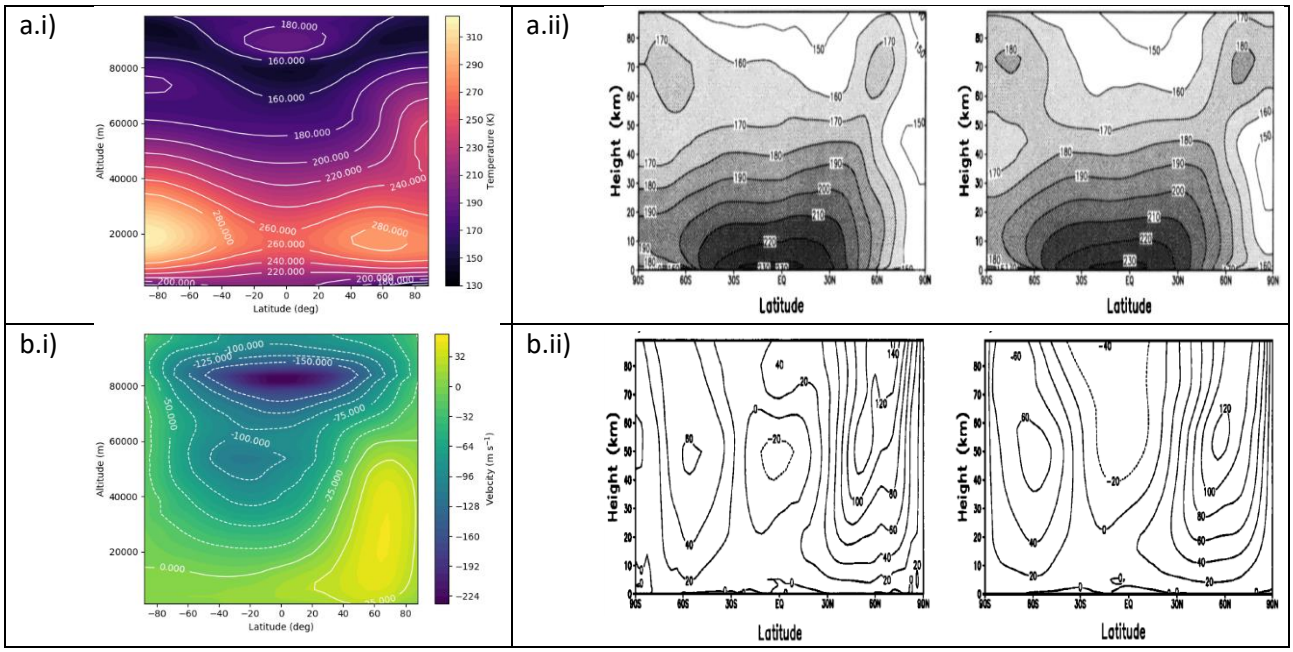

Figure 4: L_s = 180°-210°, seasonally averaged outputs for a) zonal mean temperature simulated by (i) THOR and (ii) LMD (left) and AOPP (right); b) zonal wind simulated by (i) THOR and (ii) LMD (left) and AOPP (right). All LMD and AOPP figures are taken from Forget et al. (1999) and are using a longwave optical depth of τ_{lw} = 0.4.

In comparing THOR's vernal equinox results to previous work and TES observations (Figure 5 and Figure 6), it is obvious that THOR is able to capture the almost-symmetry of a Martian equinox reasonably well. As seen in Figure 5, the mesospheric polar warming lobes are evident, as is the mesospheric equatorial cooling. There is, however, a warm region above this that is not present in the results from the previous study conducted by Hartogh et al. (2005). This region appears to be "squeezing" the cooler mesospheric region into a smaller area. This is another anomaly that appears in almost all THOR results for τ_{lw} = 0.3.

Unfortunately, due to the warm anomalies centred over both poles at ~20 km altitude, the mid-troposphere displays substantially overestimated temperatures, pushing the expected temperatures for that region further up towards the mesosphere. Towards the equator, the tropospheric temperature difference between THOR and the results simulated by the GCM Martian COMMA-IAP (Hartogh et al., 2005) ranges from 20 K to 70 K, which is far more reasonable than at the poles, where the temperature difference can be >130 K. The thermal structure in the troposphere does not match TES observations shown in Figure 5.c as a result of these polar anomalies.

The zonal wind comparisons in Figure 6 show that THOR's easterlies are much too strong, reaching peak speeds of 280 $m \cdot s^{-1}$, and extend too far down into the troposphere compared to previous work.

These easterlies push the midlatitude westerlies further down towards the surface and further out towards the poles. The southern westerly wind strength is weakened while the northern westerly is strengthened considerably. While some of this may be related to the fact that the previous work was simulating the Martian atmosphere with a longwave optical depth of τ_{lw} = 0.18, this strange behaviour does seem linked to the temperature anomalies evident in THOR's zonal mean temperature.

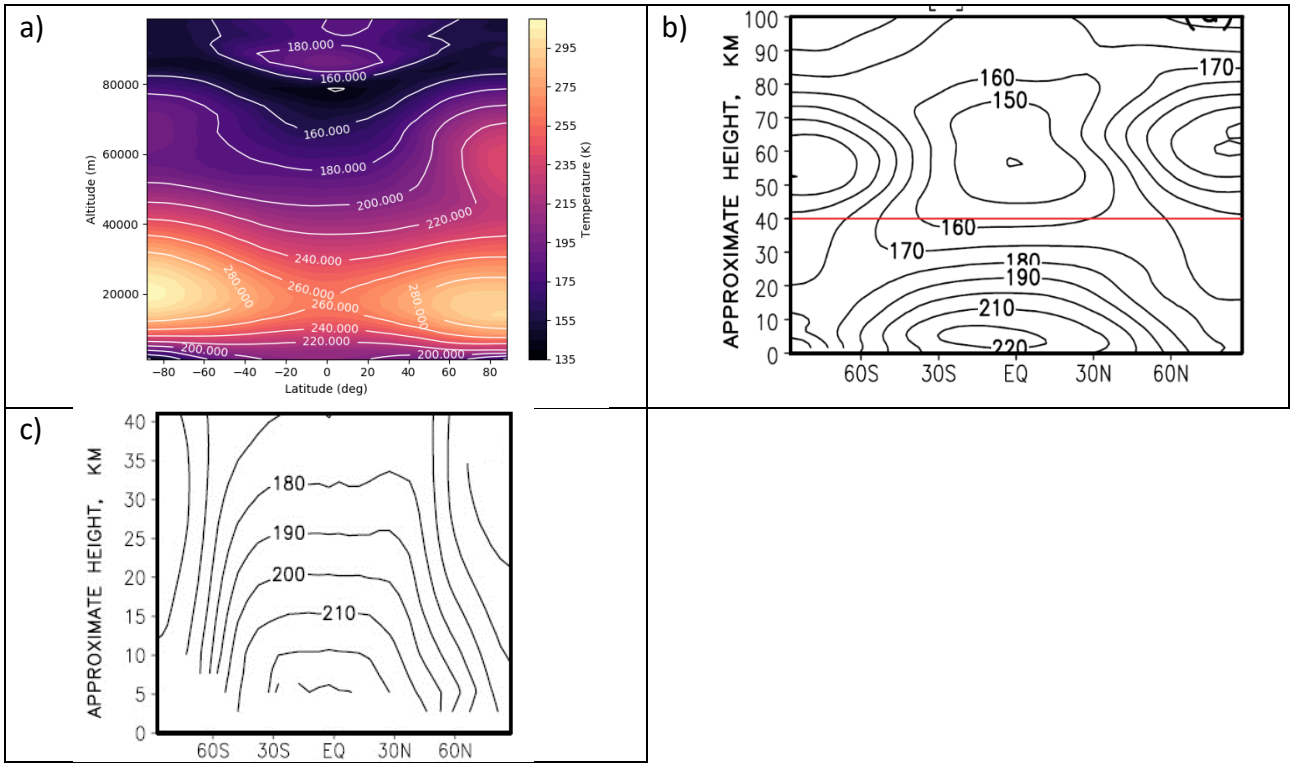

Figure 5: Vernal equinox (L_s = 180°) zonal mean temperature outputs a) for a 5-day average simulated by THOR for τ_{lw} = 0.3, b) simulated by Martian COMMA-IAP for τ_{lw} = 0.18 over an interval of $L_s \pm 3°$ with topography turned on (taken from Hartogh et al. (2005)), and c) as measured by TES (taken from Hartogh et al. (2005)).

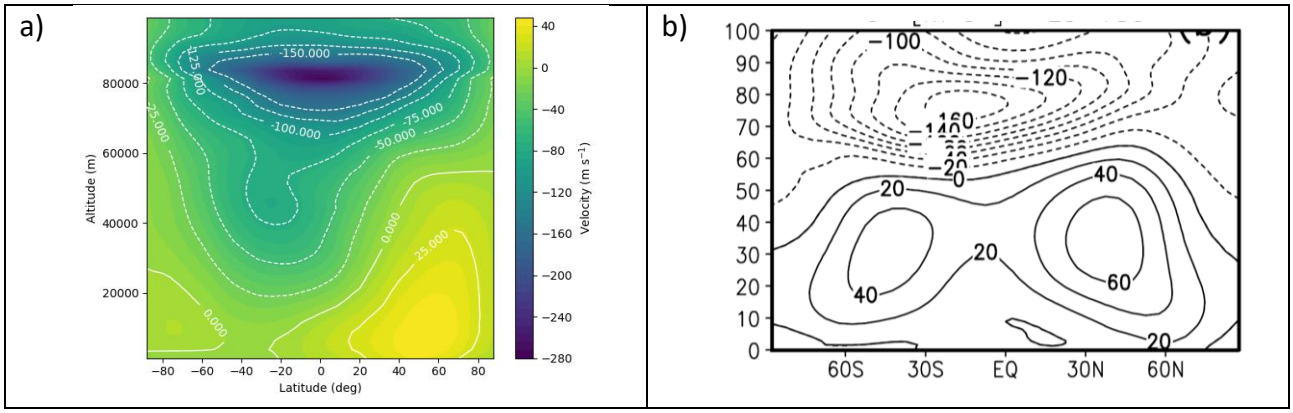

Figure 6: Vernal equinox (L_s = 180°) zonal wind outputs a) for a 5-day average simulated by THOR for τ_{lw} = 0.3, b) simulated by Martian COMMA-IAP for τ_{lw} = 0.18 over an interval of $L_s \pm 3°$ with topography turned on (taken from Hartogh et al. (2005)).

3.2.3. Southern winter (L_s = 90° – 120°)

As expected with a solstice, the thermal structure generated by THOR is heavily skewed to one hemisphere (in this case, the northern hemisphere). As with southern autumn in Section 3.2.2, THOR's thermal structure results seem to agree more favourably with the AOPP spectral model than the LMD grid point model, particularly with regard to the mesospheric polar warming in the southern hemisphere (Figure 7.a). The vertical extent of the southern tropospheric polar cooling is suppressed in THOR compared to both LMD and AOPP, likely as a result of the anomalous warming. If the anomalous temperature extremes are disregarded, THOR overestimates temperatures in warm regions by ~60-90 K but handles temperatures in cool regions reasonably well.

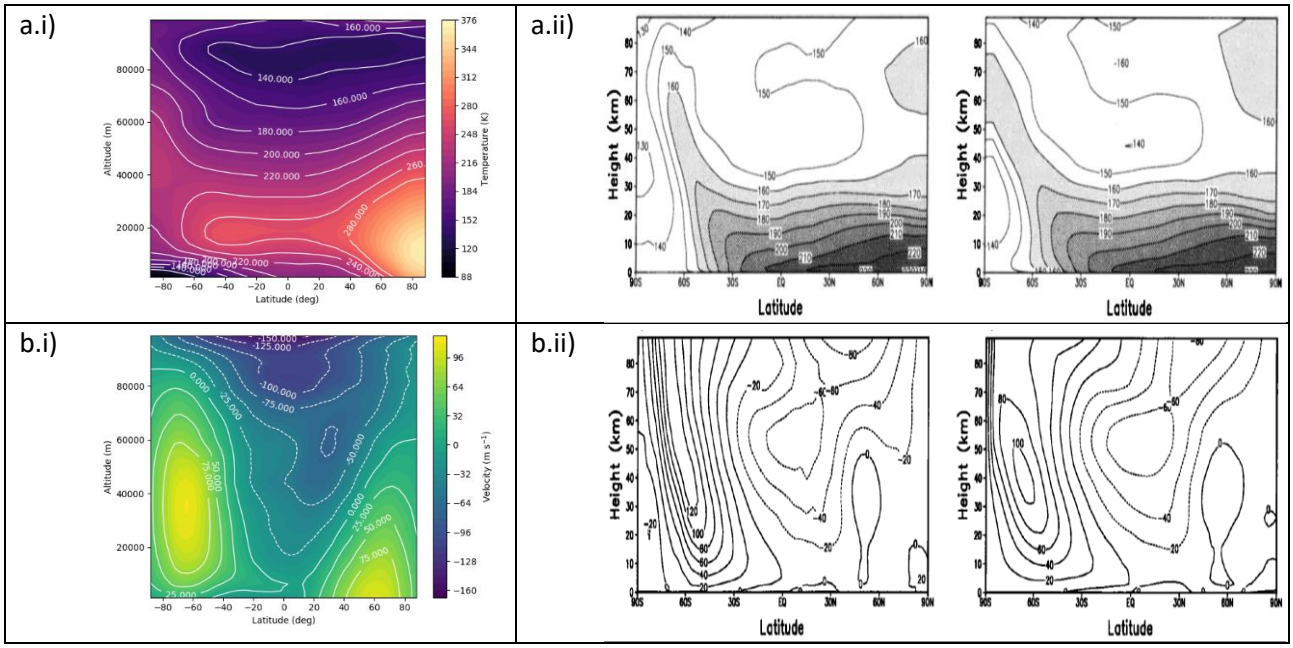

Figure 7: L_s = 90°-120°, seasonally averaged outputs for a) zonal mean temperature simulated by (i) THOR and (ii) LMD (left) and AOPP (right); b) zonal wind simulated by (i) THOR and (ii) LMD (left) and AOPP (right). All LMD and AOPP figures are taken from Forget et al. (1999) and are using a longwave optical depth of τ_{lw} = 0.4.

THOR's zonal winds tend to match the structure observed by both LMD and AOPP but, again, comparing more favourably to AOPP than to LMD (Figure 7.b). The southern westerly jet, in particular, is shown in THOR as a closed system, much like AOPP but at odds with LMD. It's maximum wind speed of ~130 m·s^{-1} is only slightly higher than LMD's 120 m·s^{-1} and AOPP's 100 m·s^{-1}. Similarly, THOR's easterlies are well-matched with those observed in the LMD and AOPP models, if somewhat overestimated. Linked to the bizarre warm anomaly observed in Figure 7.a.i) is an anomalously strong westerly in the low-level northern midlatitudes (centred over 60°N). Its peak intensity at the surface of ~96 m·s^{-1} is almost an order of magnitude greater than its LMD and AOPP counterparts (which peak at ~0 m·s^{-1} over the midlatitudes and ~20 m·s^{-1} over the poles respectively).

Figure 8 compares a 5-day average of zonal mean temperature around the southern winter solstice (L_s = 90°) as simulated by THOR with results from previous studies generated by the GM3 and Martian COMMA-IAP grid-point models, as well as measurements acquired by the Thermal Emission Spectrometer (TES) aboard the Mars Global Surveyor orbiter. Once again, ignoring the strange warm anomaly, THOR overestimates temperatures in the upper troposphere by up to ~80 K, ~70K, and ~100K compared to GM3 (Figure 8.b), COMMA-IAP (Figure 8.c and Figure 8.d), and TES observations (Figure 8.e) respectively. It also somewhat overestimates temperatures in parts of the lower mesosphere by up to ~40 K compared to both GM3 and COMMA-IAP, although temperatures within the central cooling feature in the mesosphere are well matched. The surface southern polar cooling in THOR is, again, stunted vertically compared to previous models but the temperatures here are also reasonably well matched. Surprisingly, though it's difficult to gauge from the contours in Figure 8.e, THOR's results in this particular region seem to match observations better than previous models. The structure of the mesospheric cooling feature is quite different compared to GM3 but is fairly similar to COMMA-IAP, despite COMMA-IAP modelling with a longwave optical depth of only τ = 0.18. An interesting point to note is the difference between COMMA-IAP's results with topography turned on (Figure 8.c) and topography turned off (Figure 8.d). In the latter simulation, the southern mesospheric polar warming is still present but ~40 K cooler than when topography is turned on. The mesospheric warming is practically symmetric, and the latitudinal and altitudinal extent of the northern lower-level tropospheric warming is greatly reduced. Compared to THOR's results in Figure 8.a, which also doesn't include topography it looks as though the entire thermal structure, particularly the tropospheric warming extending from the northern latitudes, has been shifted downward ~20 km in altitude. This produces an interesting effect: it looks like the entire plot has been flipped with respect to THOR, both latitudinally and thermally: where THOR has a warm anomaly between 0 km and 40 km altitude above the north pole, COMMA-IAP has a cold anomaly between 0 km and 40 km altitude over the south pole. Where THOR has cooler temperatures in the lowest 5 km between 90°S and 40°N, COMMA-IAP has warm temperatures in the lowest 5 km between 90°N and 40°S. Where THOR has cooler temperatures between 50 km and 90 km altitude, COMMA-IAP has warmer temperatures in that same region. Where THOR has a small region of warm temperatures in the highest 5 km between 0° and 90°N, COMMA-IAP has a small region of cool temperatures in the highest 10 km between 40°N and 90°S. While COMMA-IAP's results are generated using a slightly lower optical depth of τ_{lw} = 0.18 which may be affecting some of these trends, the most important aspect here appears to be topography, particularly as regards the

position and extent of the tropospheric warm region. THOR's Martian anomalies may be, in part, due to its exclusion of Martian topography.

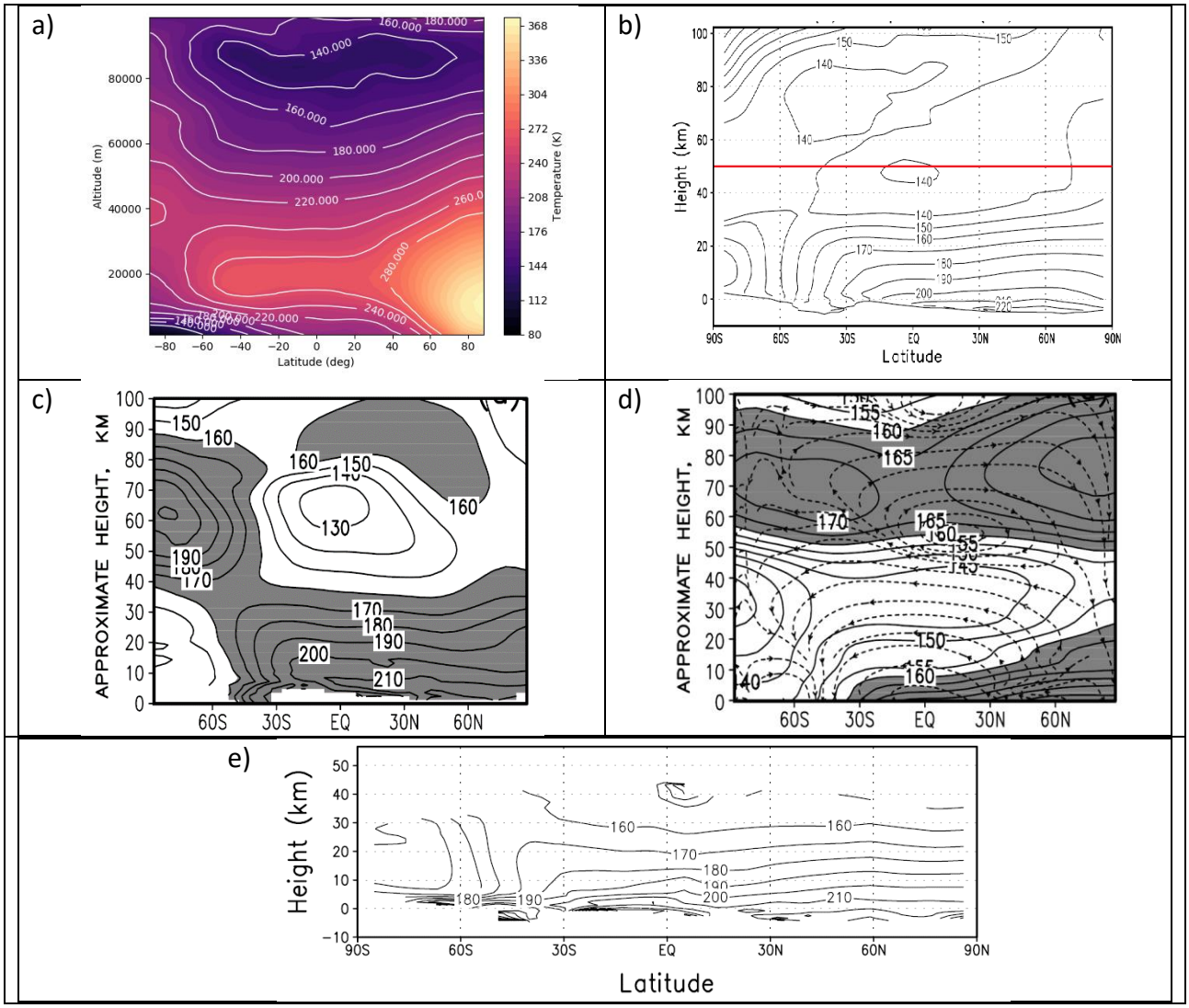

Figure 8: Winter solstice (L_s = 90°) zonal mean temperature outputs a) for a 5-day average simulated by THOR for τ_{lw} = 0.3, b) simulated by GM3 for τ_{lw} = 0.3 (taken from Moudden and McConnell (2005)), c) simulated by Martian COMMA-IAP for τ_{lw} = 0.18 over an interval of $L_s \pm 3°$ with topography turned on (taken from Hartogh et al. (2005)), d) as with (c) but with topography turned off (taken from Hartogh et al. (2005)), and e) as measured by TES (taken from Moudden and McConnell (2005)). The red line in plot (b) indicates the top altitude of plot (e). Shaded areas in plots (c) and (d) indicate temperatures above 160 K.

In terms of structure, THOR's zonal wind results (Figure 9.a) are closer to previous COMMA-IAP results for τ_{lw} = 0.18 with topography on (Figure 9.c) than previous GM3 results for τ_{lw} = 0.3 (Figure 9.b). While both the GM3 and COMMA-IAP results show a stronger southern westerly jet and weaker northern westerly wind field, the distribution and strength of the easterlies is more in line with COMMA-IAP (topography on) than GM3. This is very strange when one compares the GM3 results (which include topography) with the topography-off case for COMMA-IAP – both of these display similarly symmetric winds of comparable size and strength, although GM3's southern

westerly jet is closed, while the COMMA-IAP's extends beyond the mesosphere and into Mars's thermosphere (not shown). It is interesting that these THOR results, which were generated without the inclusion of topography, should be more closely matched with a previous case for a lower longwave optical depth which included topography than another previous case of the same exact longwave optical depth. This seems to suggest that a higher longwave optical depth can compensate for a lack of topography in generating zonal winds. Despite the mismatch in zonal winds between these THOR and GM3 results, the vertical velocities between these two models are very well matched, as seen in Figure 10, and demonstrate the Martian cross-equatorial Hadley cell common for Martian solstitial seasons.

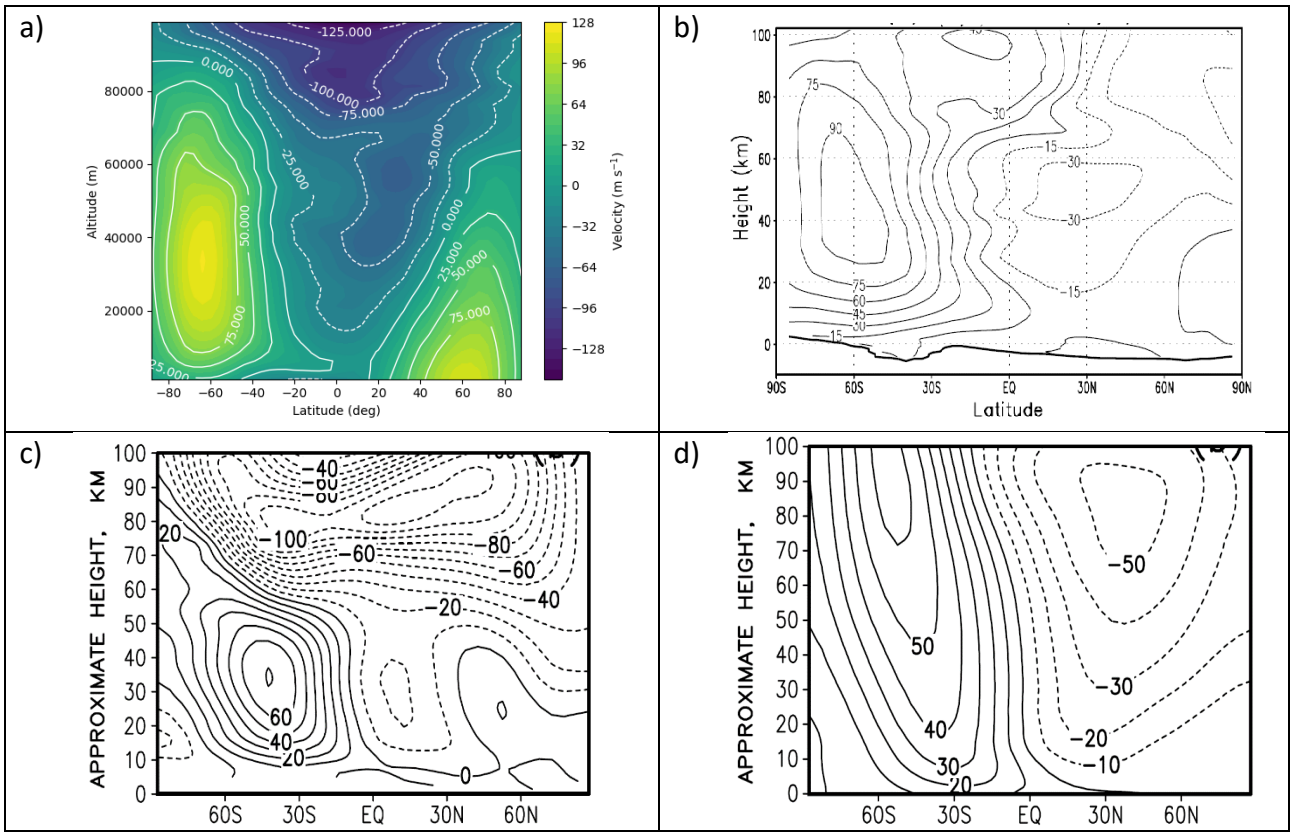

Figure 9: Winter solstice (L_s = 90°) zonal wind outputs a) for a 5-day average simulated by THOR for τ_{lw} = 0.3, b) simulated by GM3 for τ_{lw} = 0.3 (taken from Moudden and McConnell (2005)), c) simulated by Martian COMMA-IAP for τ_{lw} = 0.18 over an interval of $L_s \pm 3°$ with topography turned on (taken from Hartogh et al. (2005)), and d) as with (c) but with topography turned off (taken from Hartogh et al. (2005)).

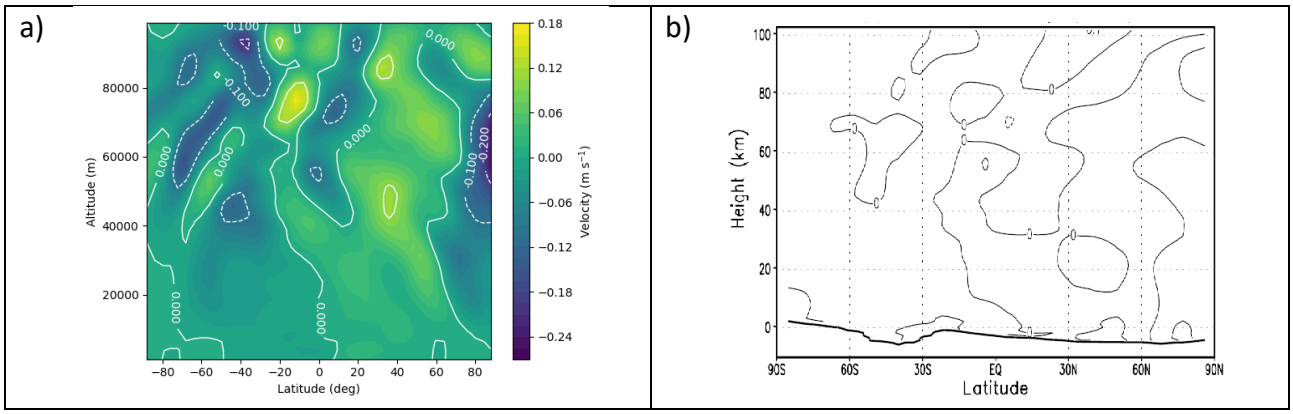

Figure 10: Winter solstice (L_s = 90°) vertical velocity outputs a) for a 5-day average simulated by THOR for τ_{lw} = 0.3, b) simulated by GM3 for τ_{lw} = 0.3 (taken from Moudden and McConnell (2005)).

3.2.4. Southern summer – the dusty season (L_s = 270 ° – 300 °)

The dustiest season on Mars is southern summer, the season when most large and/or global dust storms are generated, though this can be highly variable. In Figure 11, seasonally-averaged results for τ_{lw} = 0.3, τ_{lw} = 2, and τ_{lw} = 5 are compared with seasonally averaged results for τ = 1 previously generated by Forget et al. (1999) using the LMD model. What's most interesting to note here is that neither the τ_{lw} = 2 or τ_{lw} = 5 generate the same low-level polar anomalies in zonal mean temperature exhibited by any of the τ_{lw} = 0.3 results for this season or any other season. Warm temperature extremes in the τ_{lw} = 2 and τ_{lw} = 5 cases (Figure 11.a.ii and Figure 11.a.iii) are 128-144 K less than their τ_{lw} = 0.3 counterparts (Figure 11.a.i), and overestimates in temperature are only small (~10-20 K). The polar temperature inversion (in this case, over the north pole) between the troposphere and the mesosphere is much more readily apparent in the τ_{lw} = 2 and τ_{lw} = 5 cases, although the overall structure in the τ_{lw} = 0.3 case is better matched to the results generated by the LMD model (Figure 11.a.iv) – despite its southern polar temperature anomaly and overestimated tropospheric temperatures – solely due to its lack of upper mesospheric warming. The τ_{lw} = 2 case is a far better match to the LMD model results in terms of tropospheric structure and sensible temperature estimation. Since the LMD model used a longwave optical depth of τ = 1, the results generated by THOR for τ_{lw} = 0.3 and τ_{lw} = 2 seem like adequate matches.

In many respects, the above is also true for zonal winds. With the exception of the anomalously strong southern westerly in the τ_{lw} = 0.3 case (Figure 11.b.i), the overall structure of the zonal winds is well matched to the LMD results (Figure 11.b.iv). However, the respective strengths of westerly jets are better represented by the τ_{lw} = 2 case (Figure 11.b.ii), despite the southern westerly jet still being too high. In all of THOR's zonal wind cases shown in Figure 11, the position of this southern

westerly jet is too far south and extends too far into the troposphere, which appears to link it to the temperature anomaly observed over the south pole.

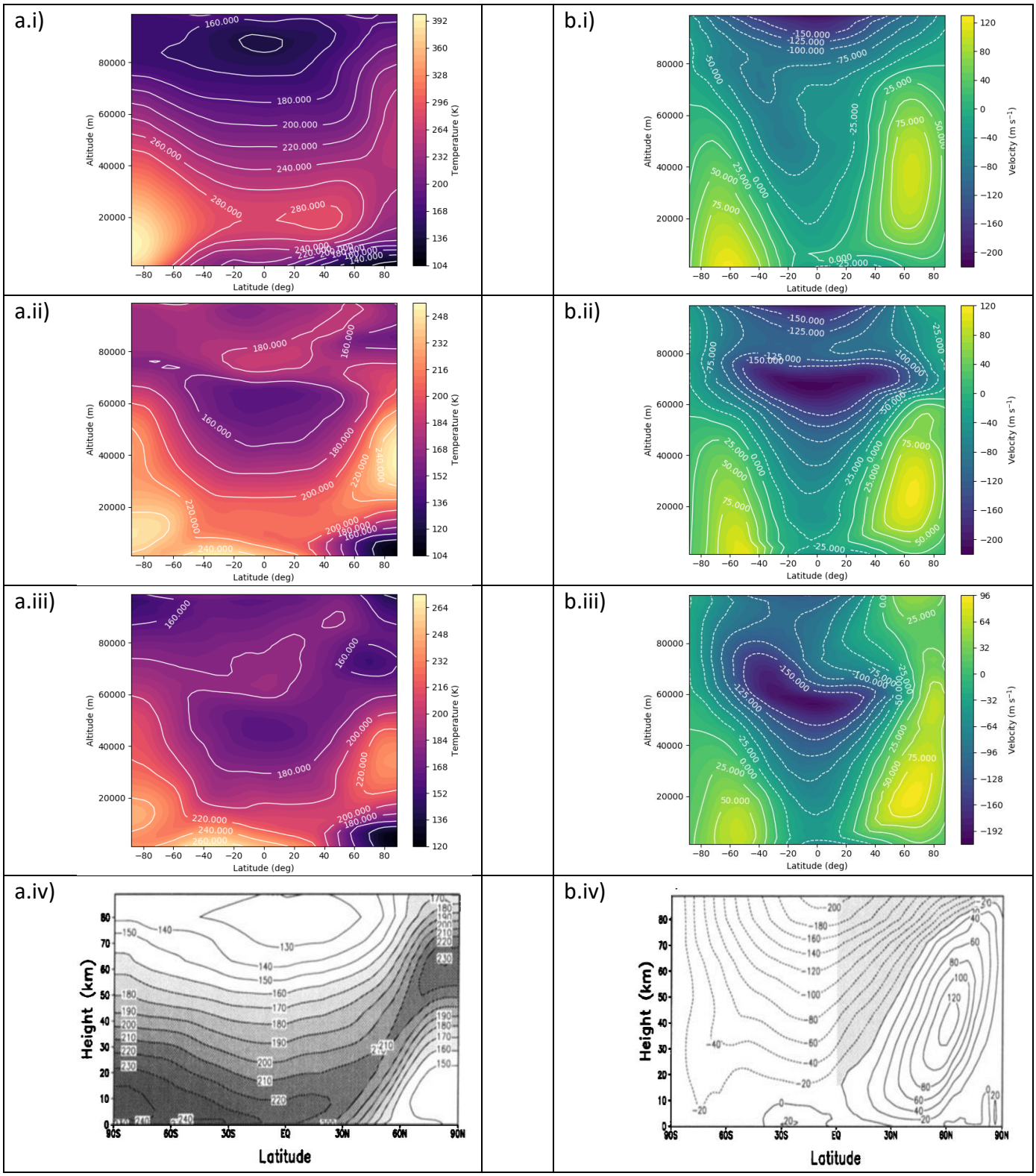

Figure 11: L_s = 270°-300°, seasonally averaged outputs for a) zonal mean temperature simulated by (i) THOR for τ_{lw} = 0.3, (ii) THOR for τ_{lw} = 2, (iii) THOR for τ_{lw} = 5, (iv) LMD for τ_{lw} = 1; b) zonal wind simulated by (i) THOR for τ_{lw} = 0.3, (ii) THOR for τ_{lw} = 2, (iii) THOR for τ_{lw} = 5, (iv) LMD for τ_{lw} = 1. Figures a.iv) and b.iv) are taken from Forget et al. (1999). The shaded area in figure b.iv) indicates the contribution of Coriolis and centrifugal forces to accelerating meridional poleward motion.

At southern summer solstice with low dust loading, THOR performs much as it did in the southern winter case ($L_s = 90°$). The overall temperature structure (see Figure 12.a) is somewhat warmer than in the winter case. This is to be expected, given that the southern summer solstice occurs close to perihelion while the southern winter solstice occurs close to aphelion, thus providing the summer solstice with stronger heating than the winter solstice (Moudden and McConnell, 2005). Despite its anomalies, the $\tau_{lw} = 0.3$ case compares favourably with previous work, as shown in Figure 12, displaying the requisite mesospheric polar warming over the north pole, warm temperatures throughout most of the troposphere and cool temperatures throughout most of the mesosphere. It also compares favourably with TES observations (shown here in Figure 12.e) in terms of structure, despite its overestimation of temperatures.

Zonal winds for $L_s = 270°$ (shown in Figure 13.a) do not exhibit quite the same problem outlined for the $L_s = 90°$ case. With the exception of the upper mesosphere, THOR's easterlies are well matched in speed and distribution to the GM3 model (Figure 13.b), while the strength of the northern westerly jet matches more closely with the COMMA-IAP model (Figure 13.c). And while the southern surface westerly is stronger in the GM3 model than in COMMA-IAP, in line with THOR's results, it's also nowhere near as strong as its THOR counterpart, nor is it located at the same latitude. COMMA-IAP's surface westerly jet, however, is located at the same latitude as its THOR counterpart but its strength (peak wind speed of ~20 $m \cdot s^{-1}$) is a fraction of that displayed in THOR's results (peak wind speed of >120 $m \cdot s^{-1}$). Once again, this southern westerly jet appears to be linked to the temperature anomaly exhibited in Figure 12.a, suggesting a link between optical depth and zonally-averaged temperatures and winds. With the exception of two very specific features of descending air in the upper mesospheric polar regions (denoted by negative values) and a pocket of weakly ascending air in the northern troposphere (denoted by positive values), THOR's vertical velocity distribution (shown in Figure 14.a) only weakly matches with GM3's distribution (Figure 14.b) but does clearly indicate the solstitial cross-equatorial Hadley cell. As expected, this cell is more latitudinally extensive than in the $L_s = 90°$ case.

For moderate dust loading (Figure 15.a), THOR performs remarkably well against previous results generated by Moudden and McConnell (2005) for $\tau = 3$ (Figure 15.c) and TES observations (Figure 15.d). Temperature values and structure are very well matched, although the upper mesospheric warming centred around the equator is pushed further down into the mesosphere in THOR than in

the GM3 model used by Moudden and McConnell (2005). When comparing THOR's moderate dust loading case against its high dust loading case (shown in Figure 15.b), it becomes apparent that higher dust loading causes this equatorial mesospheric cooling to be pushed further towards the surface, while surface temperatures in the southern midlatitudes become slightly hotter. This seems to indicate that higher dust loadings are able to trap more heat at the surface and prevents heating of the upper troposphere.

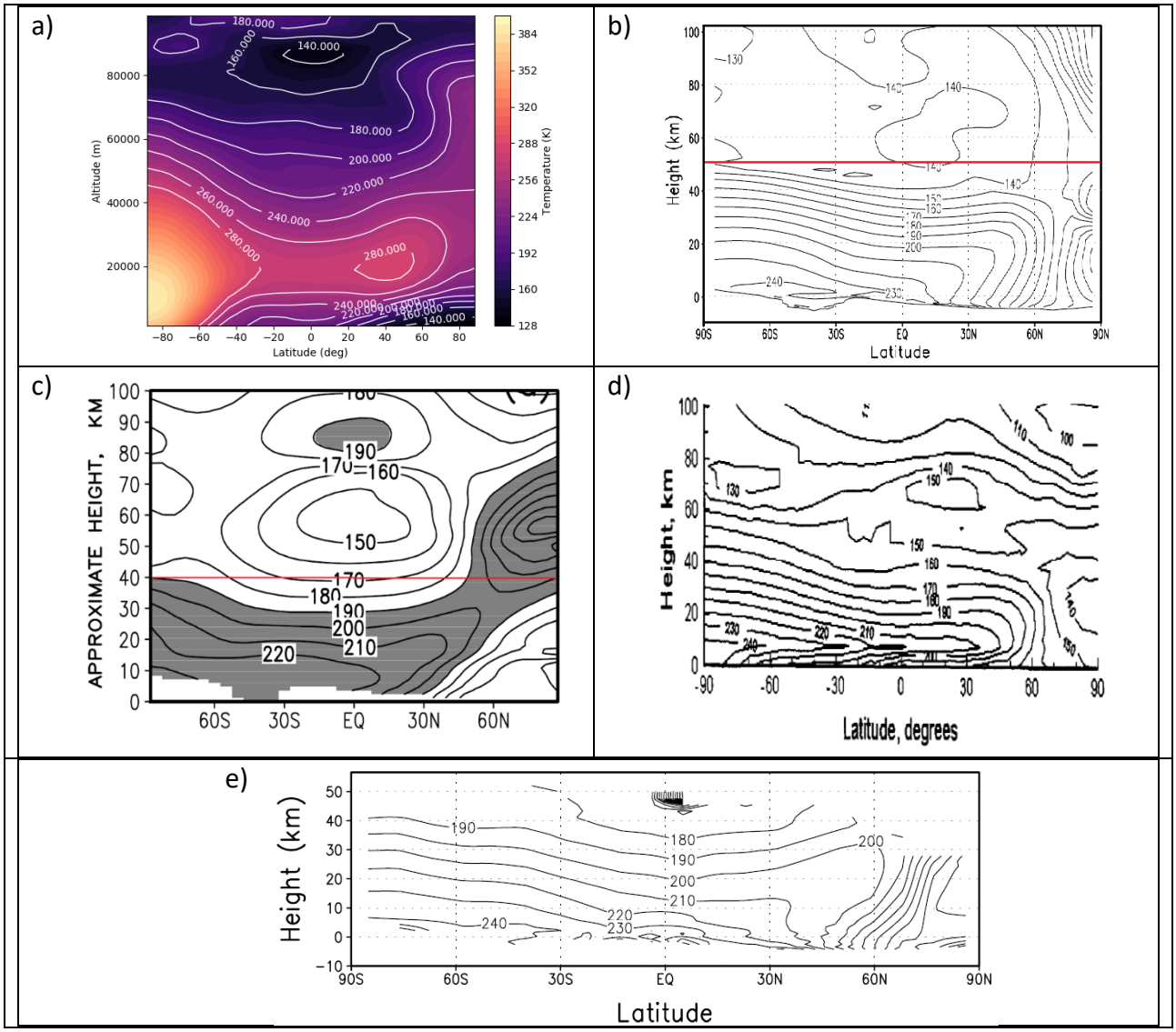

Figure 12: Summer solstice (L_s = 270°) zonal mean temperature outputs a) for a 5-day average simulated by THOR for τ_{lw} = 0.3, b) simulated by GM3 for τ_{lw} = 0.3 (taken from Moudden and McConnell (2005)), c) simulated by Martian COMMA-IAP for τ_{lw} = 0.18 over an interval of $L_s \pm 3°$ (taken from Hartogh et al. (2005)), d) simulated by Mars-GRAM 2000 for τ_{lw} = 0.3 at 3 am local time (taken from Justus et al. (2002)), and e) as measured by TES (taken from Moudden and McConnell (2005)).

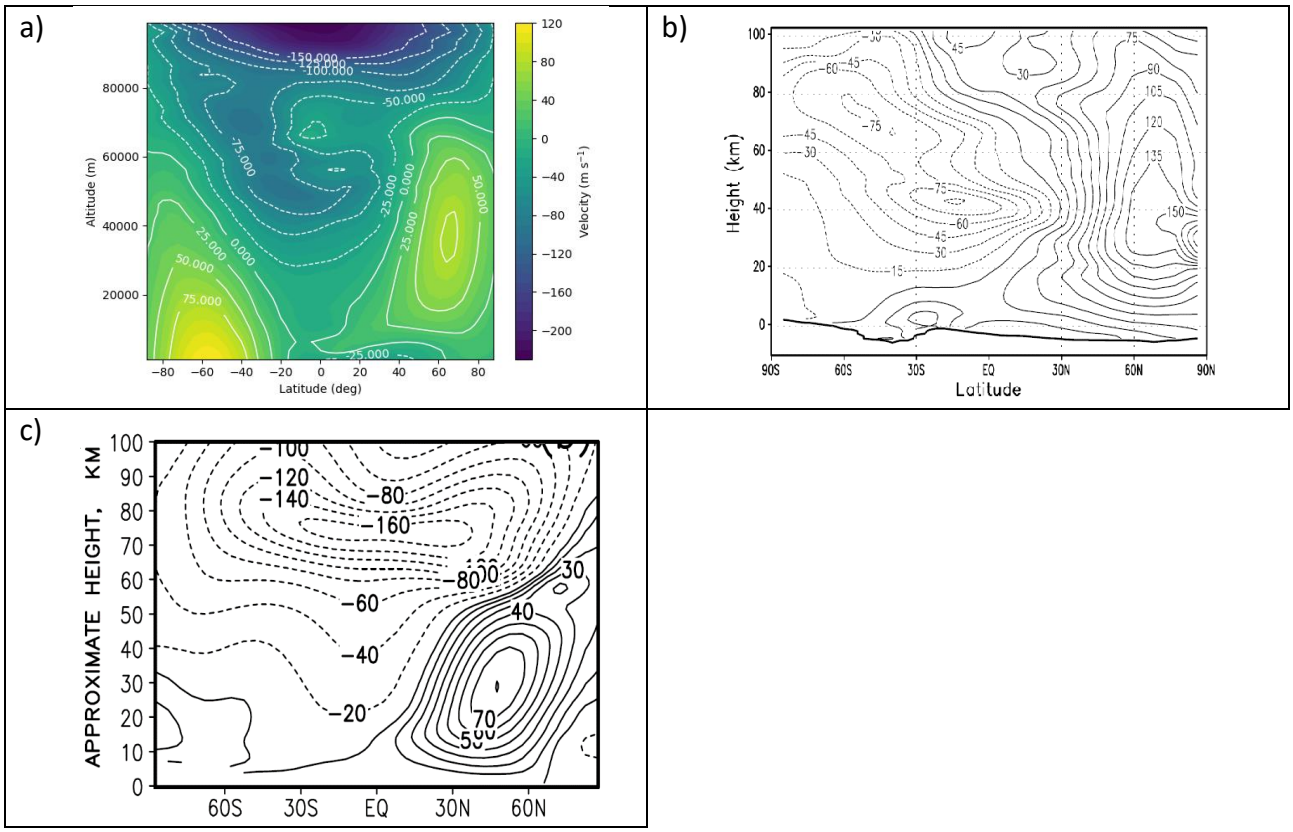

Figure 13: Summer solstice (L_s = 270°) zonal wind outputs a) for a 5-day average simulated by THOR for τ_{lw} = 0.3, b) simulated by GM3 for τ_{lw} = 0.3 (taken from Moudden and McConnell (2005)), and c) simulated by Martian COMMA-IAP for τ_{lw} = 0.18 over an interval of $L_s \pm 3°$ (taken from Hartogh et al. (2005)).

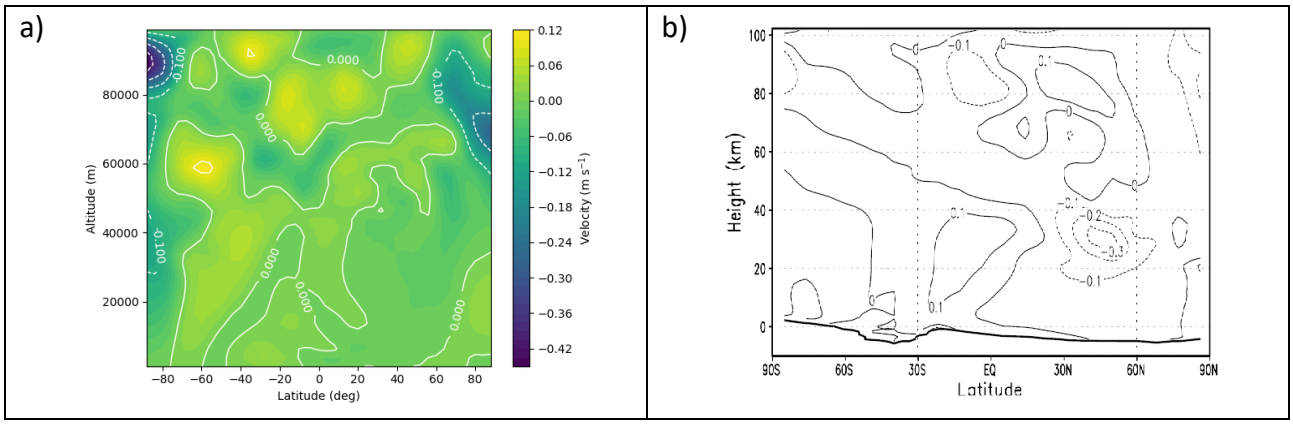

Figure 14: Summer solstice (L_s = 270°) vertical velocity outputs a) for a 5-day average simulated by THOR for τ_{lw} = 0.3, b) simulated by GM3 for τ_{lw} = 0.3 (taken from Moudden and McConnell (2005)).

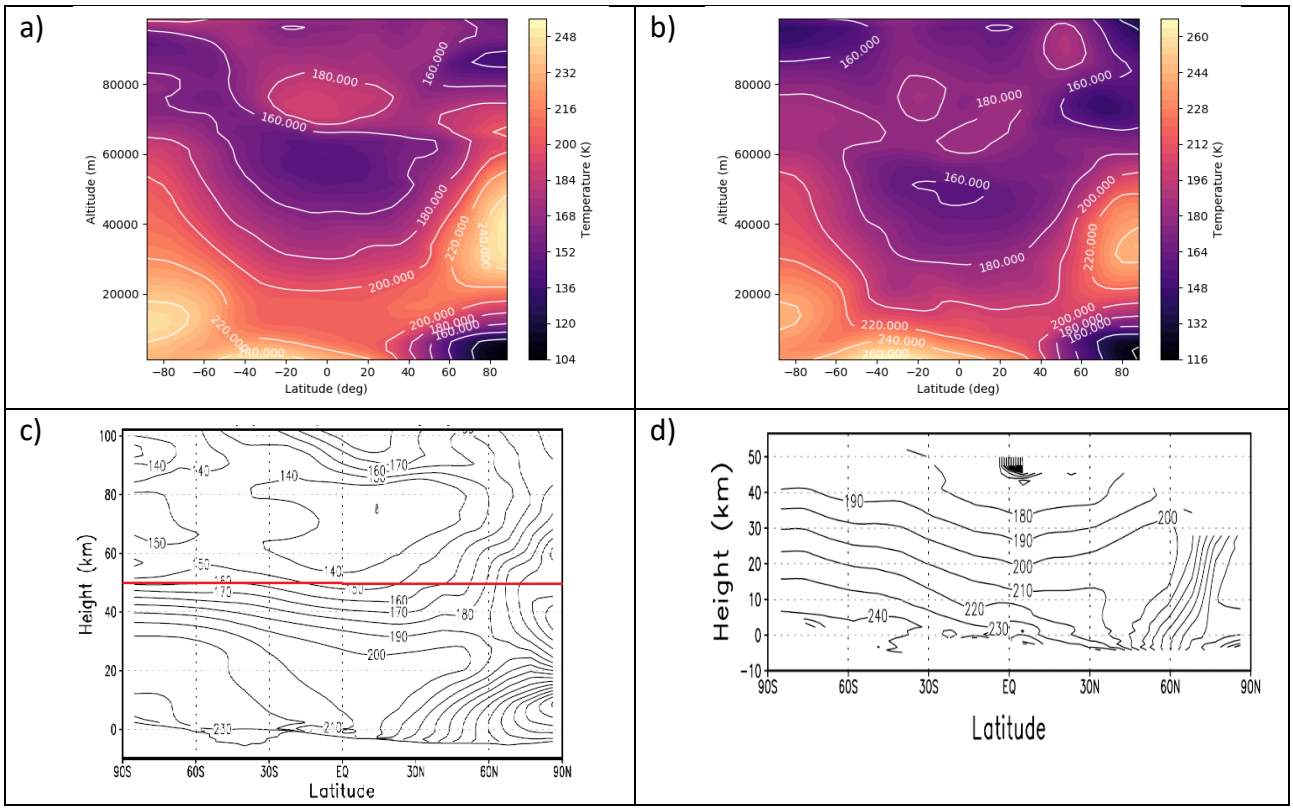

Figure 15: Summer solstice (L_s = 270°) zonal mean temperature outputs a) for a 5-day average simulated by THOR for τ_{lw} = 2, b) for a 5-day average simulated by THOR for τ_{lw} = 5, c) simulated by GM3 for τ_{lw} = 3, and d) as measured by TES. Figures (c) and (d) are taken from Moudden and McConnell (2005).

As with the τ_{lw} = 0.3 case for zonal winds, THOR again substantially overestimates the southern surface westerly wind speed when compared to results from GM3 for τ_{lw} = 3 (shown in Figure 16.c), especially for the τ_{lw} = 2 case (Figure 16.a). For the τ_{lw} = 5 case (Figure 16.b), this southern westerly, while vertically larger, is not much stronger than the one displayed in the GM3 results, though it is again displaced by ~30°S. For both τ_{lw} = 2 and τ_{lw} = 5, the strongest easterlies are displaced ~20 km lower in altitude than for the GM3 results while also overestimating their peak strength (for THOR, peak easterly wind strength is ~240 m·s^{-1} in both cases, while GM3's peak strength is ~195 m·s^{-1}). Despite THOR's overestimation of westerly wind strength, the τ_{lw} = 5 case does exhibit the same two peaks in northern westerlies between 20 km and 60 km altitude, though neither GM3 nor THOR's τ_{lw} = 2 case exhibit the northern westerly in the uppermost 10 km.

In vertical velocity results (Figure 17.a and Figure 17.b), both τ_{lw} = 2 and τ_{lw} = 5 exhibit the same strong pockets of descending air in the mid- to upper-levels between 60°N and 90°N. The distribution of ascending air is also similar. The northern easterly distribution exhibited in the GM3 results (Figure 17.c) bears more resemblance to the τ_{lw} = 2 case than the τ_{lw} = 5 case. However, a strong region of ascending air in GM3's southern midlatitudes is more evident in the τ_{lw} = 5 case

than in the τ_{lw} = 2 case. Regardless, the overall distribution in THOR's results still clearly show the ascending and descending arms of the latitudinally extensive, cross-equatorial Hadley cell one would expect to see in a Martian southern summer.

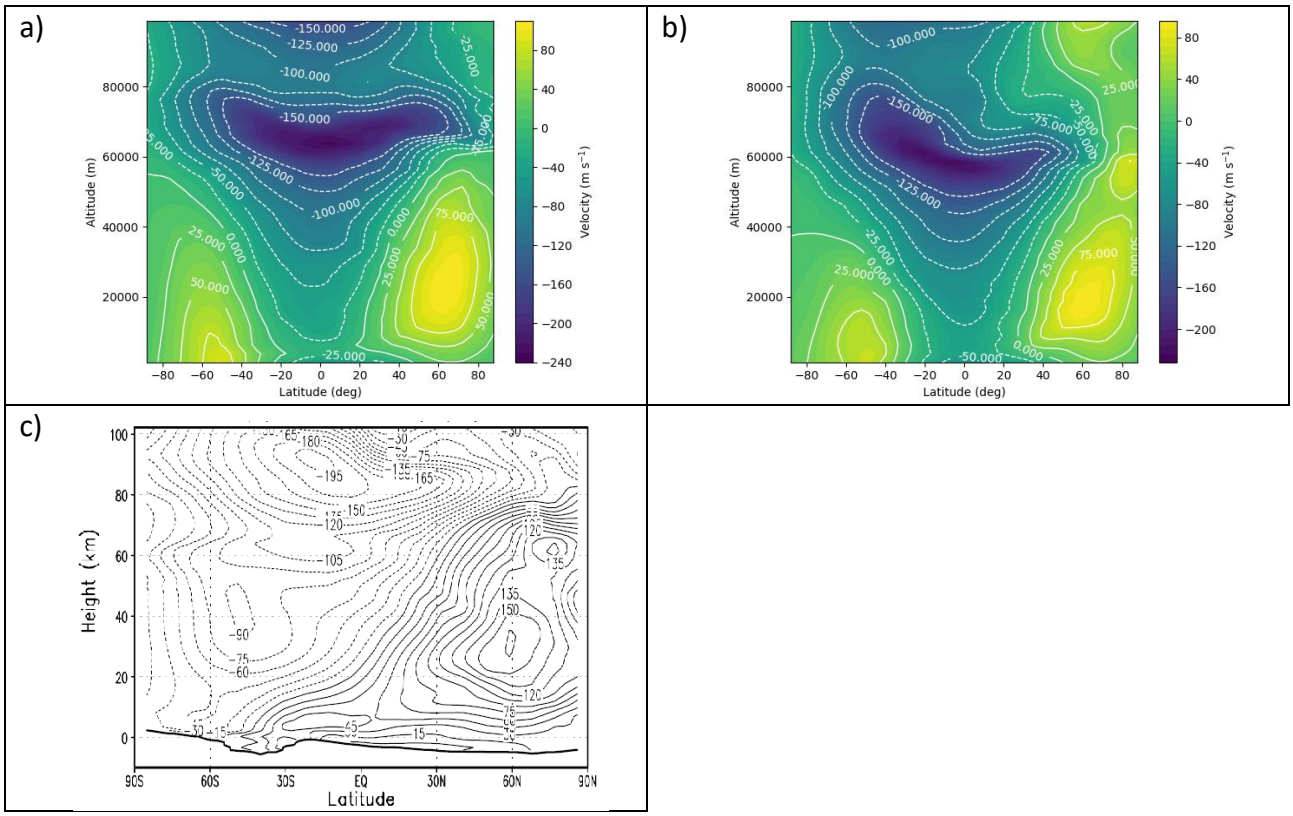

Figure 16: Summer solstice (L_s = 270°) zonal wind outputs a) for a 5-day average simulated by THOR for τ_{lw} = 2, b) for a 5 day average simulated by THOR for τ_{lw} = 5, c) simulated by GM3 for τ_{lw} = 3 (taken from Moudden and McConnell (2005)).

3.3. OBLIQUITY VARIATIONS

The implementation of optical depth in THOR is more advanced than previous models and may lead to some of the observed differences. To assess this, another set of simulations was run with τ_{lw} = 0.1 and $\tau_{lw,pole}$ = 0.08 and compared with the low-dust scenario for τ_{lw} = 0.3 and $\tau_{lw,pole}$ = 0.1 while varying obliquity to see if the problem persisted with minimal dust loading. The shortwave optical depth of τ_{sw} = 0.45 remained unchanged in order to maintain consistency. The results were compared with those obtained by Haberle et al. (2003b) for τ_{lw} = 0.3 to see if the problem could be identified.

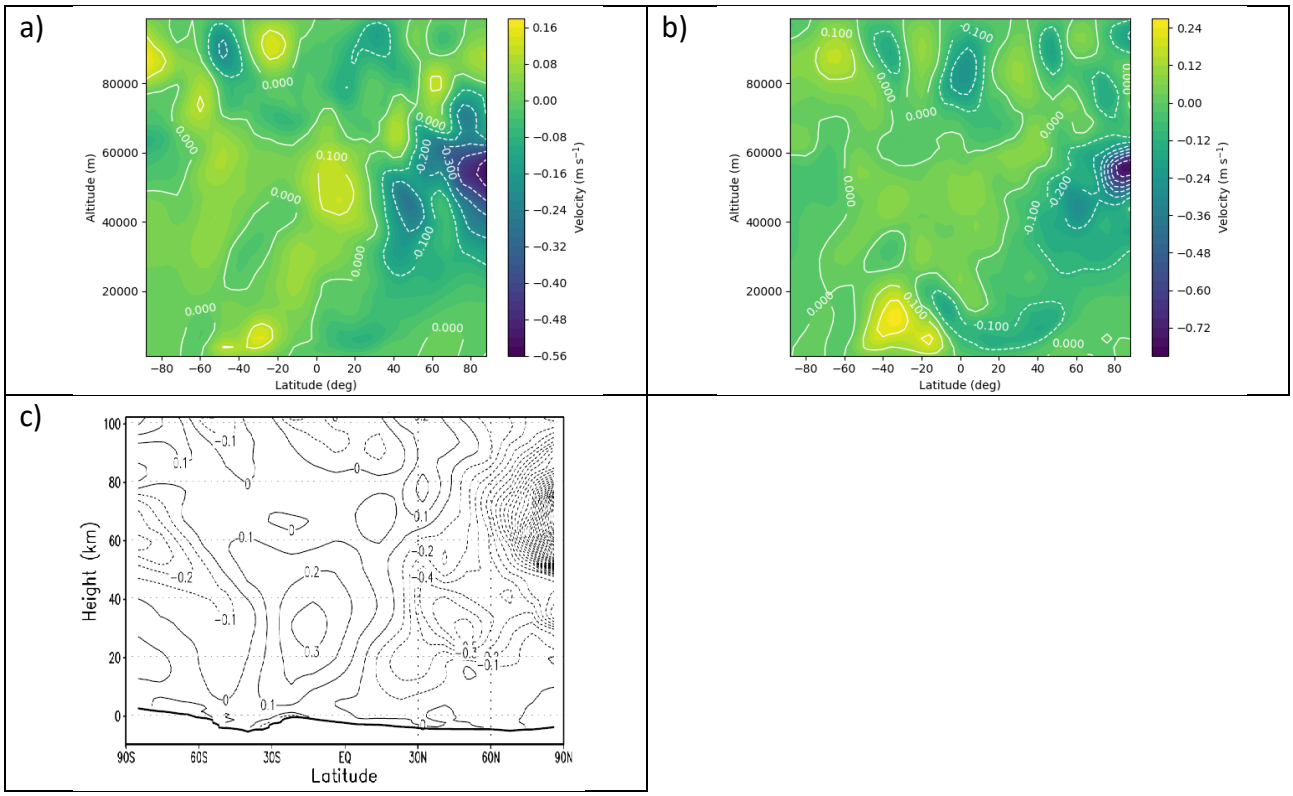

Figure 17: Summer solstice (L_s = 270°) vertical velocity outputs a) for a 5-day average simulated by THOR for τ_{lw} = 2, b) for a 5-day average simulated by THOR for τ_{lw} = 5, c) simulated by GM3 for τ_{lw} = 3 (taken from Moudden and McConnell (2005)).

3.3.1. Low obliquity (ε = 0°)

As can be seen in Figure 18 and Appendix 5 respectively, both the southern autumnal equinox (L_s = 0°) and southern summer solstice (L_s = 270°) display almost entirely symmetric results, which is expected for such a low obliquity. For each optical depth simulation, there is almost no difference between southern autumnal equinox and southern summer solstice, except that southern summer solstice is 20 K cooler with weaker easterlies and slightly stronger westerlies than southern autumnal equinox at all levels. This seems counterintuitive, given that the southern summer solstice is closer to perihelion than southern autumnal equinox is, though it does match with the results of previous work generated by (Haberle et al., 2003b) using the NASA/AMES GCM (as shown in Figure 18.a.iii and b.iii, and Appendix 5, Figure 1.a.iii and b.iii). Comparing low obliquity southern autumnal equinox results with those for present-day obliquity (shown in Appendix 6), the resemblance is favourable, and the low obliquity regime shows a greater amount of symmetry and weaker mesospheric polar warming, as expected. These comparisons show that the model's general dynamics are consistent and predictable. The more interesting comparison lies between the results of the τ_{lw} = 0.1 and τ_{lw} = 0.3 cases. Since results between L_s = 0° and L_s = 270° are almost identical, focus turns to the results displayed in Figure 18.

The difference in zonal mean temperature displayed by the two optical depth cases is stark, though it's worth remembering here that the τ_{lw} = 0.1 case has a polar optical depth value which is 80% of that for the rest of the planet (i.e. $\tau_{lw,pole}$ = 0.08) while the τ_{lw} = 0.3 case has a polar optical depth which is only a third of that for the rest of the planet (i.e. $\tau_{lw,\ pole}$ = 0.1). The two tropospheric polar anomalies one now expects to see in THOR's results for the τ_{lw} = 0.3 case (shown in Figure 18.a.ii.) have been completely obliterated in the τ_{lw} = 0.1 case (Figure 18.a.i.), replaced by a large swathe of high temperatures of up to 366 K across the entire middle troposphere, which certainly indicates a problem with optical depth. This temperature extreme is higher than for the τ_{lw} = 0.3 case, which peaks at 330 K. Neither case resembles the NASA/AMES results generated for τ = 0.3 by Haberle et al. (2003b) in the troposphere. Remarkably, the τ_{lw} = 0.1 case bears a much greater resemblance to NASA/AMES results in the equatorial mesosphere than the τ_{lw} = 0.3 case. In the former case, cooling in the equatorial region can clearly be seen while the latter case exhibits a warming in this region instead. Both cases exhibit the expected mesospheric polar warming, although this is more pronounced in the τ_{lw} = 0.3 case.

Both cases extend the easterlies too far down into the troposphere in the equatorial region compared to the NASA/AMES results (see Figure 18.b.i., b.ii., and b.iii). The τ_{lw} = 0.1 case, however, does a far better job of simulating the overall wind structure, particularly with regard to the two westerly jets. These are essentially non-existent in the τ_{lw} = 0.3 case, replaced by a single equatorial jet close to the surface, with a peak wind speed of 32 $m \cdot s^{-1}$. This jet does have a counterpart of similar strength in the NASA/AMES results, though it is not isolated from the northern westerly jet as THOR's appears to be.

The fact that neither of these cases is able to replicate the existing results in Haberle et al. (2003b) would seem to indicate that the problem lies in the shortwave optical depth value and not in the model itself. For the sake of thoroughness, and to complete all the aims originally set out in this paper, focus now turns to the high obliquity case of $\varepsilon = 60°$.

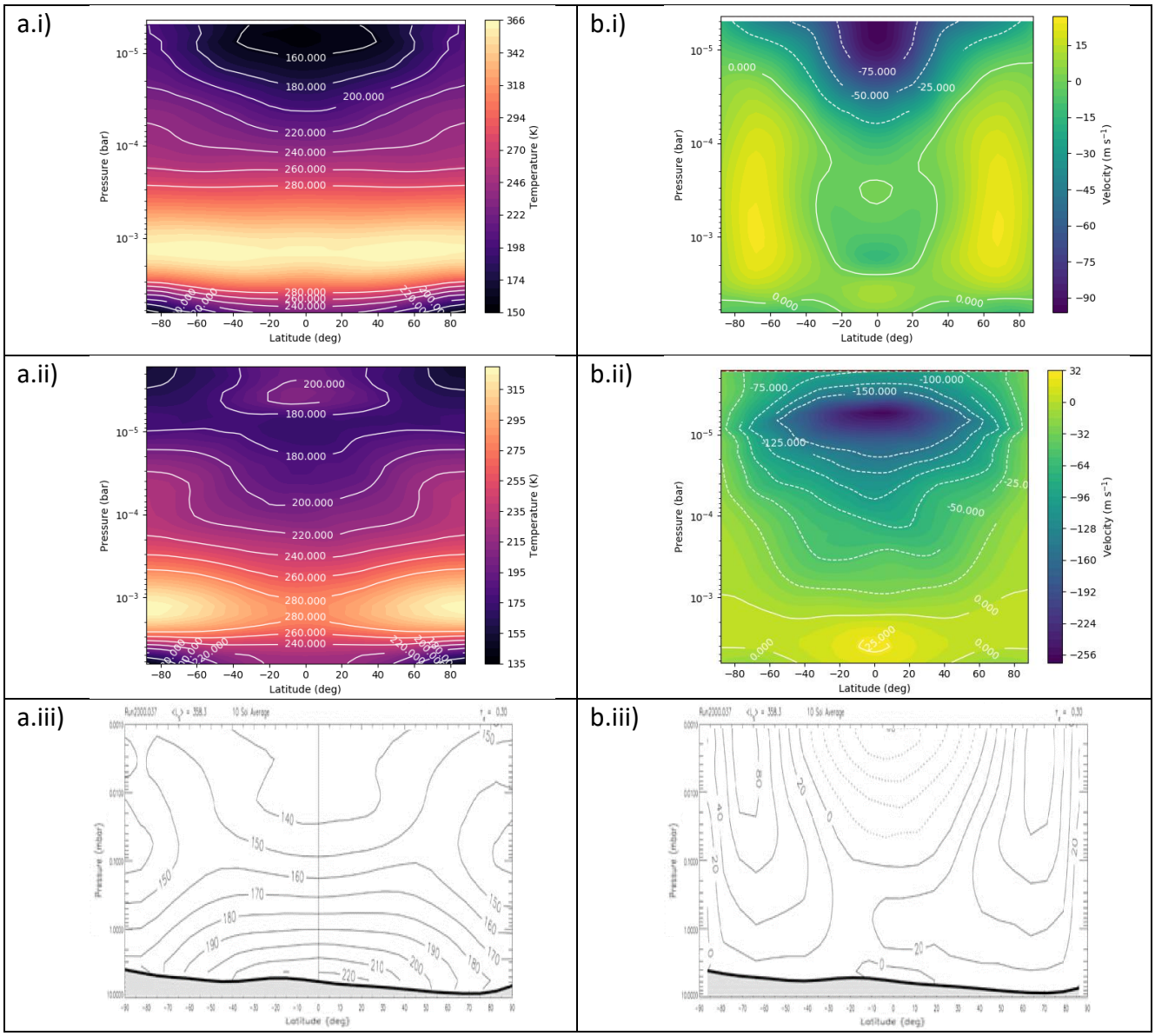

Figure 18: Low obliquity (ε = 0°) outputs at L_s = 0°. a) zonal mean temperature simulated by (i) THOR for τ_{lw} = 0.1, averaged over 5 days, (ii) THOR for τ_{lw} = 0.3, averaged over 5 days, (iii) NASA/AMES for τ_{lw} = 0.3, averaged over 10 sols; b) zonal wind simulated by (i) THOR for τ_{lw} = 0.1, averaged over 5 days, (ii) THOR for τ_{lw} = 0.3, averaged over 5 days, (iii) NASA/AMES for τ_{lw} = 0.3, averaged over 10 sols. Figures a.iv) and b.iv) are taken from Haberle et al. (2003b).

3.3.2. High obliquity (ε = 60°)

As expected, the results of the high obliquity case for southern autumnal equinox and southern summer solstice are not identical, again indicating the model's ability to model the basic atmospheric dynamics correctly. As shown in Figure 19, southern autumnal equinox displays a greater symmetry than southern summer solstice, shown in Figure 20. Compared to the current obliquity τ_{lw} = 0.3 case for southern autumnal equinox (shown in Appendix 6), the results shown in Figure 19.a.ii and b.ii bear a striking structural resemblance. An interesting point of note is that the tropospheric warm anomalies appear to have a smaller vertical extent in the higher obliquity case than in the present-day obliquity case, although a small surface cooling anomaly has now developed

at the south pole. Similarly, the high obliquity case models the two distinct westerly jets which were expected for the low and present-day cases, but which were either almost non-existent (in the former case) or much weaker than expected (in the latter case). Similar observations can be made regarding the southern summer solstice at high obliquity (shown in Figure 20) compared to the present-day obliquity results shown in Figure 12.a and Figure 13.a, although the small surface cooling anomaly shown at the south pole during southern autumnal equinox is now a small but highly extreme warm anomaly. This anomaly has temperatures of up to 10,000 K, causing the zonal mean temperature plots to appear almost black in all regions except for the region immediately above the southern polar surface (Figure 20.a.i and a.ii). A similar effect is seen with zonal wind for τ_{lw} = 0.3 in Figure 20.b.ii where there is a highly extreme easterly anomaly of up to 2160 $m \cdot s^{-1}$, resulting in most of the plot appearing yellow to green and only a tiny section just above the southern polar region appearing blue to black. Strangely, this effect is not seen at all with zonal wind for τ_{lw} = 0.1 (Figure 20.b.i).

In contrast to the results of the low obliquity regime, the high obliquity case for τ_{lw} = 0.1 at the southern autumnal equinox (Figure 19.a.i and b.i.) provides a better match with the NASA/AMES results obtained by Haberle et al. (2003b) (Figure 19.a.iii and b.iii.). The thermal structure displays a better resemblance, particularly at the 10^{-4} bar level and above, while the westerly jets are well matched with the NASA/AMES results in terms of both size and speed. The equatorial easterlies are also well matched between the mid-troposphere and mid-mesosphere, although the upper mesosphere is rather anomalous.

Results for the high obliquity case at southern summer solstice, however, do show that the τ_{lw} = 0.1 case (Figure 20.a.i and b.i) is a worse match for previous NASA/AMES results (Figure 20.a.iii and b.iii). The thermal structure, particularly in the mesosphere, is far better matched by the τ_{lw} = 0.3 case. The northern westerly jet is correctly shown as a closed system confined to the troposphere and mesosphere with similar wind speeds to the NASA/AMES results, whereas the τ_{lw} = 0.1 case shows this jet extending beyond the confines of the mesosphere and into the thermosphere, with much stronger peak winds. Both cases appear to underestimate the strength of the equatorial easterlies.

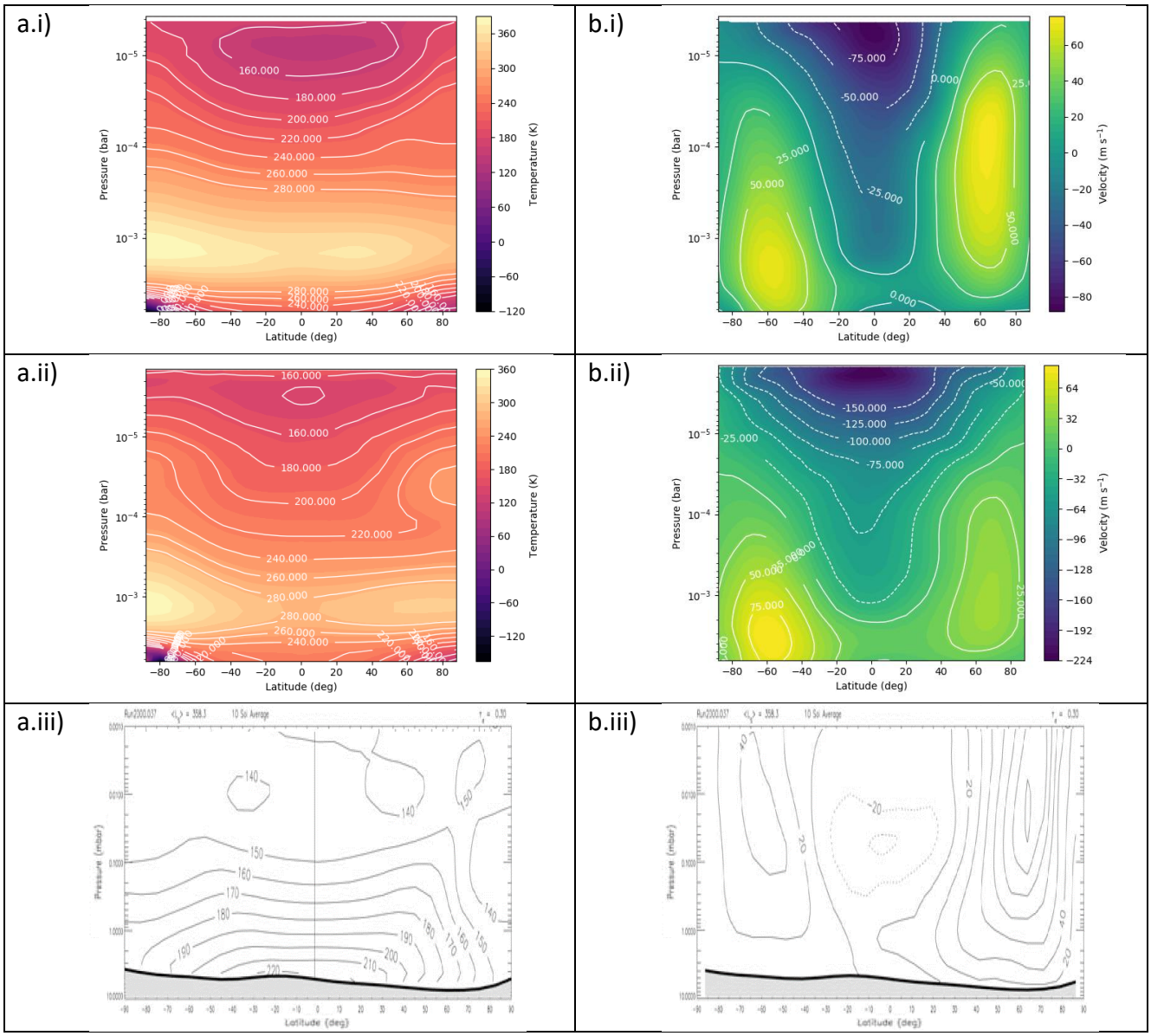

Figure 19: High obliquity (ε = 60°) outputs at L_s = 0°. a) zonal mean temperature simulated by (i) THOR for τ_{lw} = 0.1, averaged over 5 days, (ii) THOR for τ_{lw} = 0.3, averaged over 5 days, (iii) NASA/AMES for τ_{lw} = 0.3, averaged over 10 sols; b) zonal wind simulated by (i) THOR for τ_{lw} = 0.1, averaged over 5 days, (ii) THOR for τ_{lw} = 0.3, averaged over 5 days, (iii) NASA/AMES for τ_{lw} = 0.3, averaged over 10 sols. Figures a.iv) and b.iv) are taken from Haberle et al. (2003b).

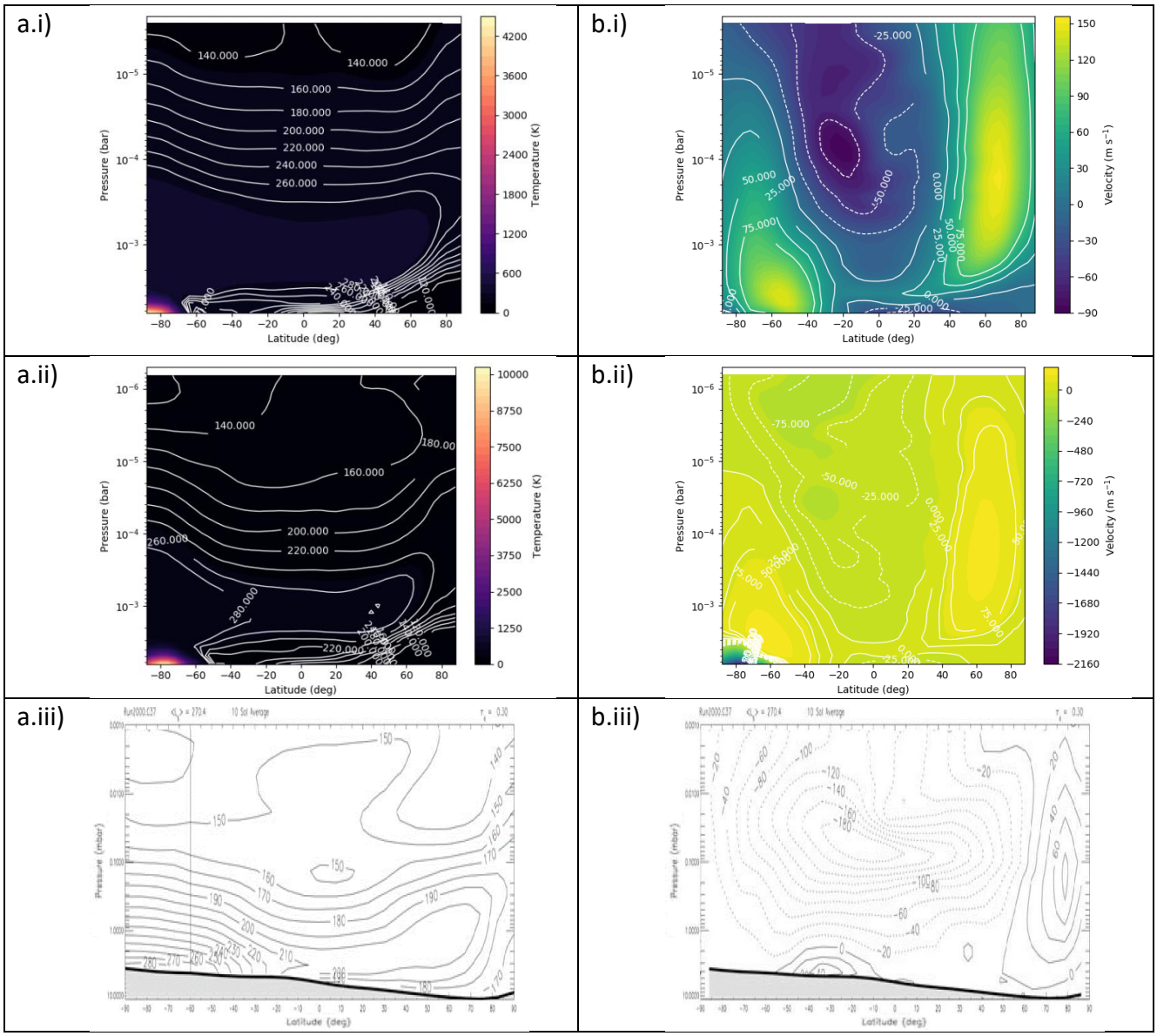

Figure 20: High obliquity (ε = 60°) outputs at L_s = 270°. a) zonal mean temperature simulated by (i) THOR for τ_{lw} = 0.1, averaged over 5 days, (ii) THOR for τ_{lw} = 0.3, averaged over 5 days, (iii) NASA/AMES for τ_{lw} = 0.3, averaged over 10 sols; b) zonal wind simulated by (i) THOR for τ_{lw} = 0.1, averaged over 5 days, (ii) THOR for τ_{lw} = 0.3, averaged over 5 days, (iii) NASA/AMES for τ_{lw} = 0.3, averaged over 10 sols. Figures a.iv) and b.iv) are taken from Haberle et al. (2003b).

CHAPTER 4 – CONCLUSIONS AND FUTURE WORK

The results presented in Chapter 3 show that THOR is capable of simulating Mars's basic seasonal atmospheric patterns at low, high, and present-day obliquity. The distinction between symmetric equinoctial seasons and asymmetric solstitial seasons is clearly modelled by THOR. However, without further investigation into aspects such as meridional winds, mass stream function, and potential vorticity, the current interpretation of these results, especially those relating to winds, is tentative. Upper-level flow particularly requires further study to check meridional flow against zonal and vertical winds. The vertical velocity trends which suggest a solstitial cross-equatorial Hadley cell are fairly weak but could be confirmed through meridional flow investigations. The apparent lowering of the top of the mesosphere in all results could be the result of several factors. Two, which may be inter-related, are the value given to the top of the model domain – here, set to 100 km altitude – and the strength of the sponge layer. While, for example, Forget et al. (1999) have also set the top of their model domain to 100 km, their seasonally averaged results – presented in Figures 3, 4, 7, and 11 – are trimmed to show only the bottom 90 km. Similarly, while Hartogh et al. (2005) set the top of their model domain to 130 km, their results were cropped to show only the bottom 110 km (further cropped here to the bottom 100 km to aid easier comparison with THOR results). Such cropping is done because the uppermost portion of the model domain is still contaminated by spurious waves, despite the application of upper boundary layer schemes (Hartogh et al., 2005). THOR's results have not been cropped to remove this contaminated upper portion. Such spurious waves can be observed in the top 10 km of almost all of THOR's results and may be contributing to the observed "shortening" of mesospheric features. Extending the model top to an altitude of 140-180 km, as in the work of Moudden and McConnell (2005), would allow a full extension of the Martian Hadley cell and thereby allow the mesospheric features to be more accurately modelled.

Another potential contributor to this "mesospheric shortening" is the lack of topography, which cannot currently be included in THOR. As noted in Chapter 1, Section 1.3.1, Mars's hemispherically asymmetric topography is a major contributor to zonal and meridional flows, dust mass transfer and temperature distributions. One suspects that including a Martian topography field in THOR would at least partially cut off the high temperature anomalies and associated strong westerlies observed at lower levels above the poles while helping to raise the mesospheric features to higher altitudes, thus increasing the accuracy of results. If this is not included, a lower boundary layer scheme representing flat surface friction could also improve results. Trial simulations were conducted with

THOR's boundary layer scheme enabled but these failed with numerical issues. Investigating these failures was beyond the time and scope of this project but must be addressed in future.

Potential sources of the observed low-level temperature anomalies and associated westerlies are the values set for longwave and shortwave optical depths. According to Read et al. (2015), many previous works have assumed a shortwave optical depth of $\tau_{sw} = 0$. The comparative works cited here do not specify their value for τ_{sw}; it's possible that they, too, have opted for a shortwave optical depth at or close to zero. In this work τ_{sw} was given a value of 0.45, as per Eq. 17. Since the results generated by THOR for $\tau_{lw} = 2$ and $\tau_{lw} = 5$ do not exhibit the temperature anomalies evident in the $\tau_{lw} = 0.3$ and $\tau_{lw} = 0.1$ cases, it seems likely that the anomalies exhibited in the latter cases are the result of τ_{sw} being greater than τ_{lw} and therefore dominating radiative transfer. Perhaps τ_{sw} has been calculated too highly, but this should be further investigated by changing the value of τ_{sw} in dusty scenarios. Alternatively, a variable τ_{sw} could be used, calculated using a variable cosine zenith angle, though this would require the addition of a complex Mars time-keeping code (see Schmidt (2019) for further details). At any rate, since τ_{sw} should not vary too much for any given planet, it seems that THOR is highly sensitive to changes in dust loading. This is especially the case for high obliquities (as seen in Figures 19 and 20 of Chapter 3), which could adversely affect the study of dusty planets and the Martian paleoclimate at high obliquity. It is thus imperative to be able to adequately simulate the radiative effects of dust. However, while THOR is based on first principles, it does not currently have a dedicated dust scheme; any consideration of Martian dust is included either as mean optical depth over the entire planet or within THOR's crude cloud parameterisation module. The latter option is particularly problematic, as the assumption of constant night-side opacity is only applicable to tidally-locked planets like WASP-43b (Mendonça et al., 2018a). For planets closer to home, like Mars, an entirely different scheme will be required. What form that might take is an open question. Given the number of Martian parameters which require tuning (most importantly, opacity and contact parameter), the model may no longer be self-consistent if a dedicated dust scheme is included. Devising an appropriate scheme for THOR will require thorough investigation.

Dust also affects albedo, both of which vary with latitude. Kahre et al. (2013) notes changes to Martian atmospheric stability with varying obliquity, increased dust loading (denoted by optical depth) and changes to polar albedo. THOR currently lacks the ability to distinguish polar albedo from the planet's bond albedo. The ability to change both optical depth *and* polar albedo may increase

the accuracy of results substantially. Furthermore, albedo is linked to the thermal conductivity of the surface. Mischna et al. (2013) notes that Mars's current albedo is largely determined "by the local, relatively bright, dust cover fraction over a much darker (largely basaltic) surface." Regions with minimal dust cover can result in albedos below 0.15, while regions with substantially more dust cover can reach albedos of 0.25-0.35. This has implications for the surface heat capacity – C_1 = 1.8 x 10^5 $J \cdot K^{-1} \cdot m^{-2}$ – used to generate the bulk of THOR's results. This value is likely too high to adequately simulate Mars's near-surface atmosphere, thus contributing to the extreme temperature anomalies exhibited at lower dust loadings. Running simulations with a lower surface heat capacity and including a classification map of surface material such as that published by Jones et al. (2014) may ameliorate this. Furthermore, there is no consideration of material grain size in this work. This should be included in future work, as grain size affects not only albedo but also thermal inertia and particle lifting, transport, and deposition processes (Jones et al., 2014, Read et al., 2015).

Finally, the "dust loading" effect observed here is based solely on optical depth. There is no consideration of atmospheric chemistry and the associated absorption spectra of particles. The observed temperature anomalies may thus be the result of a simple insolation blocking effect and the absorption of surface heat. Unlike other models (e.g. LMD, AOPP, NASA Ames, COMMA-IAP), THOR cannot currently separate the radiative effects of different absorbers. The contributions of CO_2 and H_2O have been effectively ignored, which could contribute to some of the observed dissimilarities between THOR and previous published works. A potential remedy would be to link THOR to some of the other Exoclime platforms like HELIOS-K (an ultrafast opacity calculator for exoplanetary atmospheres) and FastChem (an ultrafast equilibrium chemistry module, which has already been used in studies of WASP-43b (Mendonça et al., 2018b)). It would be interesting to see if either of these could be incorporated into studies of Mars's atmosphere. Alternatively, as noted by Kahre et al. (2013), the NASA Ames MGCM includes a radiative transfer scheme which accounts for suspended dust and gaseous CO_2 at both solar and infrared wavelengths. The inclusion of such a scheme would be immensely helpful, although it may affect THOR's internal consistency.

In all, considering that THOR has so far only really been tested on hot Jupiter-type planets, the results generated here for Mars are promising. There is room for improvement for terrestrial planet studies. High sensitivity to radiative transfer inputs related to optical depth, albedo, and surface heating will need to be kept in mind when using THOR for any future Martian climate studies.

References

ADCROFT, A., CAMPIN, J.-M., DODDRIDGE, E., DUTKIEWICZ, S., EVANGELINOS, C., FERREIRA, D., FOLLOWS, M., FORGET, G., FOX-KEMPER, B., HEIMBACH, P., HILL, C., HILL, E., HILL, H., JAHN, O., KLYMAK, J., LOSCH, M., MARSHALL, J., MAZE, G., MAZLOFF, M., MENEMENLIS, D., MOLOD, A. & SCOTT, J. 2018. *MITgcm documentation* [Online]. Available: https://media.readthedocs.org/pdf/mitgcm/latest/mitgcm.pdf [Accessed 14 June 2018].

ADCROFT, A., CAMPIN, J.-M., HILL, C. & MARSHALL, J. 2004a. Implementation of an atmosphere–ocean general circulation model on the expanded spherical cube. *Monthly Weather Review,* 132**,** 2845-2863.

ADCROFT, A., HILL, C., CAMPIN, J.-M., MARSHALL, J. & HEIMBACH, P. Overview of the formulation and numerics of the MIT GCM. Proceedings of the ECMWF seminar series on Numerical Methods, Recent developments in numerical methods for atmosphere and ocean modelling, 2004b. 139-149.

APPELBAUM, J. & FLOOD, D. J. 1990. Solar radiation on Mars. *Solar Energy,* 45**,** 353-363.

APRUZESE, J. 1980. The diffusivity factor re-examined. *Journal of Quantitative Spectroscopy and Radiative Transfer,* 24**,** 461-470.

BARNES, J. R. & HABERLE, R. M. 1996. The Martian Zonal-Mean Circulation: Angular Momentum and Potential Vorticity Structure in GCM Simulations. *Journal of the Atmospheric Sciences,* 53**,** 3143-3156.

CLIFFORD, S. M. 1993. A model for the hydrologic and climatic behavior of water on Mars. *Journal of Geophysical Research: Planets,* 98**,** 10973-11016.

COOK, K. H., VIZY, E. K. & SUN, X. 2017. Multidecadal-scale adjustment of the ocean mixed layer heat budget in the tropics: examining ocean reanalyses. *Climate Dynamics,* 50**,** 1513-1532.

CRONIN, T. W. 2014. On the choice of average solar zenith angle. *Journal of the Atmospheric Sciences,* 71**,** 2994-3003.

DAVIES, J. H. & DAVIES, D. R. 2010. Earth's surface heat flux. *Solid Earth,* 1**,** 5-24.

ESO. 2018. *THE EUROPEAN EXTREMELY LARGE TELESCOPE ("ELT") PROJECT* [Online]. European Southern Observatory (ESO). Available: https://www.eso.org/sci/facilities/eelt/ [Accessed 19 April 2018].

FORGET, F., HOURDIN, F., FOURNIER, R., HOURDIN, C., TALAGRAND, O., COLLINS, M., LEWIS, S. R., READ, P. L. & HUOT, J. P. 1999. Improved general circulation models of the Martian atmosphere from the surface to above 80 km. *Journal of Geophysical Research: Planets,* 104**,** 24155-24175.

FORGET, F., HOURDIN, F. & TALAGRAND, O. 1998. CO2 Snowfall on Mars: Simulation with a General Circulation Model. *Icarus,* 131**,** 302-316.

GIERASCH, P. & GOODY, R. 1967. An approximate calculation of radiative heating and radiative equilibrium in the Martian atmosphere. *Planetary and Space Science,* 15**,** 1465-1477.

GÓMEZ-LEAL, I., CODRON, F. & SELSIS, F. 2016. Thermal light curves of Earth-like planets: 1. Varying surface and rotation on planets in a terrestrial orbit. *Icarus,* 269**,** 98-110.

HABERLE, R. M., HOLLINGSWORTH, J. L., COLAPRETE, A., BRIDGER, A. F. C., MCKAY, C. P., MURPHY, J. R., SCHAEFFER, J., FREEDMAN, R. & FONDA, M. 2003a. The NASA/Ames Mars General Circulation Model: Model Improvements and Comparison with Observations. *Mars Atmosphere Modeling and Observations Workshop.* Granada, Spain.

HABERLE, R. M., MURPHY, J. R. & SCHAEFFER, J. 2003b. Orbital change experiments with a Mars general circulation model. *Icarus,* 161**,** 66-89.

HALTINER, G. J. A. M., FRANK L. 1957. *Dynamical and Physical Meteorology,* New York, McGraw-Hill Book Company.

HARTOGH, P., MEDVEDEV, A. S., KURODA, T., SAITO, R., VILLANUEVA, G., FEOFILOV, A. G., KUTEPOV, A. A. & BERGER, U. 2005. Description and climatology of a new general circulation model of the Martian atmosphere. *Journal of Geophysical Research: Planets,* 110.

HEAVENS, N., KLEINBÖHL, A., CHAFFIN, M., HALEKAS, J., KASS, D., HAYNE, P., MCCLEESE, D., PIQUEUX, S., SHIRLEY, J. & SCHOFIELD, J. 2018. Hydrogen escape from Mars enhanced by deep convection in dust storms. *Nat Astron,* 2**,** 126-132.

HEIKES, R. P., RANDALL, D. A. & KONOR, C. S. 2013. Optimized icosahedral grids: Performance of finite-difference operators and multigrid solver. *Monthly Weather Review,* 141**,** 4450-4469.

HENG, K., FRIERSON, D. M. & PHILLIPPS, P. J. 2011. Atmospheric circulation of tidally locked exoplanets: II. Dual-band radiative transfer and convective adjustment. *Monthly Notices of the Royal Astronomical Society,* 418**,** 2669-2696.

HOFFMAN, N. Modern geothermal gradients on Mars and implications for subsurface liquids. Conference on the Geophysical Detection of Subsurface Water on Mars, 2001.

HOLLINGSWORTH, J. 2010. *Climate Cycles* [Online]. NASA Ames Mars Climate Modeling Center. Available: Climate Cycles [Accessed 24 March 2018].

HOLLINGSWORTH, J. L. & KAHRE, M. A. 2010. Extratropical cyclones, frontal waves, and Mars dust: Modeling and considerations. *Geophysical Research Letters,* 37**,** L22202.

HOWARD, A. W., MARCY, G. W., BRYSON, S. T., JENKINS, J. M., ROWE, J. F., BATALHA, N. M., BORUCKI, W. J., KOCH, D. G., DUNHAM, E. W. & GAUTIER III, T. N. 2012. Planet occurrence within 0.25 AU of solar-type stars from Kepler. *The Astrophysical Journal Supplement Series,* 201**,** 15.

IRACI, L. T., PHEBUS, B. D., STONE, B. M. & COLAPRETE, A. 2010. Water ice cloud formation on Mars is more difficult than presumed: Laboratory studies of ice nucleation on surrogate materials. *Icarus,* 210**,** 985-991.

JABLONOWSKI, C. & WILLIAMSON, D. L. 2011. The pros and cons of diffusion, filters and fixers in atmospheric general circulation models. *Numerical Techniques for Global Atmospheric Models.* Springer.

JONES, E., CAPRARELLI, G., MILLS, F. P., DORAN, B. & CLARKE, J. 2014. An alternative approach to mapping thermophysical units from Martian thermal inertia and albedo data using a combination of unsupervised classification techniques. *Remote Sensing,* 6**,** 5184-5237.

JUSTUS, C., JAMES, B., BOUGHER, S., BRIDGER, A., HABERLE, R., MURPHY, J. & ENGEL, S. 2002. Mars-GRAM 2000 - A Mars atmospheric model for engineering applications. *Advances in Space Research,* 29**,** 193-202.

KAHRE, M. A. & HABERLE, R. M. 2010. Mars CO2 cycle: Effects of airborne dust and polar cap ice emissivity. *Icarus,* 207**,** 648-653.

KAHRE, M. A., HABERLE, R. M., HOLLINGSWORTH, J. L., MONTMESSIN, F., BRECHT, A. S., URATA, R., KLASSEN, D. R. & WOLFF, M. J. 2017. Updates on Modeling the Water Cycle with the NASA Ames Mars Global Climate Model. *6th International Workshop on the Mars Atmosphere: Modeling and Observations.* Granada, Spain.

KAHRE, M. A., VINES, S. K., HABERLE, R. M. & HOLLINGSWORTH, J. L. 2013. The early Martian atmosphere: Investigating the role of the dust cycle in the possible maintenance of two stable climate states. *Journal of Geophysical Research: Planets,* 118**,** 1388-1396.

KANE, S. R., ARNEY, G., CRISP, D., DOMAGAL-GOLDMAN, S., GLAZE, L. S., GOLDBLATT, C., GRINSPOON, D., HEAD, J. W., LENARDIC, A. & UNTERBORN, C. 2019. Venus as a laboratory for exoplanetary science. *Journal of Geophysical Research: Planets,* 124**,** 2015-2028.

KATARIA, T., SHOWMAN, A. P., FORTNEY, J. J., STEVENSON, K. B., LINE, M. R., KREIDBERG, L., BEAN, J. L. & DÉSERT, J.-M. 2015. The atmospheric circulation of the hot jupiter wasp-43b: comparing three-dimensional models to spectrophotometric data. *The Astrophysical Journal,* 801**,** 86.

KLEMP, J., DUDHIA, J. & HASSIOTIS, A. 2008. An upper gravity-wave absorbing layer for NWP applications. *Monthly Weather Review,* 136**,** 3987-4004.

KNUTSON, H. A., CHARBONNEAU, D., ALLEN, L. E., FORTNEY, J. J., AGOL, E., COWAN, N. B., SHOWMAN, A. P., COOPER, C. S. & MEGEATH, S. T. 2007. A map of the day-night contrast of the extrasolar planet HD 189733b. *Nature,* 447**,** 183.

LAPRISE, R. 1992. The Euler equations of motion with hydrostatic pressure as an independent variable. *Monthly weather review,* 120**,** 197-207.

LASKAR, J. & ROBUTEL, P. 1993. The chaotic obliquity of the planets. *Nature*.

LEVINE, J., KRAEMER, D. & KUHN, W. 1977. Solar radiation incident on Mars and the outer planets - Latitudinal, seasonal, and atmospheric effects. *Icarus,* 31**,** 136-145.

LEWIS, S. R., COLLINS, M., READ, P. L., FORGET, F., HOURDIN, F., FOURNIER, R., HOURDIN, C., TALAGRAND, O. & HUOT, J. P. 1999. A climate database for Mars. *Journal of Geophysical Research: Planets,* 104**,** 24177-24194.

MADELEINE, J. B., FORGET, F., MILLOUR, E., MONTABONE, L. & WOLFF, M. J. 2011. Revisiting the radiative impact of dust on Mars using the LMD Global Climate Model. *Journal of Geophysical Research: Planets,* 116**,** n/a-n/a.

MADHUSUDHAN, N., AGÚNDEZ, M., MOSES, J. I. & HU, Y. 2016. Exoplanetary Atmospheres—Chemistry, Formation Conditions, and Habitability. *Space Science Reviews,* 205**,** 285-348.

MANGAN, T. P., SALZMANN, C. G., PLANE, J. M. C. & MURRAY, B. J. 2017. CO2 ice structure and density under Martian atmospheric conditions. *Icarus,* 294**,** 201-208.

MCCLEESE, D. J., HEAVENS, N. G., SCHOFIELD, J. T., ABDOU, W. A., BANDFIELD, J. L., CALCUTT, S. B., IRWIN, P. G. J., KASS, D. M., KLEINBΓ¶HL, A., LEWIS, S. R., PAIGE, D. A., READ, P. L., RICHARDSON, M. I., SHIRLEY, J. H., TAYLOR, F. W., TEANBY, N. & ZUREK, R. W. 2010. Structure and dynamics of the Martian lower and middle atmosphere as observed by the Mars Climate Sounder: Seasonal variations in zonal mean temperature, dust, and water ice aerosols. *Journal of Geophysical Research: Planets,* 115**,** n/a-n/a.

MENDONÇA, J. M., GRIMM, S. L., GROSHEINTZ, L. & HENG, K. 2016. THOR: a new and flexible global circulation model to explore planetary atmospheres. *The Astrophysical Journal,* 829**,** 115(1-18).

MENDONÇA, J. M., MALIK, M., DEMORY, B.-O. & HENG, K. 2018a. Revisiting the Phase Curves of WASP-43b: Confronting Reanalyzed Spitzer Data with Cloudy Atmospheres. *The Astronomical Journal,* 155**,** 150-159.

MENDONÇA, J. M., TSAI, S.-M., MALIK, M., GRIMM, S. L. & HENG, K. 2018b. Three-dimensional Circulation Driving Chemical Disequilibrium in WASP-43b. *The Astrophysical Journal,* 869**,** 107.

MICHAELS, T., COLAPRETE, A. & RAFKIN, S. 2006. Significant vertical water transport by mountain-induced circulations on Mars. *Geophysical Research Letters,* 33.

MILLOUR, E., FORGET, F., MONTABONE, L., SPIGA, A., COLAITIS, A., NAVARRO, T., MADELEINE, J.-B., LEFÈVRE, F., CHAUFRAY, J.-Y., MONTMESSIN, F., GONZÁLEZ-GALINDO, F., LÓPEZ-VALVERDE, M. A., LEWIS, S., DESJEAN, M.-C. & HUOT, J.-P. 2013. *The LMD Mars Global Circulation Model and Mars Climate Database* [Online]. Available: http://wtk.gfd-dennou.org/2013-02-04/millour/pub/millour_0204.pdf [Accessed].

MISCHNA, M. A., BAKER, V., MILLIKEN, R., RICHARDSON, M. & LEE, C. 2013. Effects of obliquity and water vapor/trace gas greenhouses in the early martian climate. *Journal of Geophysical Research: Planets,* 118**,** 560-576.

MONTABONE, L., FORGET, F., MILLOUR, E., WILSON, R. J., LEWIS, S. R., CANTOR, B., KASS, D., KLEINBÖHL, A., LEMMON, M. T., SMITH, M. D. & WOLFF, M. J. 2015. Eight-year climatology of dust optical depth on Mars. *Icarus,* 251**,** 65-95.

MOUDDEN, Y. & MCCONNELL, J. 2005. A new model for multiscale modeling of the Martian atmosphere, GM3. *Journal of Geophysical Research: Planets,* 110.

NASA. 2018. *About the James Webb Space Telescope* [Online]. Goddard Space Flight Center, National Aeronautics and Space Administration (NASA). Available: https://jwst.nasa.gov/about.html [Accessed 19 April 2018].

PETIGURA, E. A., HOWARD, A. W. & MARCY, G. W. 2013. Prevalence of Earth-size planets orbiting Sun-like stars. *Proceedings of the National Academy of Sciences,* 110**,** 19273-19278.

PHL. 2012. *HEC: Science Plots* [Online]. Planetary Habitability Laboratory @ University of Puerto Rico at Arecibo. Available: http://phl.upr.edu/projects/habitable-exoplanets-catalog/results/science-plots [Accessed 14 May 2017].

PHL. 2018. *HEC: Periodic Table of Exoplanets* [Online]. Planetary Habitability Laboratory @ University of Puerto Rico at Arecibo. Available: http://phl.upr.edu/projects/habitable-exoplanets-catalog/media/pte [Accessed 30 March 2020].

READ, P. L., LEWIS, S. R. & MULHOLLAND, D. P. 2015. The physics of Martian weather and climate: a review. *Reports on progress in physics. Physical Society (Great Britain),* 78**,** 125901.

SANGSTER, W. E. 1960. A method of representing the horizontal pressure force without reduction of station pressures to sea level. *Journal of Meteorology,* 17**,** 166-176.

SCHMIDT, G. A. 2019. *Mars24 Sunclock — Time on Mars* [Online]. NASA Goddard Institute for Space Studies. Available: https://www.giss.nasa.gov/tools/mars24/help/algorithm.html [Accessed 16 September 2019].

SELSIS, F., WORDSWORTH, R. D. & FORGET, F. 2011. Thermal phase curves of nontransiting terrestrial exoplanets-I. Characterizing atmospheres. *Astronomy & Astrophysics,* 532**,** A1.
SKAMAROCK, W. C. & KLEMP, J. B. 2008. A time-split nonhydrostatic atmospheric model for weather research and forecasting applications. *Journal of Computational Physics,* 227**,** 3465-3485.
SMITH, M. D., WOLFF, M. J., LEMMON, M. T., SPANOVICH, N., BANFIELD, D., BUDNEY, C. J., CLANCY, R. T., GHOSH, A., LANDIS, G. A. & SMITH, P. 2004. First atmospheric science results from the Mars Exploration Rovers Mini-TES. *Science,* 306**,** 1750-1753.
STEELE, L. J., LEWIS, S. R. & PATEL, M. R. 2014b. The radiative impact of water ice clouds from a reanalysis of Mars Climate Sounder data. *Geophysical Research Letters,* 41**,** 4471-4478.
STEELE, L. J., LEWIS, S. R., PATEL, M. R., MONTMESSIN, F., FORGET, F. & SMITH, M. D. 2014a. The seasonal cycle of water vapour on Mars from assimilation of Thermal Emission Spectrometer data. *Icarus,* 237**,** 97-115.
STEVENSON, K. B., DESERT, J. M., LINE, M. R., BEAN, J. L., FORTNEY, J. J., SHOWMAN, A. P., KATARIA, T., KREIDBERG, L., MCCULLOUGH, P. R., HENRY, G. W., CHARBONNEAU, D., BURROWS, A., SEAGER, S., MADHUSUDHAN, N., WILLIAMSON, M. H. & HOMEIER, D. 2014. Thermal structure of an exoplanet atmosphere from phase-resolved emission spectroscopy. *Science,* 346.
TILLMAN, J. E., JOHNSON, N. C., GUTTORP, P. & PERCIVAL, D. B. 1993. The Martian annual atmospheric pressure cycle: Years without great dust storms. *Journal of Geophysical Research: Planets,* 98**,** 10963-10971.
TOMITA, H. & SATOH, M. 2004. A new dynamical framework of nonhydrostatic global model using the icosahedral grid. *Fluid Dynamics Research,* 34**,** 357.
TOMITA, H., SATOH, M. & GOTO, K. 2002. An optimization of the icosahedral grid modified by spring dynamics. *Journal of Computational Physics,* 183**,** 307-331.
TOMITA, H., TSUGAWA, M., SATOH, M. & GOTO, K. 2001. Shallow water model on a modified icosahedral geodesic grid by using spring dynamics. *Journal of Computational Physics,* 174**,** 579-613.
TURBET, M., LECONTE, J., SELSIS, F., BOLMONT, E., FORGET, F., RIBAS, I., RAYMOND, S. N. & ANGLADA-ESCUDÉ, G. 2016. The habitability of Proxima Centauri b. *A&A,* 596**,** A112.
ULLRICH, P. A., REYNOLDS, D. R., GUERRA, J. E. & TAYLOR, M. A. 2018. Impact and importance of hyperdiffusion on the spectral element method: A linear dispersion analysis. *Journal of Computational Physics,* 375**,** 427-446.
URATA, R. A. & TOON, O. B. 2013. A new general circulation model for Mars based on the NCAR Community Atmosphere Model. *Icarus,* 226**,** 336-354.
WATTERS, T., MCGOVERN, P. & IRWIN, R. 2007. Hemispheres Apart: The Crustal Dichotomy on Mars. *Annual Review of Earth and Planetary Sciences,* 35**,** 621-652.
WHITE, A. A., HOSKINS, B. J., ROULSTONE, I. & STANIFORTH, A. 2005. Consistent approximate models of the global atmosphere: shallow, deep, hydrostatic, quasi-hydrostatic and non-hydrostatic. *Quarterly Journal of the Royal Meteorological Society: A journal of the atmospheric sciences, applied meteorology and physical oceanography,* 131**,** 2081-2107.
WILLIAMS, D. R. 2018a. *Sun Fact Sheet* [Online]. National Space Science Data Coordinated Archive, NASA Goddard Space Flight Center. Available: https://nssdc.gsfc.nasa.gov/planetary/factsheet/sunfact.html [Accessed 5 June 2019].
WILLIAMS, D. R. 2018b. *Mars Fact Sheet* [Online]. National Space Science Data Coordinated Archive, NASA Goddard Space Flight Center. Available: https://nssdc.gsfc.nasa.gov/planetary/factsheet/marsfact.html [Accessed 5 June 2019].
WILLIAMS, D. R. 2020. *Earth Fact Sheet* [Online]. National Space Science Data Coordinated Archive, NASA Goddard Space Flight Center. Available: https://nssdc.gsfc.nasa.gov/planetary/factsheet/earthfact.html [Accessed 31 March 2020].
ZALUCHA, A. M., MICHAELS, T. I. & MADHUSUDHAN, N. 2013. An investigation of a super-Earth exoplanet with a greenhouse-gas atmosphere using a general circulation model. *Icarus,* 226**,** 1743-1761.
ZHANG, H. & SHI, G.-Y. 2001. An improved approach to diffuse radiation. *Journal of Quantitative Spectroscopy and Radiative Transfer,* 70**,** 367-372.

Appendix 1

Mars Orbiter Laser Altimeter topographic map of Mars, created by Emily Lakdawalla for NASA/JPL/GSFC, and modified for the Planetary Society's Bruce Murray Space Image Library. A digital high-resolution version is available for viewing at https://planetary.s3.amazonaws.com/assets/images/4-mars/2013/20131025_mars-major-features.jpg

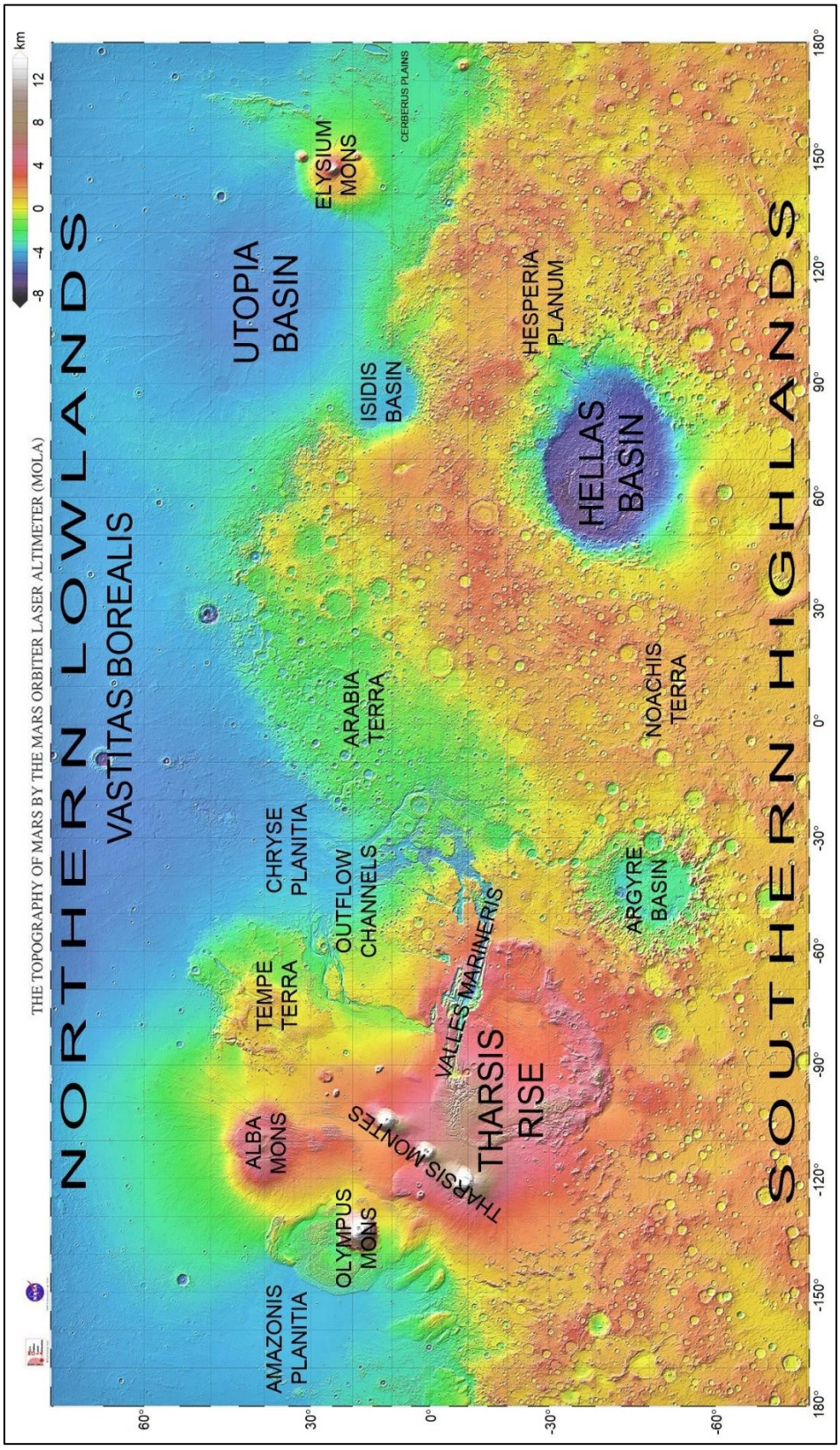

Appendix 2

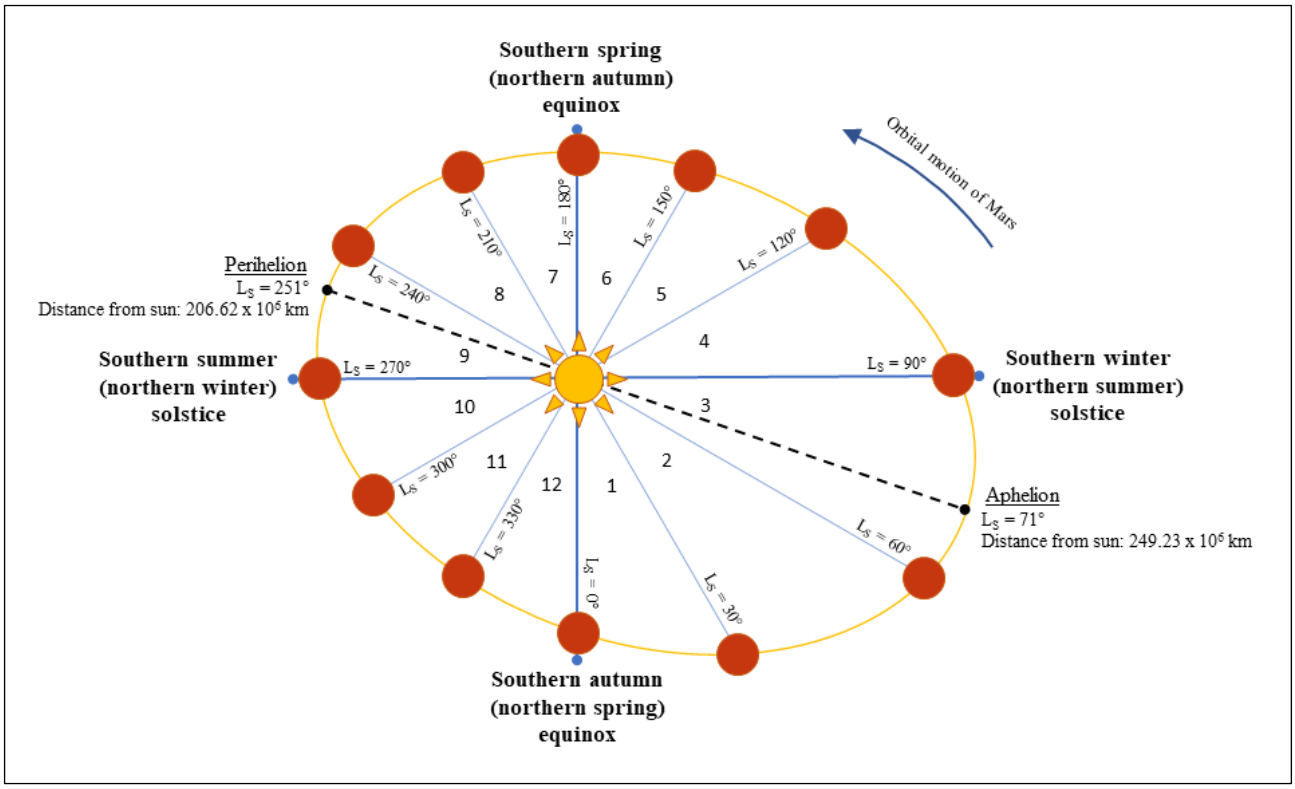

Figure 1: Diagram of Mars's orbit (not to scale). Numbers 1-12 denote the Martian seasons listed in Chapter 3, Table 2.

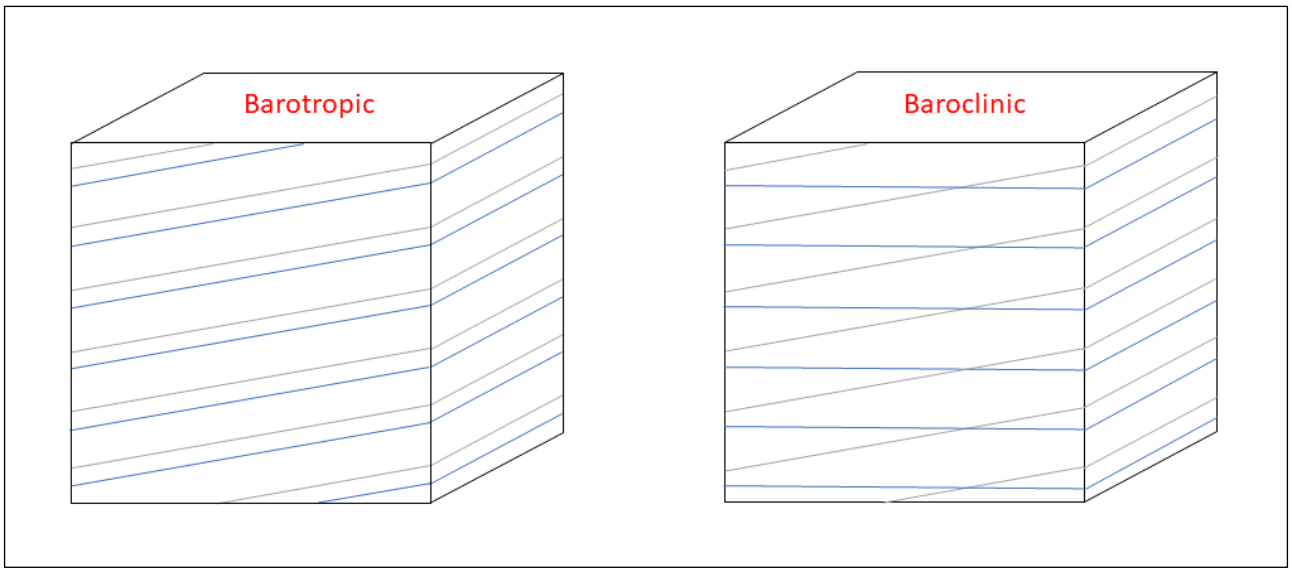

Figure 2: Concept comparison of a barotropic atmosphere (left) and a baroclinic (right) atmosphere. Blue lines represent surfaces of constant density, grey lines represent surfaces of constant pressure.

Appendix 3

Table of available parameters in THOR and their corresponding values. Parameters with a value of "*Variable*" are those which have been varied according to the scenarios laid out in Chapter 2, Section 2.3.4. Parameters which are greyed out are ones which were never enabled in THOR for this work.

Parameter	Symbol	Code	Value
TIMESTEPPING/OUTPUT OPTIONS			
Number of steps		num_steps	432000
Length of timesteps (s)		timestep	300
Output every n steps		N_out	1500
Conserve angular momentum, etc		conservation	true
PLANETARY PARAMETERS			
Radius (m)	R	radius	3396200
Rotation rate (rad/s)	ω	rotation_rate	7.078e-5
Gravitational acceleration (m/s^2)	g	gravitation	3.71
Gas constant (J/kg·K)	R_d	Rd	191.84
Specific heat capacity (J/kg·K)	C_p	Cp	750
Mean atmospheric temperature (K)	T	Tmean	210
Reference surface pressure (Pa)	P_{ref}	P_ref	636
GRID OPTIONS			
Altitude at top of model domain	z	Top_altitude	100000
Horizontal resolution level		glevel	4
Vertical resolution level		vlevel	40
Enable spring dynamics		spring_dynamics	true
Parameter beta for spring dynamics	β	spring_beta	1.15
DIFFUSION			
Enable hyper-diffusion		HyDiff	true
Enable divergence-damping		DivDampP	true
Strength of diffusion	K_d	Diffc	0.015
Strength of divergence damping	K	DivDampc	0.015
MODEL OPTIONS			
Enable non-hydrostatic parameter		NonHydro	true
Enable deep atmosphere		DeepModel	true
Use initial conditions file (ifile)		rest	true
Select core benchmark test		core_benchmark	NoBenchmark
Switch off dynamical core		gcm_off	false
Enable convective adjustment scheme		conv_adj	1 (0 = false, 1 = true)
SPONGE LAYER			
Use sponge layer at top of atmosphere		SpongeLayer	true
Number of latitude rings		nlat	20
Bottom of sponge layer (fractional height)	η_s	ns_sponge	0.75
Strength of sponge layer (1/damping time)	k_s	Rv_sponge	1e-4
Shrink sponge by half after some time		shrink_sponge	true
When to shrink sponge (days)		t_shrink	1

RADIATIVE TRANSFER OPTIONS			
Enable radiative transfer		radiative_transfer	true
Stellar temperature (K)	$T_\odot$	Tstar	5772
Orbital distance or semi-major axis (AU)	d	planet_star_dist	1.52366231
Radius of host star ($R_\odot$)	$R_\odot$	radius_star	1
Bond albedo of planet	A	albedo	0.25
Grey opt. depth of thermal wavelengths (at ref. pressure)	τ_{lw}	taulw	*Variable*
Grey opt. depth of incoming stellar flux (at ref. pressure)	τ_{sw}	tausw	0.45
Opt. depth at poles	$\tau_{lw,pole}$	taulw_pole	*Variable*
1/diffusivity factor (1/r) *(where r = 1.81, as per Chapter 2, Section 2.3.3.2)*		diff_ang	0.5
Add $\sin(\text{lat})^2$ dependence to tau lw		latf_lw	true
Temperature of internal heat flux (K)	T_{low}	Tlow	25
Heat capacity of surface ($J/K \cdot m^2$)	C_{surf}	Csurf	*Variable*
POWER LAW INDEX OF UNMIXED ABSORBERS			
Longwave index	n_L	n_lw	4
Shortwave index	n_S	n_sw	2
Strength of unmixed absorbers in longwave	f_L	f_lw	0.5
INSOLATION PARAMETERS			
Enable synchronous rotation		sync_rot	false
Mean motion of orbit (rad/s)	Ω	mean_motion	1.05e-7
Initial substellar longitude (deg)	α_i	alpha_i	0
Initial orbital position (deg)	$L_{s,i}$	true_long_i	0
Eccentricity or orbit	e	ecc	0.09341233
Obliquity (deg)	ε	obliquity	*Variable*
Longitude of periastron	$\overline{\omega}$	longp	336.04084
BOUNDARY LAYER OPTIONS			
Enable lower boundary layer		boundary_layer	false
Type of boundary layer drag		bl_type	RayleighHS
Strength of drag	k_v	surf_drag	1.157407e-5
Boundary layer sigma	σ_b	bl_sigma	0.7
DEVICE OPTIONS			
GPU ID number		GPU_ID_N	0

Appendix 4

Comparison plots for areal heat capacities of $C_1 = 1.8 \times 10^5$ J·K^{-1}·m^{-2} and $C_2 = 2.6 \times 10^6$ J·K^{-1}·m^{-2}

Appendix 4A

$\tau = 0.3$, $\varepsilon = 25.19°$, **$L_S = 270°$**

	Zonal mean temperature	Zonal wind speed	Vertical wind speed
C_1	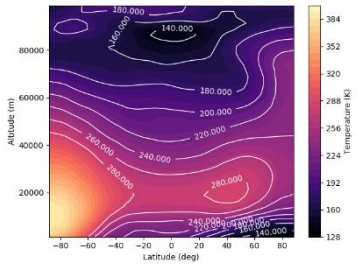	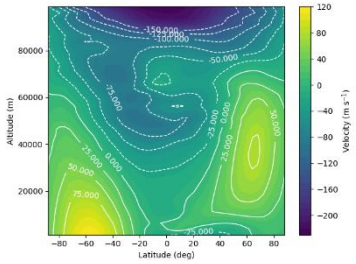	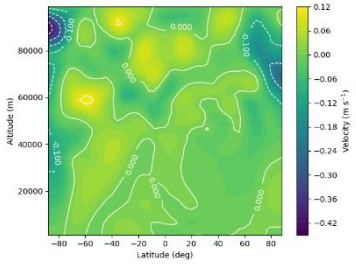
C_2	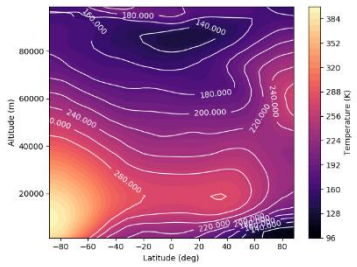	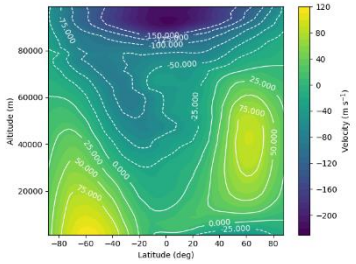	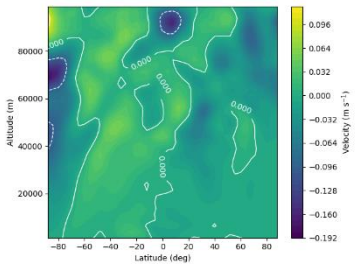
Past works	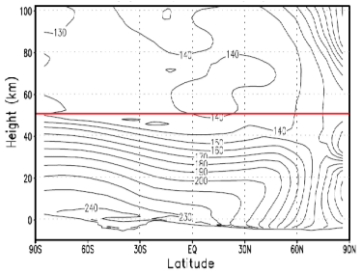 Moudden and McConnell (2005), Figure 5a	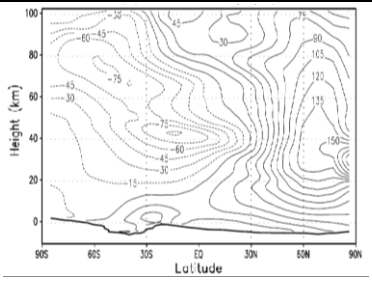 Moudden and McConnell (2005), Figure 5d	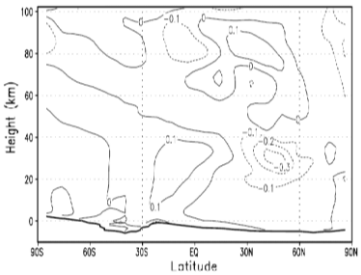 Moudden and McConnell (2005), Figure 5f

Appendix 4B

$\tau = 0.3$, $\varepsilon = 25.19°$, $\underline{L_s = 90°}$

	Zonal mean temperature	Zonal wind speed	Vertical wind speed
C_1	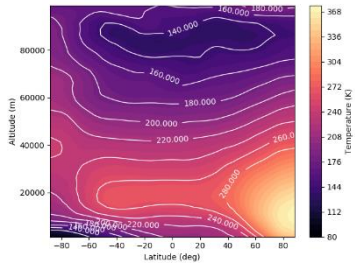	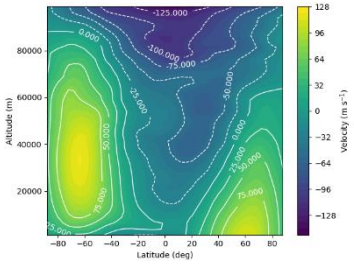	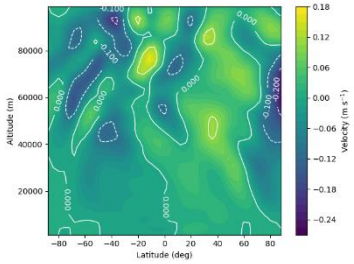
C_2	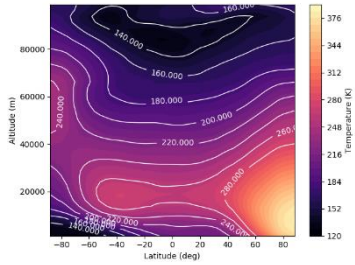	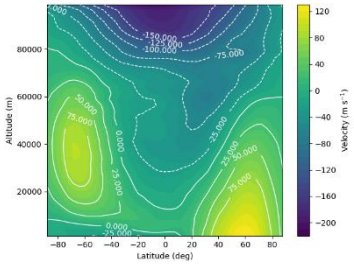	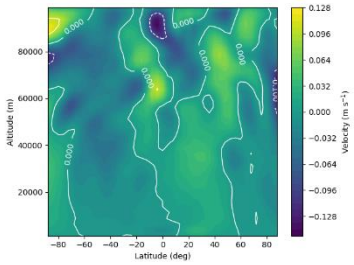
Past works	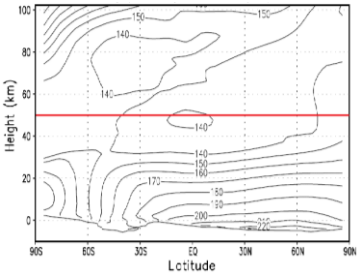 Moudden and McConnell (2005), Figure 7a	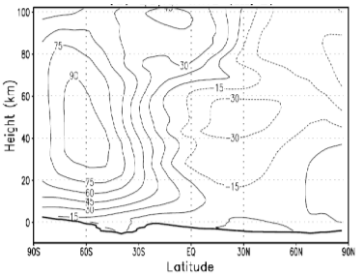 Moudden and McConnell (2005), Figure 7d	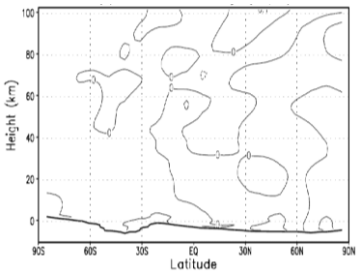 Moudden and McConnell (2005), Figure 7f

Appendix 4C

$\tau = 0.3$, $\varepsilon = 0°$, $\underline{L_s = 0°}$

	Zonal mean temperature	Zonal wind speed	Mass stream function
C_1	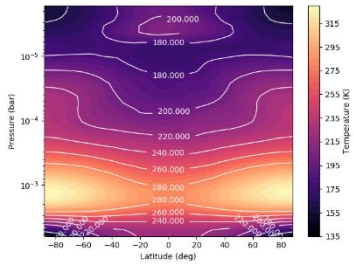	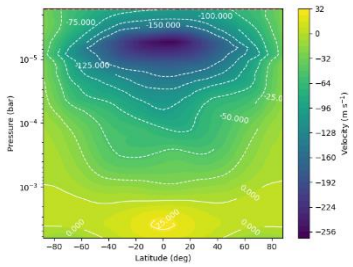	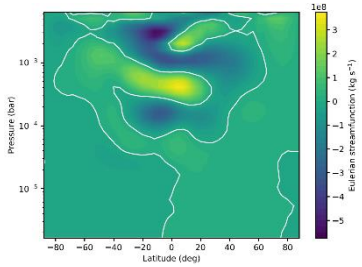
C_2	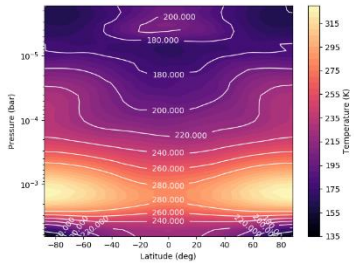	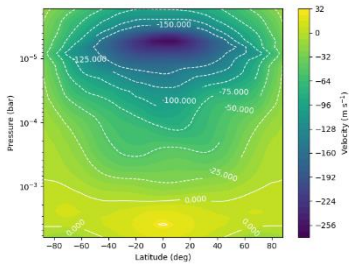	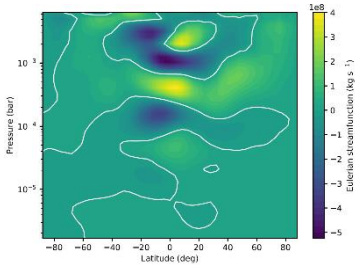
Past works	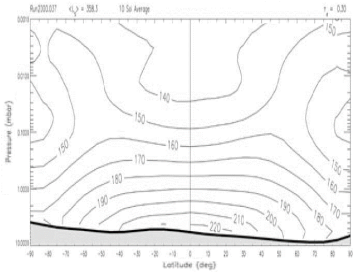 Haberle et al. (2003b), Figure 12a (top)	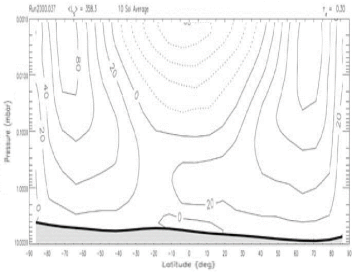 Haberle et al. (2003b), Figure 12a (middle)	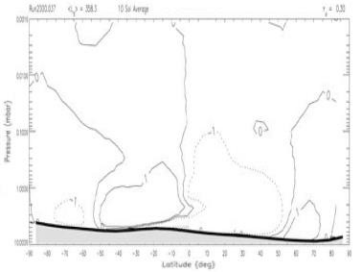 Haberle et al. (2003b), Figure 12a (bottom)

Appendix 4D

$\tau = 0.3$, $\varepsilon = 0°$, $\underline{L_s = 270°}$

	Zonal mean temperature	Zonal wind speed	Mass stream function
C_1	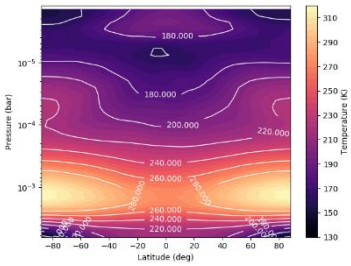	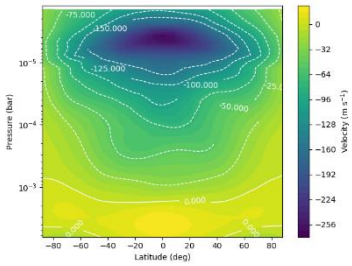	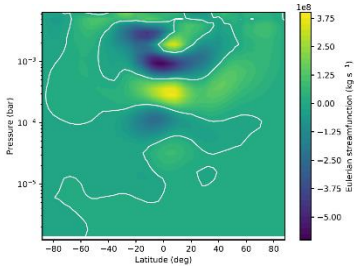
C_2	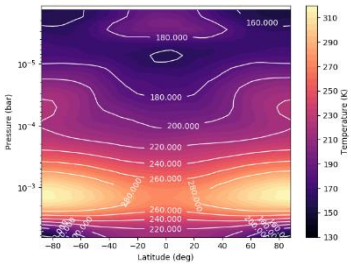	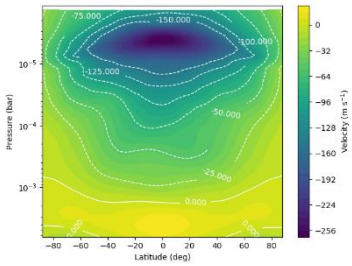	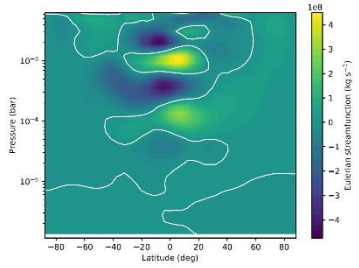
Past works	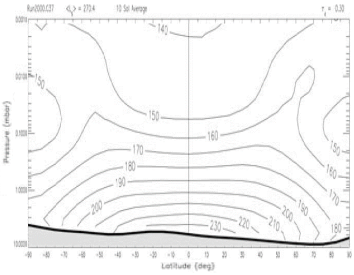 Haberle et al. (2003b), Figure 13a (top)	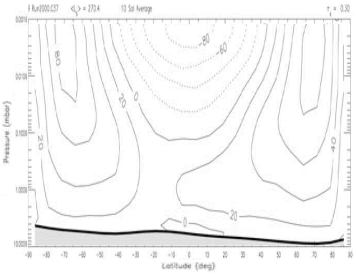 Haberle et al. (2003b), Figure 13a (middle)	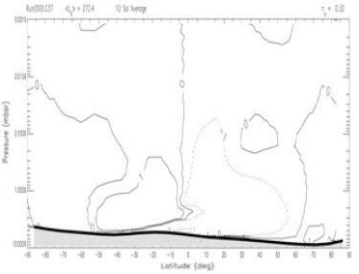 Haberle et al. (2003b), Figure 13a (bottom)

Appendix 4E

$\tau = 0.3$, $\varepsilon = 60°$, $\underline{L_s = 0°}$

	Zonal mean temperature	Zonal wind speed	Mass stream function
C_1	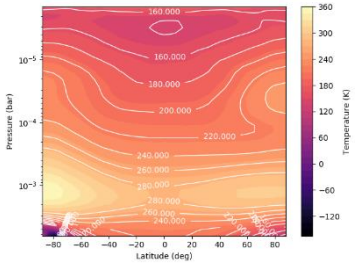	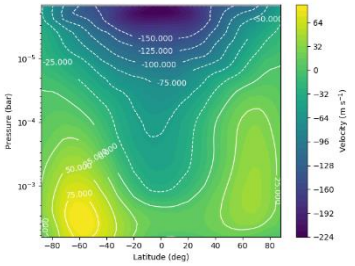	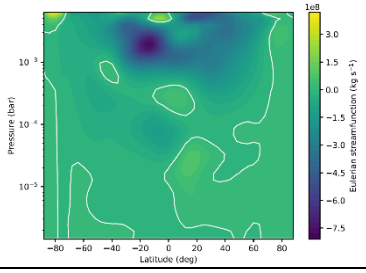
C_2	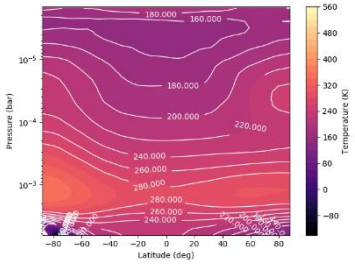	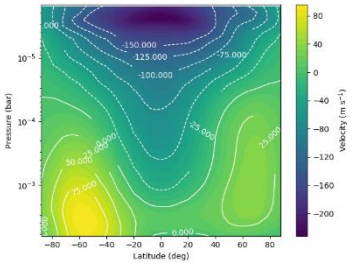	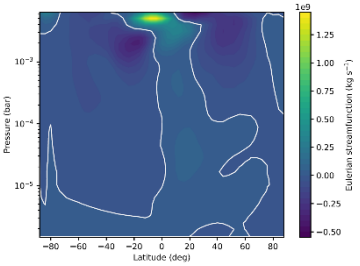
Past works	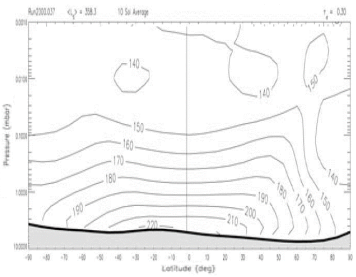 Haberle et al. (2003b), Figure 12b (top)	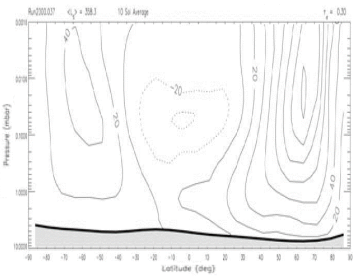 Haberle et al. (2003b), Figure 12b (middle)	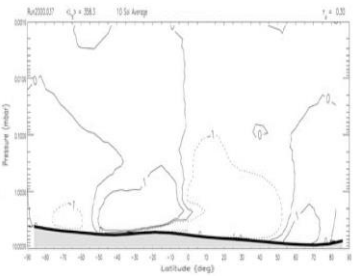 Haberle et al. (2003b), Figure 12b (bottom)

Appendix 4F

$\tau = 0.3$, $\varepsilon = 60°$, $\underline{L_s = 270°}$

	Zonal mean temperature	Zonal wind speed	Mass stream function
C_1	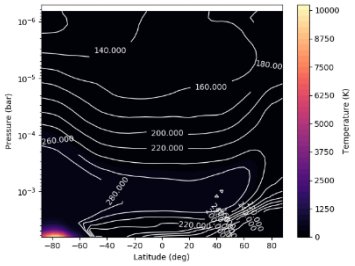	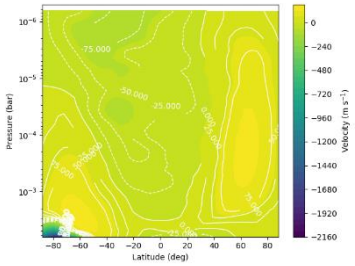	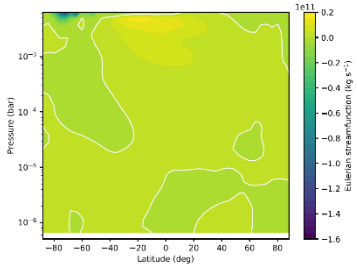
C_2	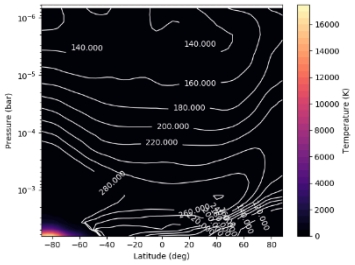	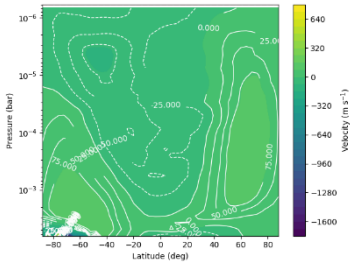	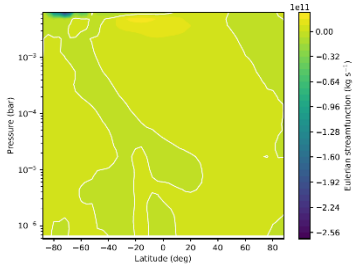
Past works	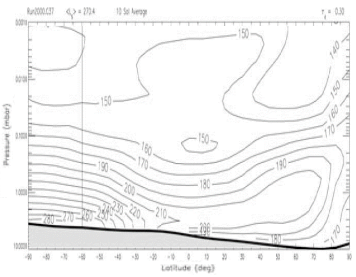 Haberle et al. (2003b), Figure 13b (top)	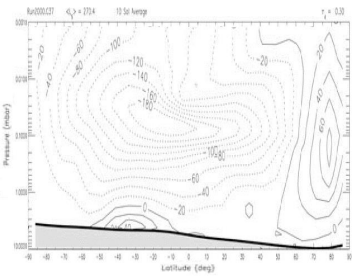 Haberle et al. (2003b), Figure 13b (middle)	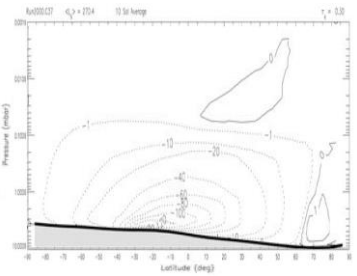 Haberle et al. (2003b), Figure 13b (bottom)

Appendix 5

Zonal mean temperature and zonal wind results for ε = 0° at L_s = 270°

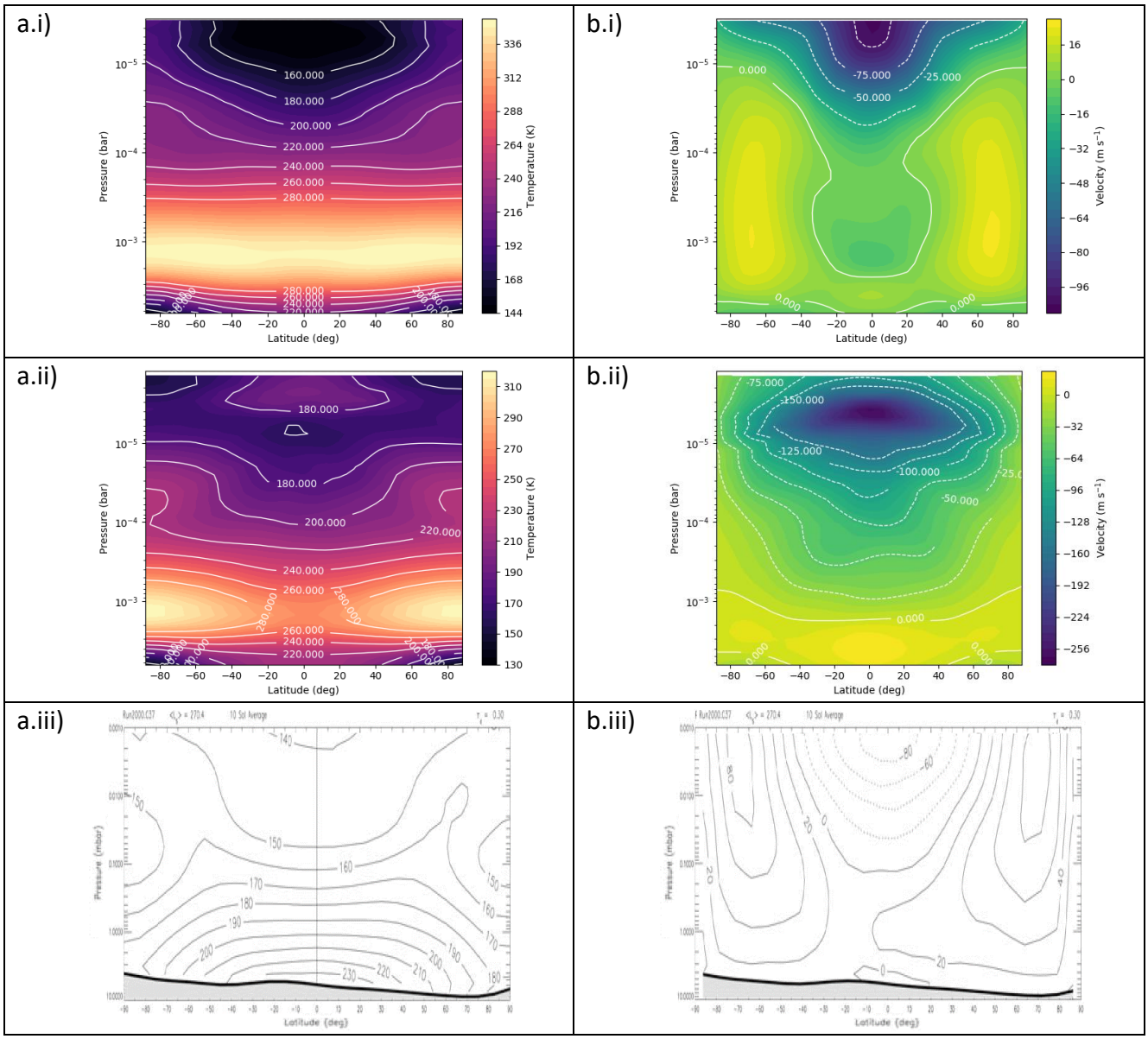

Figure 1: Low obliquity (ε = 0°) outputs at L_s = 270° a) zonal mean temperature simulated by (i) THOR for τ_{lw} = 0.1, averaged over 5 days, (ii) THOR for τ_{lw} = 0.3, averaged over 5 days (iii) NASA/AMES for τ_{lw} = 0.3, averaged over 10 sols; b) zonal wind simulated by (i) THOR for τ_{lw} = 0.1, averaged over 5 days, (ii) THOR for τ_{lw} = 0.3, averaged over 5 days, (iii) NASA/AMES for τ_{lw} = 0.3, averaged over 10 sols. Figures a.iv) and b.iv) are taken from Haberle et al. (2003).

Appendix 6

A comparison of southern autumnal equinox results generated by THOR under the low dust loading regime at low obliquity and high obliquity vs. present-day (current) obliquity. The top row of figures compares zonal mean temperature results, while the bottom row compares zonal wind speeds.

Low obliquity regime (ε = 0°)	**Current obliquity regime (ε = 25.19°)**	**High obliquity regime (ε = 60°)**